University of Bath

UNIVERSITY OF BATH

PHD

Broadband studies of acoustic scattering from a model rough surface.

Thorne, P. D.

Award date:
1982

Awarding institution:
University of Bath

Alternative formats

If you require this document in an alternative format, please contact:
openaccess@bath.ac.uk

BROADBAND STUDIES OF ACOUSTIC SCATTERING

FROM A MODEL ROUGH SURFACE

Submitted by P D Thorne

for the degree of Ph.D

of the University of Bath

1982

COPYRIGHT

P.O. Thorne

ProQuest Number: U333225
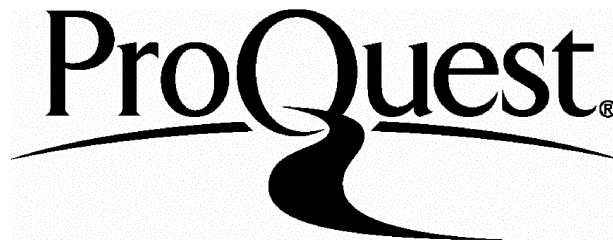
ProQuest U333225

Abstract

Experimental measurements at near normal incidence of the

underwater acoustic backscattering from a pressure release model

rough surface with Gaussian statistics were conducted in a laboratory

tank. Scattering measurements were obtained over the frequency range

20-1200 kHz, for a variety of transmitter and receiver positions. To

obtain a source that has sufficient directivity and a wide enough

bandwidth performance, to carry out the investigation, advantage was

taken of the parametric array's unique properties.

Theoretical expressions for the mean intensity were developed,

using the Helmholtz-Kirchhoff Integral. The Fresnel and

Fraunhofer phase approximations were used to evaluate the scattering

integral, and predictions for the mean intensities were compared with

the measured values. The Fresnel approach gave scattering coefficients

which were in closer agreement with the experimental values.

Acknowledgements

I wish to express my thanks to my supervisor, Dr N. Pace, for his guidance and valuable criticisms throughout this study, to Professor H.O. Berktay for his encouragement and enlightening discussions, and to all who worked in the underwater acoustic section for their general interest.

I would like to thank the technical staff particularly Mr B Ring and Mr B Gay for their assistance and advice.

My thanks also to Jane Sloper for patiently typing the dissertation.

Finally special thanks go to Katharine Rhodes for her invaluable help in the preparation of this manuscript.

The work was supported by a Research Studentship from the Natural Environment Research Council.

Contents

Page

List Of Figures

Page

Figure

Chapter 2

Chapter 3

Chapter 4

Page

Chapter 6

Appendix 2

Page

Appendix 5

Chapter 1   Introduction

1.1   Background

Interest in the scattering of waves embraces many fields of

activity.   Scattering of electromagnetic waves from marine and

ground surfaces as considered by Ouchi, Uscinski, Robertson and

Thomas (1), and from sub-glacial beds as studied by Berry (2) are

developing areas of investigation.   With regard to acoustics and

in particular underwater acoustics, the effect of rough boundaries

upon communication, detection and also the inverse problem of iden-

tification of surface features from scattered waves have all

commanded much interest.   In this investigation the emphasis is placed

on a well defined underwater acoustic wave encountering a rough sur-

face and being scattered back into the half space containing the

acoustic source.   A tremendous amount of material has been published on

this aspect of scattering, much of which was found most useful in this

study.   Reviews by Horton (3) and Fortuin (4) provide useful intro-

ductions into the subject.

1.2   The Rayleigh Method

The earliest attempt to obtain a solution for a plane wave being

scattered from a rough boundary is attributed to Rayleigh (5) who

considered the case of normal incidence sound being scattered by a

corrugated surface.   The solution consisted of the incident plane

wave being scattered in discrete directions,which had amplitudes

that could be obtained by successive approximations from an infinite

set of linear equations.   This approach was extended by La Casce and

Tamarkin (6) for a general angle of incidence, and they presented this with one of the earliest underwater experiments on a rough surface. Using three constructed pressure release surfaces with sinusoidal corrugations comparisons were made between the experimental and theoretical values obtained by various approaches including Rayleigh's. Reasonable agreement was obtained when the surface slopes were small. Marsh (7) developed the Rayleigh method to investigate the scattered field from a one-dimensional irregularly rough surface, however, little experimental work has been compared with this method.

Uretsky (8) approached the problem of scattering from a sinusoidal surface by using the Helmholtz equation written in terms of Green's functions. Uretsky obtained a general solution which showed that the Rayleigh method only gives good estimates for the scattered field when the surface undulations are small. Again, however, the problem was reduced to that of solving an infinite set of linear equations by successive approximation. Using Uretsky's theory the predicted preferred directions and amplitudes of the scattered plane wave reflected from a pressure release sinusoidal surface of particular dimensions were computed and measured by Barnard,Horton, Miller and Spitznogle (9) and good agreement was obtained.

1.3 Helmholtz-Kirchhoff Method

Rather than using either the Rayleigh or a generalised Uretsky method when approaching the problem of a non-deterministic surface,

such as used in this study, a more common course has been to use
the Helmholtz theorem with the Kirchhoff boundary conditions. The
Helmholtz integral expresses the scattered field at a point of
observation as an integral over the elementary Huygen sources
which are induced on the surface by the incident wave. The
source strengths are evaluated using Kirchhoff's equations. This
method initially applied to a rough surface by Eckart (10), offers
a more tractable solution to the problem of scattering from a
randomly rough boundary than either the Rayleigh or Uretsky approach.

The Helmholtz integral is given by Clay and Medwin (11) as

$$\dot{p}(r) = \frac{1}{4\pi} \int_S [p \frac{\partial}{\partial n} (\frac{\exp{(ikr)}}{r}) - (\frac{\exp{(ikr)}}{r}) \frac{\partial p}{\partial n}] \, dS \qquad 1-1$$

where r is the distance from dS, the surface element, to the
observation point, n is the normal to dS drawn towards the half
space containing the source and receiver, and p and $\partial p/\partial n$ are the
values of the pressure and its normal derivative on the surface.
The exact values of these latter two quantities on the surface
are generally unknown and the Kirchhoff method consists of
approximating these values by those that would be present on a
tangental plane at this point. With this approximation the bound-
ary conditions can be stated in terms of the incident field, p(i)
at the surface

$$p = R\, p(i) \qquad\qquad 1-2$$

$$\frac{\partial p}{\partial n} = \frac{-R \partial p(i)}{\partial n} \qquad\qquad 1-3$$

$$R = \frac{Z_2 \cos\theta_1 - Z_1 \cos\theta_2}{Z_2 \cos\theta_1 + Z_1 \cos\theta_2} \qquad\qquad 1-4$$

Where R is the reflection coefficient. Using 1-4 Eckart

developed a statistical theory for a boundary that is randomly

rough in two dimensions. Estimates for the mean intensity of

the scattered radiation from a randomly rough surface were obtained

for two regimes of long and short wavelengths of the incident radi-

ation relative to the surface roughness. A dimensionless para-

meter known as the scattering coefficient S_c is defined, and for

these two cases is given by

$$S_c = (k^2 c^2 / 4\pi)^2\, S(ka,\ kb) \quad \text{long wavelength} \qquad 1-5$$

$$S_c = (1/8\pi\alpha\beta)\exp[-\tfrac{1}{2}[(a/\alpha c)^2 + (b/\beta c)^2]] \quad \text{short wavelength} \qquad 1-6$$

where a, b, c are the sum of the x, y, z directional cosines of

the vectors from the transducer to the area of insonification and

from the area to the receiver, α and β are the root-mean-square slopes

of the surface in the x and y directions, and S(ka, kb) is the
power spectrum of the surface relief. At low frequencies the
scattering coefficient is seen to be dependent on frequency to
the fourth power, while at the high frequencies, for a bivariate
Gaussian height distribution, the only surface features involved
are the surface slopes.

Eckart's approach was applied to surfaces with a Gaussian
height distribution and specific autocorrelation functions by Horton
and Muir (12). The short wavelength predictions, for a number of
incidence angles, were compared with experimental values of the
scattered intensity from a pressure release randomly rough sur-
face, presented in a companion paper by Horton, Mitchell and
Barnard(13). The boundary condition of equation 1-3 which for a
pressure release surface is given by

$$\frac{\partial p}{\partial n} = \frac{\partial p(i)}{\partial n}$$

was changed to

$$\frac{\partial p}{\partial n} = 0$$

to obtain calculated scattered intensities which were in good
agreement with the measured data. The negligible normal pressure
derivative was thought to arise from the strong relief on the model
surface.

Proud, Beyer and Tamarkin (14) extended the Helmholtz-Kirchhoff Integral approach and obtained a solution valid for all frequencies for a one-dimensional randomly rough surface. Two pressure release surfaces were constructed, one modelled to have a Gaussian height distribution, and the other having an analytical auto-correlation function. Using these surfaces it was shown that acoustic scattering measurements could be used in conjunction with the theory to derive the root-mean-square height of the first surface, and correlation function of the second.

One of the earliest and most important treatises on the development of scattering from a rough surface is that of Beckmann and Spizzichino (15). The formulation of the problem on scattering from a two-dimensional randomly rough surface is again statistical, and based on the Helmholtz-Kirchhoff Integral. However, the geometrical representation is simpler than of those previously mentioned; all the solutions are normalised at the outset to a plane surface with unit reflection coefficient, the calculation of the normal derivatives in the scattering integral is not approximated to being in the $\hat{z}$ direction, and the expressions obtained cover the whole of the frequency range for a two-dimensional randomly rough surface. The solutions derived are also separated into two components, the coherent and incoherent. The coherent part of the scattered intensity is obtained from the ensemble average of the pressure with regard to phase. The incoherent part is the residual mean intensity after the coherent component has been removed from the total scattered intensity and is given by

$$\langle I \rangle_{IC} = \langle pp^* \rangle_T - \langle p \rangle_C^2$$

1-7

where p and p* are the scattered pressure and its complex conjugate, $\langle \rangle$ indicates ensemble average, and IC, T and C are the incoherent, total, and coherent intensities respectively.

As the surface becomes smoother the signal variance reduces and the coherent component becomes equal to the total intensity and the incoherent component tends to zero. For large fluctuations in intensity the coherent tends to zero and the total intensity becomes incoherent. Their formulation of the scattering problem in terms of two components normalised by a plane surface give final expressions which are readily interpretable and lend themselves easily to experimental investigation.

To obtain their solution to the scattering problem,Beckmann and Spizzichino chose a surface with Gaussian height statistics and a Gaussian autocorrelation function. The acoustic source was given a rectangular directivity pattern with no sidelobes. The principal result relevant to the scattered intensity from a two-dimensional randomly rough surface is

$$\frac{\langle I \rangle_T}{I_0} = D^2 \exp(-g) + \frac{\pi T^2 F_j^2}{A} \exp(-g) \sum_{n=1}^{\infty} \frac{g^n}{n\,n!} \exp\left(-\frac{k^2 V^2 T^2}{4n}\right)$$

1-8

where

$$F_1 = \frac{1 + \cos\theta_1 \cos\theta_2 - \sin\theta_1 \sin\theta_2 \cos\theta_3}{\cos\theta_1(\cos\theta_1 + \cos\theta_2)}$$

$$g = k^2 h^2 (\cos\theta_1 + \cos\theta_2)^2$$

$$D = \text{Sinc } \alpha X \sin\beta Y$$

$$\alpha = (\sin\theta_1 - \sin\theta_2 \cos\theta_3)$$

$$\beta = -\sin\theta_2 \sin\theta_3$$

$$V^2 = \alpha^2 + \beta^2$$

$<I>_T$ is the total mean scattered intensity, and is normalised by

the specular intensity, I_0, reflected from a plane surface with

a reflection coefficient of unity. X and Y are the half-lengths

of the insonified area A = 4XY. The incident scalar wave number

is k, h is the root-mean-square height of the rough surface and

T is its autocorrelation length. θ_1 is the angle of incidence,

θ_2 is the scattered angle in the same plane as θ_1 and θ_3 is the

angle out of this plane. The geometry is shown in figure 1 of the

following chapter. q is frequently used, and is known as the roughness parameter.

The first term on the right hand side of equation 1-8 is

the coherent component. For a surface with a Gaussian height dis-

tribution, this is seen to reduce exponentially as g increases.

The second term, the incoherent can be simplified for scattering

in the specular direction where V = 0 and F = 1. In this direction

for g<<1 and g>>1 respectively then the incoherent component is

given respectively by

$$[\frac{\pi T^2 g}{A}]_{g<<1} \quad \text{(a)} \qquad [\frac{\pi T^2}{Ag}]_{g>>1} \quad \text{(b)} \qquad 1\text{-}9$$

As $T^2 <<A$ then when g<<1 the coherent term will dominate. The

inequality $T^2 <<A$ needs to be true since if it were not the case

only one or two irregularities would be insonified rather than an

area of surface roughness. At high frequencies the coherent expon-

ential term becomes negligible and the scattered intensity is

given by 1-9b.

Clay and Medwin (16) used the high frequency approximation

multiplied by a diffraction term to analyse backscattered data

of acoustic waves from the sea surface, and found it to be useful

near normal incidence. Hayre and Kaufman (17) extended the theory

to a surface with composite roughness. Medwin (18) following the

development of Beckmann and Spizzichino modified their approach

by introducing a more realistic directivity function for the

transmitter. The solution for normal incidence was used to estimate

the root-mean-square height and slope of an agitated water surface

from acoustically backscattered signals.

A serious criticism arises in the formulation of equation 1-8,

because the factor used to normalise the scattered field by the

specular intensity reflected from a plane surface with unit reflec-
tion coefficient is, ~~not realisable using a~~ real source, and this has introduced some confusion

into the literature when considering the incoherent intensity. The

normalising term used by Beckmann and Spizzichino is

$$p_0 = \frac{ikA \, Cos\theta_1}{4 \pi R_1} \, exp \, (ikR_1) \qquad\qquad 1\text{-}10$$

R_1 is the distance from the surface to the receiving position. How-

ever, the normalising term should be that of the image solution, by

virtue of a plane surface being considered. But since a Fraunhofer

phase approximation is used by Beckmann and Spizzichino in evaluating

the scattering integral, for the response of a plane surface, the

image solution is not obtained. Fortunately the normalised coherent

intensity is the same as when the scattering integral is correctly

evaluated to give the image solution, although without the normali-

sation this would not be the case. However, the incoherent intensity

is incorrect when normalised.

Horton and Melton (19) extended the analysis for a rough surface

from a Fraunhofer to a Fresnel approximation and compared their pre-

dicted mean intensities with measured values at one frequency in the

specular direction, and found the Fresnel approximation gave better

agreement with observed data. However, the expression for the reflec-

tion from a plane surface was not the image solution. Boyd and Deavenport

(20) considered the question of a Fraunhofer phase approximation in the

scattering integral with particular reference to obtaining the image

solution when the surface roughness is allowed to tend towards zero.

Using Green's functions to calculate the coherent intensity and

evaluating the resulting integral using the stationary phase method,

an expression was obtained consistent with the image solution when the surface becomes plane. Clay and Medwin (21) also obtained the same solution from a realisation that the complete evaluation of the Helmholtz integral for a plane surface would yield the image solution. The correct form for the coherent pressure is given by

$$\langle p \rangle = \frac{RGD_0}{(R_0 + R_1)} \exp[\imath k(R_0 + R_1)] . \langle \exp(\imath kh\gamma) \rangle \qquad \text{1-11}$$

where G is a constant containing source terms, D_0 is the directivity function, $\gamma = -(\cos\theta_1 + \cos\theta_2)$, R_0 is the distance from the surface to the receiver, R is reflection coefficient of the rough surface and $\langle \exp(\imath kh\gamma) \rangle$ is the characteristic function of the surface and gives the effect which roughening a plane surface has upon the average reflected coherent pressure. For a Gaussian height distribution, the characteristic function is given by $\exp[-(g/2)]$, where g has been defined previously, and is known as the roughness parameter. As the surface roughness tends to zero $\langle \exp(\imath kh\gamma) \rangle = \exp[-(g/2)] \underset{h\to 0}{\longrightarrow} 1$ and the image solution is obtained. Boyd and Deavenport normalised the calculated intensity with the image solution, and used a heuristic argument on Beckmann and Spizzichino's solution to obtain the total scattered intensity given by

$$\frac{\langle I \rangle}{I_0} = D_0^2 \exp(-g) + \frac{AF^2 k^2 (R_0 + R_1)^2 T^2}{4\pi R_0^2 R_1^2} \exp(-g)$$

$$\left(\sum_{n=1}^{\infty} \frac{g^n}{n n!} \exp\left[-\frac{k^2 V_0^2 T^2}{4n} \right] [1 - D_0^2 \exp(-g)] \right) \qquad \text{1-12}$$

where

$$V_0^2 = V^2(\theta_1, \theta_2, 0) = (\text{Sin } \theta_1 - \text{Sin } \theta_2)^2$$

$$F = \text{Cos}\theta_1 F_1(\theta_1, \theta_2, 0) = \frac{1 + \text{Cos } \theta_1 \text{ Cos } \theta_2 - \text{Sin } \theta_1 \text{ Sin } \theta_2}{(\text{Cos } \theta_1 + \text{Cos } \theta_2)}$$

and all the other terms have been previously defined. The normalised coherent part is identical to that of equation 1-8 but the incoherent normalised intensity is different. The range, area, angle and frequency dependence of the incoherent component are different to those in equation 1-8. Reasonable agreement was obtained when the experimental scattering data of Welton, Frey and Moore (22), on the angular distribution of the mean scattered intensity at three frequencies, was compared with the predictions of equation 1-12. This demonstrated the correctness of the normalisation used.

At low frequencies when g<<1 the first term on the right hand side of equation 1-12, the coherent term, again dominates. Clay, Medwin and Wright (23) investigated the coherent component for a wind driven water surface with an approximate Gaussian height distribution and observed the exponential decrease in intensity with increasing frequency for small values of g. However, because the probability density function was not ideally Gaussian, the experimental values deviated from the simple exponential function for values of g>3. Bruno, Novarini and Vara (24) considered the independence of the coherent component from the surface autocorrelation function. They found that for Gaussian and non-Gaussian surfaces when using the Helmholtz-Kirchhoff approach with the Fraunhofer phase approximation, the coherent pressure was a function of the probability density

distribution of the surface heights only, regardless of the cor-
relation function. For large values of g in the specular direction
the dominating incoherent normalised intensity becomes

$$\frac{<I>}{I_0} = \frac{A}{16\pi} \frac{(R_0 + R_1)^2}{R_0^2 R_1^2} \frac{T^2}{h^2}$$

1-13

This shows a mean normalised intensity with an angular and frequency
independence which for fixed ranges and areas of insonification is
only dependent on the mean square surface slope, defined as ah^2/T^2.

Although Boyd and Deavenport used an improved method to calculate
the coherent scattered intensity, the incoherent was still obtained
using the Fraunhofer phase approximation, derived by a heuristic
modification of Beckmann and Spizzichino's expression for the integral
of the incoherent intensity. This modified form was, however, cor-
rectly normalised. Clay and Medwin (11) outline an approach which
improves on the linear phase approximation. Second order terms are
retained in the phase components of the scattering integral. This
Fresnel phase approximation is developed in the present study for
predicting the scattered intensity.

1.4 Present Investigation

At the beginning of this study the majority of laboratory
scattering measurements in underwater acoustics on model rough sur-
faces had concentrated on the angular distribution of the ensemble

average scattered intensity. Most measurements were taken at distances from the rough surface which were large compared with the area insonified, and usually at a single frequency or over a narrow bandwidth. Much of the data collected under these conditions has been compared with theoretical predictions based upon an evaluation of the Helmholtz-Kirchhoff integral, using a Fraunhofer phase approximation, as outlined in the previous section.

In the present investigation the ensemble average scattered intensity from a model rough surface is measured. However, the frequency response of the scattered intensity rather than the angular distribution is considered. Normal incidence backscattered intensity measurements from a rough surface are presented, principally in the range 20-300 kHz, although some measurements were taken between 600-1200 kHz. The transducer and hydrophone were gradually changed from positions where the insonified area was large compared with their distances to the surface, to positions where the separation of the transducer and hydrophone from the rough surface were closer in value to the diameter of the insonified region. Predicted intensities based on a Fraunhofer evaluation of the scattering integral and a Fresnel approximation, developed in chapter 2, are compared with the measured values of the ensemble average scattered intensity.

A model rough surface of dimensions 60 x 65 x 3.5 cm was constructed from a low density polyurethane foam. The surface statistics were designed to be Gaussian, with a root-mean-square height and autocorrelation length, compatible with obtaining predominantly coherent scattering at the low frequencies, and incoherent at the high frequencies.

The parametric array was utilised to obtain a source with sufficient bandwidth performance and high enough directivity, to conduct the investigation between 20-300 kHz. The parametric or virtual end-fire array is a volumetric array brought into being by the nonlinear interaction of two intense coaxial sound beams propagating simultaneously through the water. Intermodulation frequencies are generated by the interaction, and the lowest frequency produced, which is the difference in primary frequencies, is particularly useful because it has a very narrow beamwidth, and can be readily varied over a broad range of low frequencies by small changes in the primary frequencies. An experimental study was carried out which demonstrates the feasibility of using the parametric array in the context of the laboratory scattering measurements undertaken.

All the scattering measurements were made in a fibre-glass tank of dimensions 110 x 122 x 245 cm. Gantry facilities were manufactured and fitted onto the tank which allowed the freedom of movement for the transmitter and receiver necessary to conduct the measurements required. A framework was built to house the rough surface underwater which could be manoeuvred to obtain the alignment needed for normal incidence backscattering experiments. Transmitting electronics were constructed which delivered two high frequency quasi-monochromatic signals onto a broadband transducer which launched them simultaneously into the water to generate the parametric array. A receiver system filtered out the primary frequencies, and the broadband of difference frequencies available were employed to make measurements.

The theoretical development used to predict the scattered intensity is based upon the Helmholtz integral with the Kirchhoff

approximations. This method was outlined in the previous section. The derivation particularly draws on the second order phase approximation presented in reference (11). The scattering integral is developed for a general random surface, and evaluated for the particular case of a surface with a Gaussian height distribution and Gaussian autocorrelation function. The directivity of the transmitted radiation is assumed to have a Gaussian profile. The expression derived predicts the ensemble average intensity for any angle of incidence and scattering at any frequency. However, since multiple scattering and shadowing are neglected very rough surfaces and low grazing angles are poorly modelled.

The calculated scattered intensities are compared with measured values of the near normal incidence backscattered intensities. For the first set of experiments the transducer remains at a fixed distance of 100 cm from the surface and an on-axis hydrophone measures the scattered field at 70, 50, 30 and 20 cm, from the rough surface between 20-300 kHz. In a second series of measurements the transducer also moves closer to the rough surface. The hydrophone occupies the same distances from the surface and a similar frequency range is covered, however, this time the distance between the transducer and the surface is 86, 66, 46 and 36 cm respectively. Measurements are also presented on the coherent component of the scattered intensity between 20-100 kHz. Further observations of the backscattered intensity were made over the frequency band 600-1200 kHz.

Although a parametric source is used for the majority of measurements the observations made are generally applicable and not unique to

the virtual end-fire array. The evaluation of the scattering integral
is also derived without any particularisation in the development due
to the use of the parametric array.

Chapter 2   Theoretical Development

2.1   Basic Expression For The Scattering Integral

The basis of the development is the Helmholtz integral. As explained in the previous chapter this relates the reflected pressure on the surface p, estimated using Kirchhoff's equations, to the pressure $p(r_1)$ at a point r_1 above the surface. Using equation 1-4 in chapter 1 gives,

$$p(r_1) = \frac{R}{4\pi} \int_s [p(i)\frac{\partial}{\partial n}(\frac{\exp(ikr_1)}{r_1}) + \frac{\exp(ikr_1)}{r_1}\frac{\partial p}{\partial n}(i)] \, dS \qquad 2\text{-}1$$

Where R is the reflection coefficient of the surface, and n is the surface normal. The Kirchhoff method is a first approximation for smoothly varying surfaces. This approximation has been considered by Mintzer (25) and Meecham (26), and appears to be valid for a surface with small slopes and large radii of curvature relative to the insonifying wavelength. For a slowly changing rough surface, effects due to shadowing and multiple scattering can be neglected for non-grazing angles.

For a directional spherically spreading harmonic source the incident radiation, with the time dependence suppressed, is given by

$$p(i) = \frac{GD}{r_0} \exp(ikr_0) \qquad 2\text{-}2$$

Where G contains the source terms, D is the directivity function,

and r_0 is the distance from the transducer to the rough surface.

Substituting equation 2-2 into 2-1 yields

$$p(r_1) = \frac{RG}{4\pi} \int_s D \left[\frac{\exp(ikr_0)}{r_0} \frac{\partial}{\partial n}\left(\frac{\exp(ikr_1)}{r_1}\right) + \frac{\exp(ikr_1)}{r_1} \frac{\partial}{\partial n}\left(\frac{\exp(ikr_0)}{r_0}\right)\right] dS$$

$$2-3$$

2.2 Scattering Geometry

Using figure 1, $r_0 + r_1$ can be written as

$$r_0 + r_1 = [(R_0 \sin\theta_1 + x)^2 + (R_o \cos\theta_1 - \zeta)^2 + y^2]^{\frac{1}{2}} + [(R_1 \sin\theta_2 \cos\theta_3$$

$$- x)^2 + (R_1 \sin\theta_2 \sin\theta_3 - y)^2 + (R_1 \cos\theta_2 - \zeta)^2]^{\frac{1}{2}} \qquad 2-4$$

Rearranging equation 2-4 yields

$$r_0 + r_1 = R_0 \left[1 + \left(\frac{2x\sin\theta_1}{R_0} - \frac{2\zeta\cos\theta_1}{R_0} + \frac{(x^2 + y^2 + \zeta^2)}{R_0^2}\right)\right]^{\frac{1}{2}}$$

$$+ R_1 \left[1 + \left(\frac{2x\sin\theta_2\cos\theta_3}{R_1} - \frac{2y\sin\theta_2\sin\theta_3}{R_1}\right.\right.$$

$$\left.\left. - \frac{2\zeta\cos\theta_2}{R_1} + \frac{x^2 + y^2 + \zeta^2}{R_1^2}\right)\right]^{\frac{1}{2}} \qquad 2-5$$
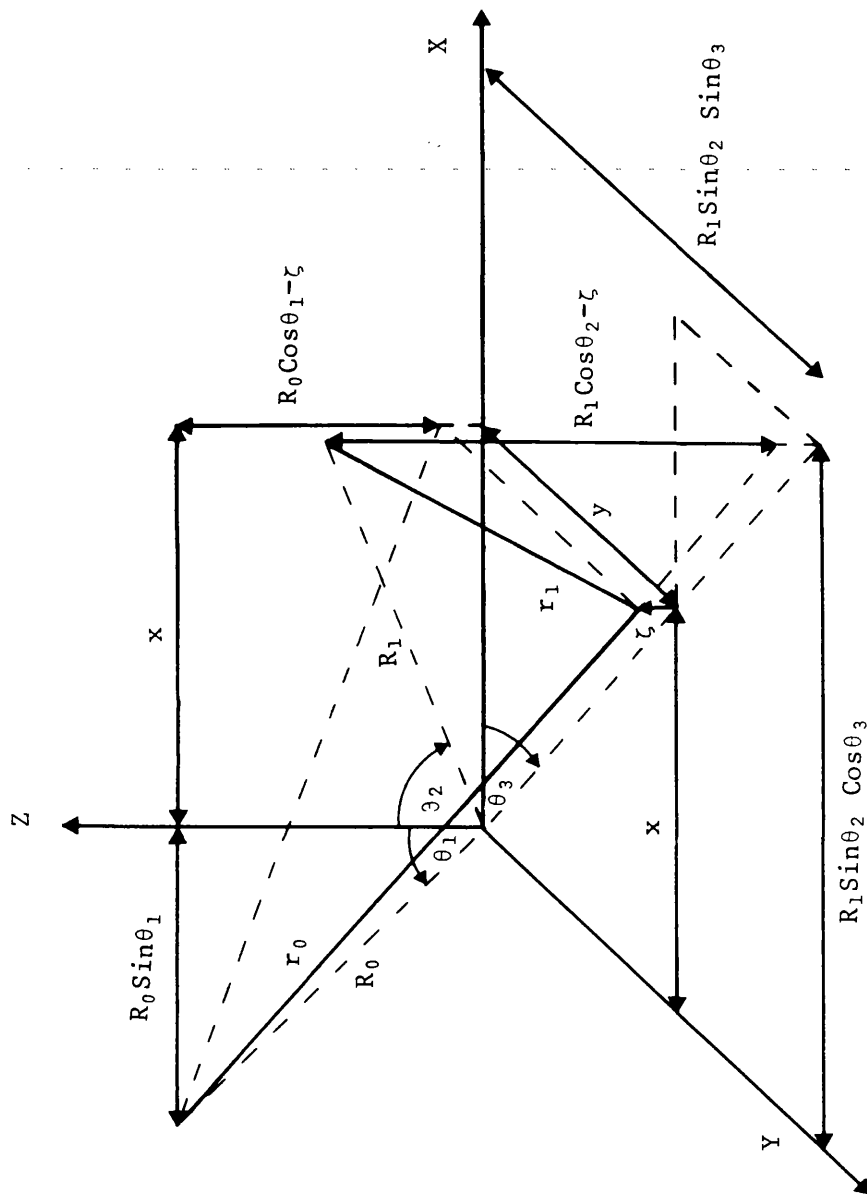
Fig 1 The geometry of the scattering problem.

To obtain the normal derivative of the terms in the scattering

integral of equation 2-3 an approximation for the expression of

$r_0 + r_1$ in equation 2-5 is made. For a highly directional source

the assumption that $x \ll R_0$ and $x \ll R_1$, and $y \ll R_0$ and $y \ll R_1$ may be

made. For small surface undulations $\zeta \ll R_0$ and $\zeta \ll R_1$. This allows a

simplification by carrying out a binomial expansion on the expres-

sion for $r_0 + r_1$ which will be utilised in the following sections.

2•3 Calculation Of The Normal Derivative

Reconsidering equation 2-3 an approximation can be made for

the normal derivative. The normal derivative can be written as

$$\frac{\partial}{\partial n} \left(\frac{\exp(ikr)}{r} \right) = \frac{ik}{r} \exp(ikr) \left(1 - \frac{1}{ikr} \right) \frac{\partial r}{\partial n} \qquad 2\text{-}6$$

which for $ikr \gg 1$ gives

$$p(r_1) = \frac{ikRG}{4\pi r_0 r_1} \int_s D \left(\frac{\partial r_0}{\partial n} + \frac{\partial r_1}{\partial n} \right) \exp(ik[r_0 + r_1]) dS \qquad 2\text{-}7$$

Using the standard vector relationship $\partial \emptyset / \partial n = \hat{n} \cdot \nabla \emptyset$ where $\emptyset$ is a

scalar quantity, and $\hat{n}$ is a normal unit vector, results in;

$$p(r_1) = \frac{\imath kRG}{4\pi r_0 r_1} \int_S D.\hat{\underset{\sim}{n}} \cdot \nabla(r_0 + r_1) \exp(\imath k[r_0 + r_1])dS \qquad 2\text{-}8$$

Bourne and Kendall (27) show for a surface such that $\zeta = f(x, y)$ then

$$\hat{\underset{\sim}{n}} = (- \hat{\underset{\sim}{x}}f_x - \hat{\underset{\sim}{y}}f_y + \hat{\underset{\sim}{z}})/\surd (f_x^2 + f_y^2 + 1) \qquad 2\text{-}9$$

$$dS = \surd(f_x^2 + f_y^2 + 1)\ dxdy \qquad 2\text{-}10$$

where f_x and f_y are the partial derivatives of the height distribution with respect to x and y. Expanding equation 2-5 while retaining only first order terms in ζ, x and y, in the gradient term yields

$$r_0 + r_1 = R_0 + R_1 + \alpha x + \beta y + \gamma \zeta \qquad 2\text{-}11$$

with

$$\alpha = \text{Sin}\,\theta_1 - \text{Sin}\,\theta_2 \text{Cos}\,\theta_3 \qquad 2\text{-}12a$$

$$\beta = -Sin\theta_2 Sin\theta_3 \qquad\qquad 2\text{-}12b$$

$$\gamma = -(Cos\theta_1 + Cos\theta_2) \qquad\qquad 2\text{-}12c$$

Using equations 2-9, 2-10, 2-11 and 2-12 in 2-8 gives

$$p(r_1) = \frac{ikRG}{4\pi R_0 R_1} \int\int_{-\infty}^{\infty} D.(-\alpha f_x - \beta f_y + \gamma) \cdot exp(ik[r_0 + r_1]\ dxdy \qquad 2\text{-}13$$

When the dimensions of the insonified area are much larger than the incident wavelength equation 2-13 can be simplified by using integration by parts on the f_x and f_y terms. Tolstoy and Clay (28) show that under this condition equation 2-13 simplifies to

$$p(r_1) = \frac{ikRG}{4\pi R_0 R_1} \frac{\alpha^2 + \beta^2 + \gamma^2}{\gamma} \int\int_{-\infty}^{\infty} D\ exp\ (ik[r_0 + r_1])\ dxdy \qquad 2\text{-}14$$

This can be rewritten as

$$p(r_1) = \frac{-ikRGF}{2\pi R_0 R_1} \int\int_{-\infty}^{\infty} D\ exp(ik[r_0 + r_1])\ dxdy \qquad 2\text{-}15$$

where

$$F = \frac{1 + \cos\theta_1\cos\theta_2 - \sin\theta_1\sin\theta_2\cos\theta_3}{\cos\theta_1 + \cos\theta_2}$$

The approximations used to obtain equation 2-15 requires the surface irregularities and area of insonification to be small compared with the transmitter and receiver distances. The insonified area should also be large compared with the incident wavelength.

2.4   Second Order Expansion

In section 2.3 a first order expansion for $r_0 + r_1$ was used to obtain the normal derivative. However, in evaluating the phase term a second order expansion is required for $r_0 + r_1$ to obtain the image solution when the surface becomes plane. This gives

$$r_0 + r_1 = R_0 + R_1 + \alpha x + \beta y + \gamma \zeta + U_x x^2 + U_y y^2 \qquad \text{2-16}$$

where

$$U_x = \tfrac{1}{2} \left(\frac{\cos^2\theta_1}{R_0} + \frac{1 - \sin^2\theta_2\cos^2\theta_3}{R_1} \right) \qquad \text{2-17a}$$

$$U_y = \tfrac{1}{2} \left(\frac{1}{R_0} + \frac{1 - Sin^2\theta_2 Sin^2\theta_3}{R_1} \right) \qquad\qquad 2\text{-}17b$$

Substituting 2-16 into 2-15 yields

$$p(r_1) = - \frac{ikRGF}{2\pi R_0 R_1} \int\int_{-\infty}^{\infty} D \, exp \, (ik[R_0 + R_1 + \alpha x + \beta y + \gamma\zeta + U_x x^2 + U_y y^2])dxdy$$

$$2\text{-}18$$

Equation 2-18 is identical with that of Clay and Medwin (11) and is used here to calculate the coherent and incoherent components of the total scattered intensity in an arbitary direction for any incident frequency using a Fresnel phase approximation. Allowing $U_x = U_y = 0$ gives the Fraunhofer approximation.

2.5 Coherent Component Of The Scattered Pressure

To calculate the coherently scattered pressure the ensemble average of the pressure with regard to phase is required. The random character of the surface only enters through the height function, ζ , and this is the term averaged over. Equation 2-18 now becomes

$$<p(r_1)> = - \frac{ikRGF}{2\pi R_0 R_1} \int\int_{-\infty}^{\infty} D \, exp(ik[R_0 + R_1 + \alpha x + \beta y + U_x x^2 + U_y y^2])$$

$$<exp(ik\gamma\zeta)> \, dxdy \qquad\qquad 2\text{-}19$$

where < > represents the emsemble average value. The average value
within the integral is only dependent on the height distribution
and is given by

$$\langle \exp(\imath k\gamma\zeta)\rangle = \int_{-\infty}^{\infty} w(\zeta) \exp(\imath k\gamma\zeta) \, d\zeta \qquad\qquad 2\text{-}20$$

which is the characteristic function of the height probability
density distribution $w(\zeta)$. The mean coherent pressure can now be
written as

$$\langle p(r_1)\rangle = -\frac{\imath kRGF}{2\pi R_0 R_1} \langle \exp(\imath k\gamma\zeta)\rangle \int\!\!\int_{-\infty}^{\infty} D \exp(\imath k[R_0 + R_1$$

$$+ \alpha x + \beta y + U_x x^2 + U_y y^2]) dx dy \qquad\qquad 2\text{-}21$$

The integral contains the solution for $\zeta = 0$, that of a plane surface.
For a plane surface the reflected intensity will be concentrated in
the specular direction, and in this case

$$F = \cos\theta$$

$$\alpha = \beta = 0$$

$$U_x = R_s \cos^2\theta$$

$$U_y = R_s$$

where

$$R_s = (1/2)((1/R_0) + (1/R_1))$$

The integral can now be written as

$$\Gamma_0 = \int\int_{-\infty}^{\infty} D \exp(\imath k(R_0 + R_1)[1 + ((x^2 R_s \cos^2\theta_1 + y^2 R_s)/(R_0 + R_1))]) dxdy$$

2-22

This integral can be evaluated using the method of stationary phase. From Born and Wolf (29) a double integral of the form

$$\Phi = \int\int g(x, y) \exp(\imath t f(x, y)) dxdy$$
$\qquad$ 2-23

can be evaluated in a region where $g(x, y)$ is slowly changing and

$$\partial f/\partial x = \partial f/\partial y = 0$$
$\qquad$ 2-24

For large, positive and real values of t the integral asymptotically approaches a value given by

$$\Phi = \frac{2\pi\iota\sigma}{\sqrt{|ab - c^2|}} g(x_0, y_0) \frac{\exp(\iota t f(x_0, y_0))}{t} \qquad 2\text{-}25$$

where

$$a = (\partial^2 f/\partial x^2)x_0$$

$$b = (\partial^2 f/\partial y^2)y_0$$

$$c = (\partial^2 f/\partial x \partial y)x_0, y_0$$

The positive root is taken and

$$\sigma = \begin{cases} + 1 & \text{for } ab > c^2 & a > 0 \\ - 1 & \text{for } ab > c^2 & a < 0 \\ - \iota & \text{for } ab < c^2 \end{cases}$$

Since $k(R_0 + R_1) \gg 1$, and at the origin of equation 2-22 the value for the partial derivatives are zero, and D is slowly varying, then the stationary phase method can be used to evaluate the integral giving

$$\Gamma_0 = \frac{D\pi\iota}{kR_s\cos\theta} \exp(\iota k[R_0 + R_1]) \qquad 2\text{-}26$$

Combining this value of 2-26 with the terms in front of the integral in equation 2-21 yields

$$\langle p \rangle \quad = \frac{RGD}{(R_0 + R_1)} \exp(ik[R_0 + R_1]) \langle \exp(ik\gamma\zeta) \rangle \qquad 2\text{-}27$$

where the nemonclature of $\langle p \rangle$ has been used for the coherent pressure. If a Fraunhofer phase approximation had been used in the argument of the exponent in equation 2-19, then the value of $\langle p \rangle$ would not have the form given here, which reduces to the image solution for $\zeta = 0$, but would have been similar to that given in equation 1-10 of the previous chapter. The characteristic function needed to evaluate the coherent component can be introduced later after the incoherent component of intensity has been obtained.

2.6 Incoherent Component Of The Scattered Intensity

The incoherent intensity is the difference between the total and coherent scattered intensity. The total intensity is the product of the pressure with its complex conjugate. Using equations 2-18 and 2-19 to formulate the total and coherent intensity respectively, the average incoherent intensity $\langle I \rangle_{IC}$ can be expressed in bivariate form as

$$\langle I \rangle_{IC} = \frac{k^2 R^2 G^2 F^2}{8\pi^2 \rho c R_0^2 R_1^2} \int\int\int\int D \ D' \exp(\iota k[\alpha(x-x') + \beta(y-y') + U_x(x^2-x^{2\,\prime})$$

$$+ \ U_y(y^2-y'^2)]) \ (\langle\exp(\iota k\gamma[\zeta-\zeta'])\rangle$$

$$- \langle\exp(\iota k\gamma\zeta)\rangle\langle\exp(-\iota k\gamma\zeta')\rangle\rangle)dxdy \ dx'dy' \qquad 2\text{-}28$$

ρ and c are the ambient density and velocity of sound in the fluid respectively. The first term in the bracket containing the average expressions is the two-dimensional characteristic function of the bivariate height distribution, $w(\zeta, \zeta')$, for the surface. This is given by

$$\langle\exp(\iota k\gamma[\zeta-\zeta'])\rangle = \int\int_{-\infty}^{\infty} w(\zeta, \zeta') \ \exp(\iota k\gamma[\zeta-\zeta']) \ d\zeta d\zeta' \qquad 2\text{-}29$$

To solve the integral of equation 2-28, an expression for the directivity function of the transducer, D, is required. A Gaussian form is used since this in reasonable agreement with the experimental beam patterns, and leads to an analytic form for $\langle I \rangle_{IC}$. Using such a form gives

$$D = \exp(-[(x^2/X^2) + (y^2/Y^2)]) \qquad 2\text{-}30$$

were $X = X_0/Cos\theta_1$ and $Y = Y_0$. X_0 and Y_0 are the $1/e$ points on the directivity pattern at right angles to the acoustic axis, and are equal for an axisymmetric transducer. θ_1 is the angle of incidence to the surface given in figure 1.

Introducing the change of variables

$$x = x'' + \epsilon/2 \qquad \text{a)} \qquad y = y'' + \eta/2 \qquad \text{c)}$$

$$2\text{-}31$$

$$x' = x'' - \epsilon/2 \qquad \text{b)} \qquad y' = y'' - \eta/2 \qquad \text{d)}$$

allows an integration over x'' and y'', and approximations in the second order terms U_x, U_y, and allowing $X_0 \sim Y_0 = W$ in the integral, produces a simplification. This is carried out in Appendix A, and yields

$$<I>_{IC} = \frac{k^2 R^2 G^2 F^2 XY}{16\pi\rho c R_0^2 R_1^2} \int\int_{-\infty}^{\infty} \exp(-[(\epsilon^2 + \eta^2)s]) \exp(\iota k[\alpha\epsilon + \beta\eta])$$

$$(<\exp(\iota k\gamma[\zeta-\zeta'])>-<\exp(\iota k\gamma\zeta)><\exp(-\iota k\gamma\zeta')>)$$

$$d\epsilon d\eta \qquad 2\text{-}32$$

where

$$s = (1/2)[(1/W)^2 + g(R_s W/h\gamma)^2] \qquad 2\text{-}33$$

h is the root-mean-square height of the surface, $g = (hk\gamma)^2$.

As s tends to zero equation 2-32 becomes identical with a

Fraunhofer phase approximation.

Changing to polar co-ordinates allows the integral to be reduced

to a one dimension integral. Applying the identity

$$\frac{1}{2\pi} \int_0^{2\pi} \exp(ik[x\cos\phi + y\sin\phi])d\phi = J_0(k\sqrt{[x^2 + y^2]}) \qquad 2-34$$

where J_0 is the zero order Bessel function enables the integral

over ϕ to be carried out and this gives

$$\langle I \rangle_{ic} = \frac{k^2 R^2 G^2 F^2 XY}{8\rho c R_0^2 R_1^2} \int_0^{\infty} J_0(kr\sqrt{[\alpha^2 + \beta^2]}) \exp(-r^2 s)(\langle\exp(ik\gamma[\zeta-\zeta'])\rangle$$

$$-\langle\exp(ik\gamma\zeta)\rangle\langle\exp(-ik\gamma\zeta')\rangle) \, rdr \qquad 2-35$$

This is the incoherent component of the intensity, which can be

evaluated for specific probability density functions. To preserve

generality the dependence of the characteristic functions on ϵ, η,

and ζ, and r and ζ, has remained implicit.

2.7 Total Scattered Intensity

The coherent and incoherent expressions can be combined to give the total intensity $\langle I \rangle_T$ as,

$$\langle I \rangle_T = \frac{R^2 G^2 D^2}{2\rho c (R_0 + R_1)^2} \langle \exp(\imath k\gamma\zeta) \rangle \langle \exp(-\imath k\gamma\zeta') \rangle$$

$$+ \frac{k^2 R^2 G^2 F^2 XY}{8\rho c R_0 R_1} \int_0^\infty J_0(kr\sqrt{[\alpha^2 + \beta^2]}) \exp(-r^2 s)(\langle \exp(\imath k\gamma[\zeta-\zeta']) \rangle$$

$$-\langle \exp(\imath k\gamma\zeta) \rangle \langle \exp(-\imath k\gamma\zeta') \rangle) \, r \, dr \qquad\qquad 2\text{-}36$$

To simplify equation 2-36 expressions are required for the characteristic functions. The surface used in the experimental work had approximately Gaussian statistics, and using this type of distribution gives

$$\langle \exp(\imath k\gamma\zeta) \rangle \langle \exp(-\imath k\gamma\zeta') \rangle = \exp(-g) \qquad\qquad 2\text{-}37a$$

$$\langle \exp(\imath k\gamma(\zeta-\zeta') \rangle = \exp(g[1-C]) \qquad\qquad 2\text{-}37b$$

C is the normalised auto-correlation function for the surface, and is given by

$$C = \langle \zeta\zeta' \rangle / \langle \zeta^2 \rangle \qquad\qquad 2\text{-}38$$

Substituting 2-37a and 2-37b into 2-36 yields

$$\langle I \rangle = \frac{R^2 G^2 D^2}{2\rho c (R_0 + R_1)^2} \exp(-g) + \frac{k^2 R^2 G^2 F^2 XY}{8\rho c R_0{}^2 R_1{}^2} \int\limits_{o}^{\infty} J_0 (kr\sqrt{[\alpha^2 + \beta^2]}) \exp(-r^2 s)$$

$$(\exp(-g[1-C]) - \exp(-g)) \, r dr \qquad \text{2-39}$$

The characteristic functions in the integral can be rewritten in the form of a series as

$$\exp(-g[1-C]) - \exp(-g) = \exp(-g) \sum_{n=1}^{\infty} \frac{g^n C^n}{n!} \qquad \text{2-40}$$

A Gaussian auto-correlation function is in reasonable agreement with the model rough surface measurements and can be given by

$$C = \exp(-r^2/T^2) \qquad \text{2-41}$$

where T is the autocorrelation length.

Using the series expansion in equation 2-40 with a Gaussian autocorrelation function, and utilising the Bessel function integral

$$\int_0^\infty J_0(ar)\exp(-r^2/b^2)r\,dr = \frac{b^2}{2}\exp(-a^2b^2/4) \qquad\qquad 2\text{-}42$$

while letting

$$V = \sqrt{[\alpha^2 + \beta^2]} \qquad\qquad 2\text{-}43$$

allows $\langle I\rangle_T$ to be expressed as

$$\langle I\rangle_T = \frac{R^2 G^2 D^2}{2\rho c(R_0 + R_1)^2}\exp(-g) + \frac{R^2 G^2 F^2 XY}{16\rho c R_0^2 R_1^2}\frac{T^2}{h^2\gamma^2}L(g) \qquad\qquad 2\text{-}44$$

where

$$L(g) = g\exp(-g)\sum_{n=1}^{\infty}\frac{g^n}{(sT^2 + n)n!}\exp\left(\frac{-g\,B}{4(sT^2 + n)}\right)$$

$$B = \frac{V^2 T^2}{h^2\gamma^2}$$

Equation 2-44 is the expression for the mean intensity scattered from a surface with Gaussian statistics.

2.8 Normalised Intensity

The coherent component can be simplified by normalising $\langle I \rangle_T$ with the value for $\langle I \rangle_T$ in the specular direction for a smooth perfectly reflecting surface. Under these conditions the incoherent component becomes zero, and $\langle I \rangle_T$ is given by I_0 where

$$I_0 = G^2/2\rho c (R_0 + R_1)^2 \qquad\qquad 2\text{-}45$$

This is the image solution. Defining the scattering coefficient S_c as

$$S_c = \langle I \rangle_T / \langle I_0 \rangle \qquad\qquad 2\text{-}46$$

gives

$$S_c = R^2 D^2 \exp(-g) + \frac{R^2 F^2 XY}{8} \frac{(R_0 + R_1)^2}{R_0^2 R_1^2} \frac{T^2}{h^2 \gamma^2} \, L(g) \qquad\qquad 2\text{-}47$$

Equation 2-47 is the total scattered normalised mean intensity from a surface with a Gaussian probability density function and auto-correlation function. It depends upon the transmitter and receiver

positions, the area of insonification, the transducer's directivity function, and the root-mean-square height, correlation length, and reflection coefficient of the surface.

The expression for S_c can be compared with that of reference (20), the result of which is given here in equation 1-12 of chapter 1. The coherent components of the scattered intensity are identical, however, the incoherent response is different due to the presence of s, the lack of the term [1-D exp(-g)], and an extra factor of 2 in the denominator. When g>3 then [1-D exp(-g)]≈1, and the incoherent intensity predicted using equation 2-47 has a maximum value of a half that obtained using equation 1-12 chapter 1, and can have a value much less than this depending on the magnitude of s.

2.9 Calculated Values For L(g) And Its Asymptotic Values

For calculations of L(g) when g<30 better than 1% accuracy can be obtained for L(g) by summing the first fifty terms in the series. For 30<g<50 the first seventy terms suffice. For small or large values of g particularly simple approximations can be made for the specularly scattered radiation. This can be done either by making approximations in the integral of equation 2-39 and then evaluating the integral, or simply by summing the series in equation 2-44; both give the same results. The asymptotic values are

$$L(g) \approx \frac{g^2}{(sT^2 + 1)} \quad g \ll 0.1 \qquad \qquad 2\text{-}48a$$

$$L(g) = \frac{g}{(sT^2 + g)} \quad g \gg 10 \qquad \qquad 2\text{-}48b$$

Figures 2 and 3 show values for L(g). In figure 2 L(g) is calculated for B = 0 and s = 0. From this diagram it can be seen that the approximations in 2-48a and 2-48b are valid. Figure 3 shows the magnitude of L(g) for different values of s and B. All calculations for L(g) in figure 3 use an autocorrelation length of 2 cm, a value of 1.9 cm was measured for the model rough surface.

For the case where $s \ll 1$, so that $sT^2 \ll g$ for all values of g, the expression for L(g) becomes identical to that obtained if U_x and U_y had been neglected in the evaluation of the incoherent scattered intensity. This is the result derived for a linear phase approximation. For some of the calculations in chapter 5 the value of sT^2 does have an important influence upon the magnitude of the predicted scattered intensities.

2.10 Normal Incidence Backscattering

For specular scattering $V = 0$, $F = \cos\theta_1$ and $\gamma = 2\cos\theta_1$. In the particular case of normal incidence specular backscattering, with a circular region insonified on the surface so that $X_0 = Y_0 = W$, equation 2-47 reduces to

$$S_c = R^2 \exp(-g) + \frac{R^2 W^2}{32} \frac{(R_0 + R_1)^2}{R_0^2 R_1^2} \frac{T^2}{h^2} Z(g)$$

$$Z(g) = L(g)(B = 0) = g \exp(-g) \sum_{n=1}^{\infty} \frac{g^n}{(sT^2 + n)n!} \qquad \text{2-49}$$
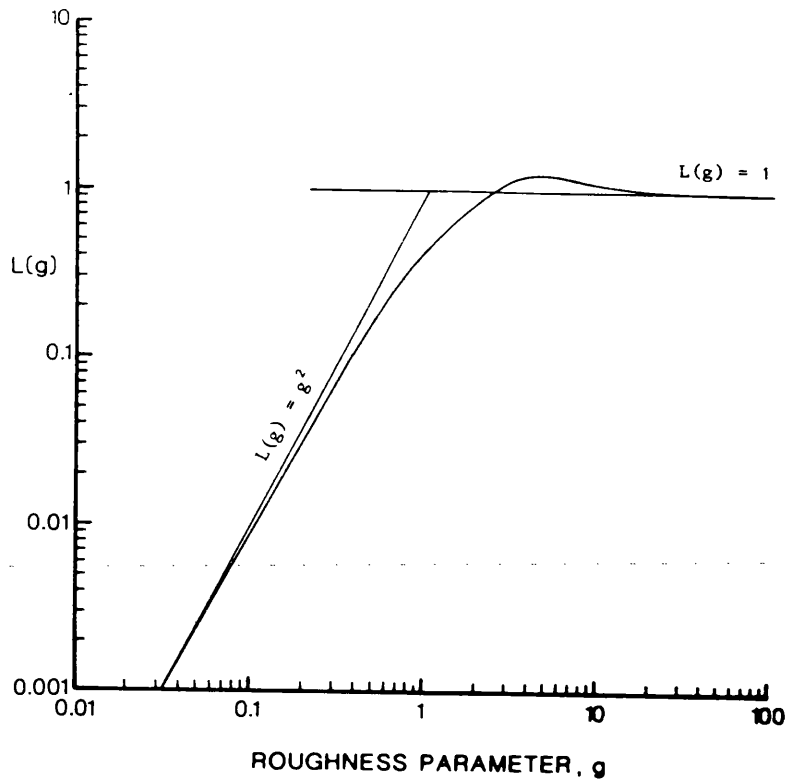
Fig 2   Calculations for L(g), given in text, when B = s = 0.
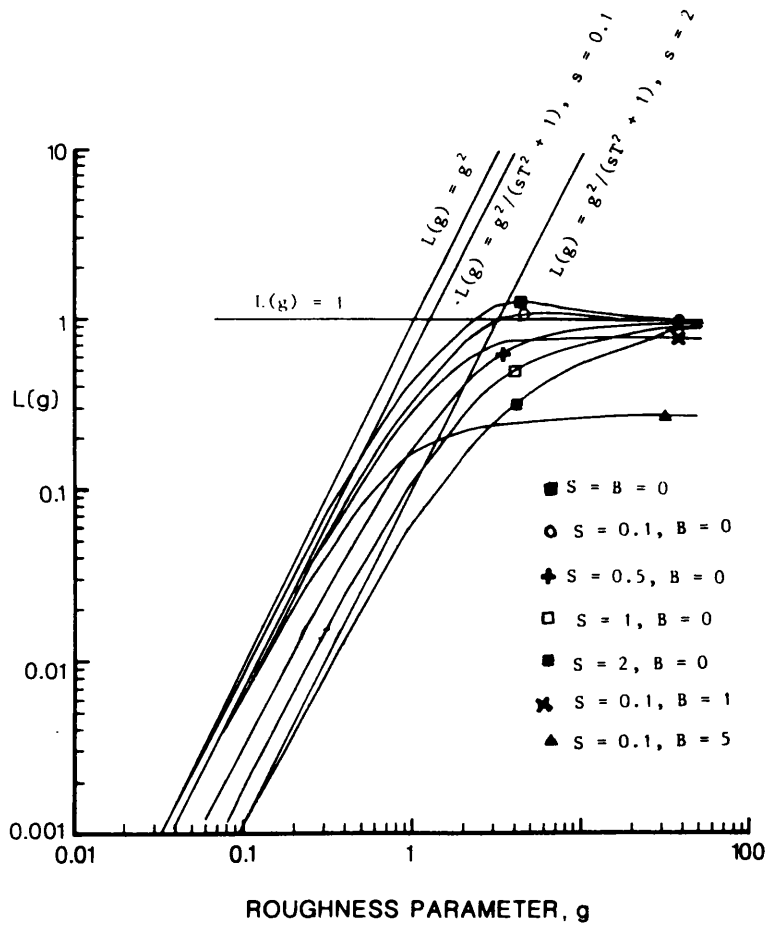
Fig 3 Calculations for L(g) for different values of s and B.

Predicted values for the normalised scattered intensity calculated using equation 2-49 are compared with experimental observations presented in chapter 5. The intensity measurements are made for a range of values of g between 0.14 and 462, with values for R_0, R_1 and W being varied.

To evaluate equation 2-49 values for R, W, R_0, R_1, T, h and k needed to be measured. The measurement of some of these parameters is presented in the following chapters, and an estimate is made of the uncertainty in the predicted intensity arising from the experimental error in the parameters measured.

Chapter 3   Model Rough Surface

3.1   Introduction To Model Rough Surfaces

Investigations on the interaction between underwater acoustic waves and a rough boundary have in many cases centred on the use of constructed models in controlled conditions. This is partly because of the difficulty of collecting accurate and reliable data at sea. Also, the lack of detailed information on sea-bed topography, and wave statistics meant that little critical comparison could be made between observations and theoretical predictions.

Some of these studies were mentioned in the introduction. The pressure release surfaces with sinusoidal profiles in references (6) and (9) were used to investigate contemporary theories. One dimensional pressure release random surfaces in reference (14) were used to investigate the possibility of obtaining information on a surface using acoustic measurements. An important programme in acoustic scattering from rough surfaces has been the construction, using low density expanded polystyrene, of four two dimensional randomly rough surfaces, based on information from aeromagnetic maps of the Canadian Shield. Extensive rough surface work has been carried out using these models which has been presented in references (13), (19), (20) and (22). This work was primarily directed towards the spatial distribution of the scattered intensity; however, the range dependence of the signal level scattered from these sur- faces has also been investigated by Mikesta and McKinney (30).

Surfaces other than those using pressure release materials have also been manufactured. Fung and Leovaris (31) constructed two surfaces made from mild steel, and a third from a rubber polymer with a relatively low reflection coefficient. Numrich and Callen (32) generated rough surfaces under computer control by milling aluminium, and made acoustic scattering measurements up to a roughness parameter 'g' greater than one hundred. Laboratory backscatter experiments on surfaces composed of gravel were also conducted by Markson and Stern(33).

An alternative approach to the creation of a solid rough surface has been the agitation of a water/air interface usually by using a wind tunnel. The rough boundary is observed from below the water surface. An early attempt at using this type of two dimensional randomly rough boundary was carried out in (18), where the surface had been designed to have a roughness with Gaussian height and slope distributions and a Gaussian autocorrelation function. This experimental arrangement was upgraded to allow improved measurements of the surface height distribution and correlation function, and to give better control over the surface statistics as in references (21) and (23). In (23) for example, five centrifugal fans were used to generate the rough boundary for investigating the coherently scattered intensity.

The generation of a randomly rough surface with guaranteed statistics is difficult to achieve using either solid or fluid boundaries. The advantage of a solid rough surface is that it allows the surface statistics and acoustic measurements to be taken relatively easily. However, having a limited area allows

only a limited number of independent random acoustic samples to be taken, and this could restrict the accuracy of the stochastic variable being measured. In the case of an agitated water surface the boundary is rapidly fluctuating in time, and a more sophisticated system is required to measure the surface statistics and collect the acoustic data. An advantage of this approach is that there is no restriction on the number of measurements that can be taken, and this allows higher accuracies to be obtained.

3.2 The Rough Surface Used For This Study

A primary objective in construction was to create a surface with Gaussian statistics, as the theoretical analysis of the previous chapter, highlighted this specific case. The height distribution for such a surface is given by

$$w(\zeta) = \frac{1}{h\sqrt{2\pi}} \exp\left(-\frac{\zeta^2}{2h^2}\right) \qquad 3\text{-}1$$

where h is the root-mean-square height of the surface. The height variation is measured relative to a zero mean plane so

$$\langle \zeta \rangle = 0 \qquad 3\text{-}2$$

$$\langle \zeta^2 \rangle = h^2 \qquad 3\text{-}3$$

Although the height distribution is random, neighbouring points are correlated and an autocorrelation function is also required to

describe the surface. The form required was Gaussian

$$C = \exp\left[-(r^2/T^2)\right] \qquad\qquad 3-4$$

where T is the autocorrelation length.

A solid pressure release surface was chosen to ensure that measurements of the surface statistics, and collection of the acoustic data was relatively straightforward. The frequency range of the investigation was principally in the range 20-300 kHz. The root-mean-square height of the surface was constructed so that the scattered returns were coherent at low frequencies, those in the intermediate range both coherent and incoherent, and those at high frequencies were diffuse. The autocorrelation length was to be consistent with small surface slopes.

3.3 Construction Of The Rough Surface

The material used was expanded polyurethane which has a low density of 47 kgm^{-3}. Some water absorption took place; this stabilised at 82 kgm^{-3}. To reduce absorption the completed model was thinly coated with an oil based paint. This reduced the stabilised density to 64 kgm^{-3}. The velocity in the material was measured as 900 ± 100 ms^{-1} and this gave an acoustic impedence of $(5.8 \pm 0.6).10^4$ $kgm^{-2}s^{-1}$. When this acoustic impedance is used the reflection coefficient between water and expanded polyurethane is approximately 0.92 ± 0.01.

A flat parallel sided slab of the expanded polyurethane foam 50 x 50 cm and 4.5 cm thick was formed to carry out calibration measurements, and this was also covered with the oil based paint. The slab reflection losses, relative to a plane water-air interface, and the transmission loss were measured for the material and the results are shown in fig 1a and 1b. The reflection loss increases with frequency. To obtain flat sides the expanded polyurethane surface was milled level, which exposed the bubble matrix structure of the material at the surface giving a slight roughness. At 200 kHz a root-mean-square height of 200 μm will introduce a loss of -2db into the coherent component of the reflected signal and it could be this weak scattering which is increasing the reflection loss. The transmission loss shows a general increase with frequency which was thought to be due to scattering and absorption by the bubble structure within the material. The polyurethane foam was therefore a reasonably good acoustic reflector underwater, with a high transmission loss which removes effects due to the material being of finite thickness over the frequency range of this study.

The construction of the model rough surface took place in three stages. Initially a rough surface model was fashioned from modelling clay. Secondly a thin sheet of the thermo-plastic was used to form a mould of the clay model. The plastic mould was very thin, 270 μm and was found to be acoustically transparent for the frequencies used. Over the plastic mould was poured a mixture of the two liquids, a phenyl isocyanate composition and a resin. These form the basis of an isofoam series produced by Baxeden Chemicals; the one used was RM18. The mixture flowed
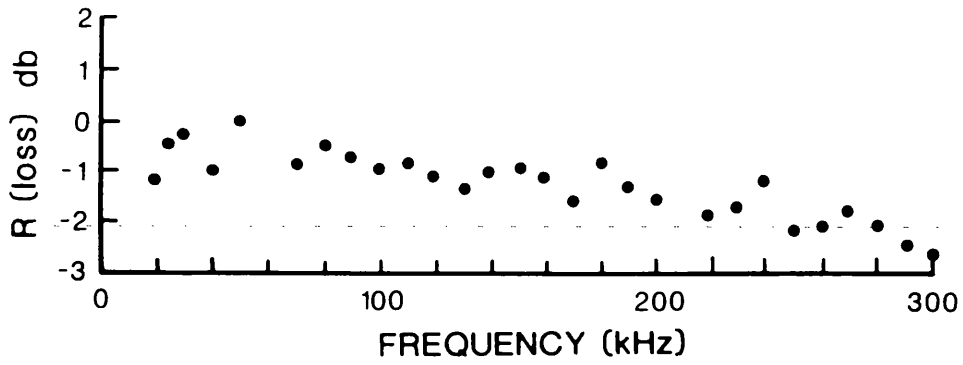
Fig 1a   Reflection loss of the polyurethane foam relative to an
air-water interface.
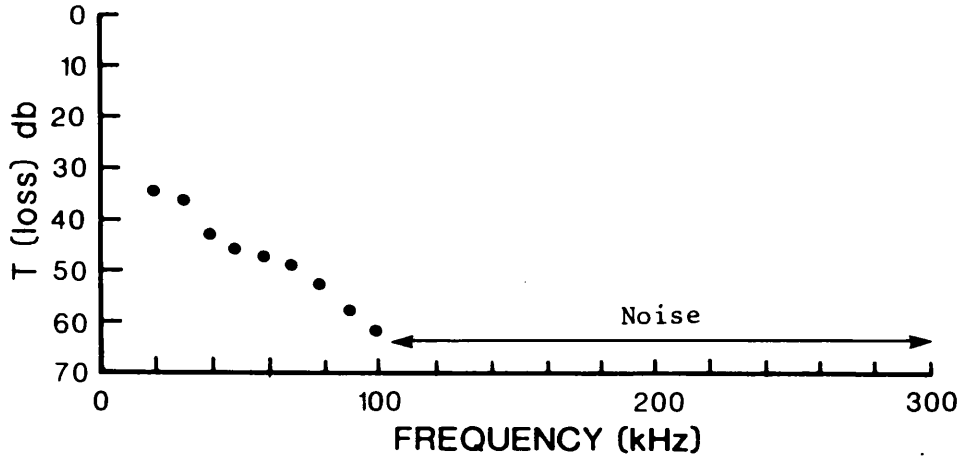
Fig 1b   One way transmission loss through the polyurethane foam.

over the plastic mould expanding to a low density rigid foam

at room temperature with one face almost plane and the other taking

up the shape of the mould and adhering to it. The low density

model rough surface was then thinly coated with the oil paint.

A photograph of the completed surface is shown in figure 2.

3.4 Measurement Of Surface Statistics And Statistical Analysis

3.4.1 Measurement of surface statistics

To measure the surface statistics a contour follower

was made which sampled the profile along a surface section.

Sample points were taken every 2 mm along sections which were

480 mm long, and referred to a fixed height above the rough

surface. The technique is shown in figure 3. Two sets of

profiles were taken at right angles to one another, ten sections

in one direction and nine in the other, each section being

approximately 5 cm apart. The profiles from the contour

follower were then traced onto graph paper, digitised, and

recorded on computer tape for analysis. The size of the surface

was 65 x 60 x 3.5 cm.

3.4.2 Comparison of the surface statistics with a Gaussian
distribution

A typical section is shown in figure 4. A theoretical

Gaussian distribution having the same mean and standard deviation

as the profile is compared with a histogram of the measured height

data. The autocorrelation function was also calculated for the

Fig 2   Model Rough Surface With Six Inch Ruler Showing Scale

Contour Follower

Rough Surface
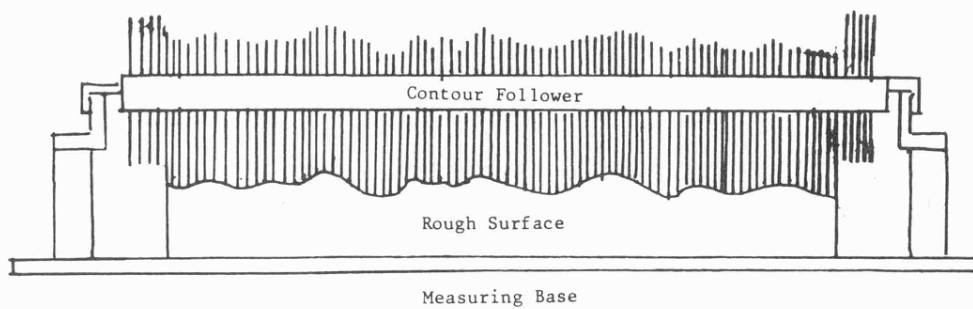
Measuring Base

Fig 3   Contour follower measuring surface statistics.

AUTOCORRELATION FUNCTION

LAG,L (mm)

FREQUENCY

HEIGHT (mm)

HEIGHT (mm)

DISTANCE ACROSS THE SURFACE SECTION (mm)
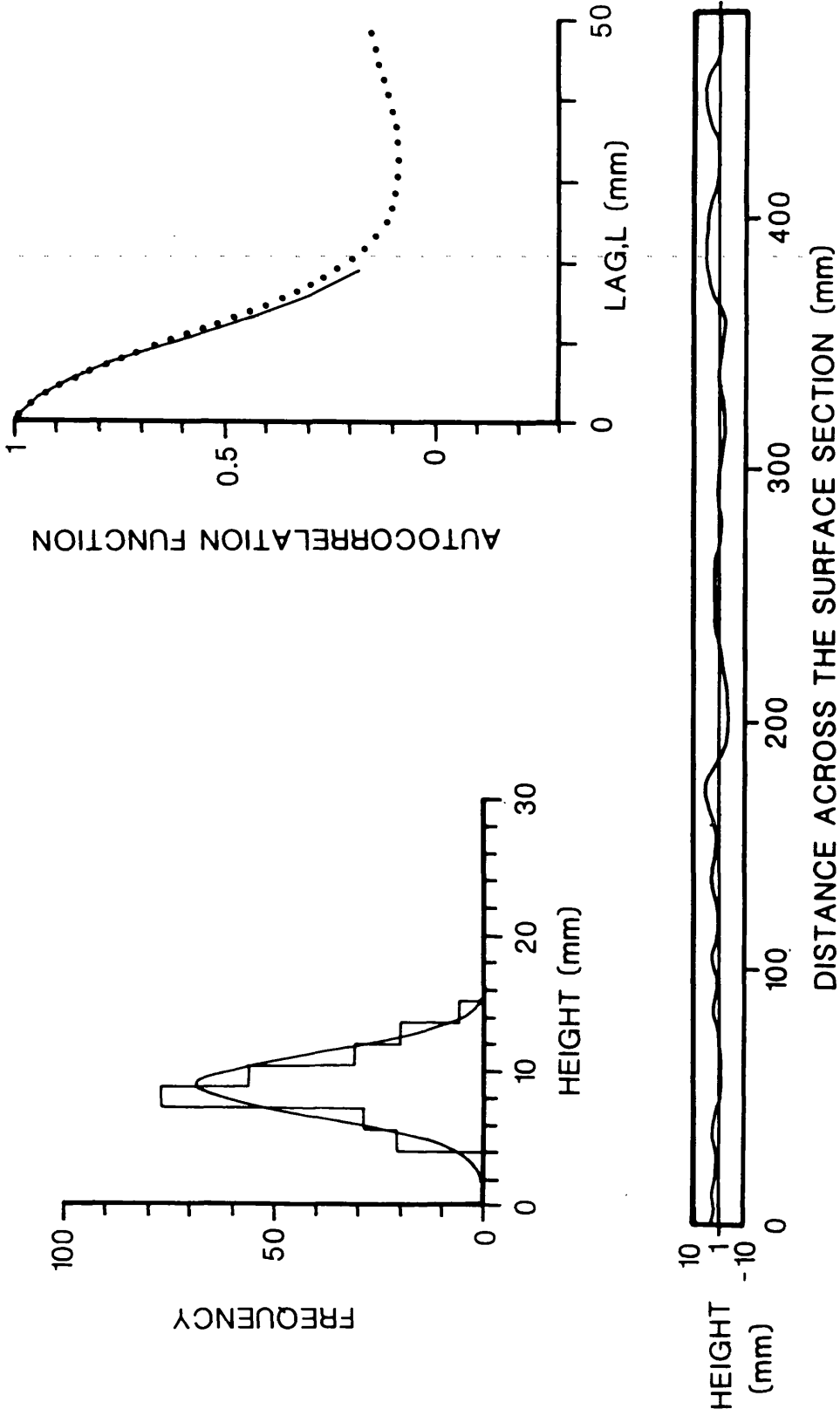
Fig 4 A surface section compared with a Gaussian height
distribution and Gaussian autocorrelation function.

Table (1)

Surface Section	Mean Ht mm	RMS Ht mm	AL ($\equiv$ T) cm
A0	14.37	2.31	1.4
A1	12.92	1.76	1.0
A2	11.91	2.52	1.8
A3	9.89	2.00	1.6
A4	10.32	2.51	2.4
A5	10.80	2.70	1.8
A6	8.81	2.24	1.4
A7	9.23	2.16	1.8
A8	8.28	1.88	2.0
A9	8.88	2.68	2.0
B0	11.76	3.26	2.4
B1	11.63	3.27	2.4
B2	9.78	2.71	2.2
B3	9.80	2.31	1.8
B4	8.32	2.65	1.8
B5	8.76	2.27	1.8
B6	9.57	2.28	2.4
B7	9.95	2.29	2.0
B8	10.85	2.13	1.6

section by removing the mean height from the profile and normal-

ising with the variance of the section, and thus may be written as

$$C[L] = \frac{1}{N} \left[\sum_{i=0}^{N-|L|-1} x_i \cdot x_{i+|L|} \right] / C[0] \qquad L = 0, \pm 1, \pm 2, \ldots \pm N-1 \qquad 3-5$$

A maximum lag of 0.1 of the profile length was used in calculating

the autocorrelation function and a comparison was made with a

Gaussian autocorrelation function fitted above its half value point.

All the profiles are collected together in Appendix 2 and the

important parameters are listed in Table 1.

The surface profiles in Appendix 2 are labelled A0-A9 and

B0-B8, to identify the two sets of sections at right-angles to one

another. The profiles are scaled down as compared with the actual

sections, but the vertical and horizontal reductions are identical,

and thereby give an accurate representation of the original profiles.

The sections are centred on their mean value, and show a correlated

randomly rough surface with small slope values. The height distri-

bution of the profiles are compared with Gaussian curves having the

same standard deviation and mean as the measured values shown in

the histogram. In general, the agreement is good although some

bimodal character and skewness is observed. The autocorrelation

functions are in reasonable agreement with the Gaussian autocorrelation

functions which are compared with the data. Statistical tests are

carried out on these measurements to obtain more objective comparisons.

An analysis can be made of the standard deviation, means
and autocorrelation lengths of the samples, to see if the surface
measurements are consistent with those expected for a surface with
Gaussian features.

3.4.3 Estimate of the number of independent sample points in a section

Generally sampling theory is derived for random data which is
uncorrelated. In the case of sampling a rough surface, neighbouring
points in a section are correlated, and therefore the number of
independent points sampled in a section is much lower than the number
of points sampled when a fine sampling interval is used. The profiles
required fine sampling for the calculation of the autocorrelation
function; however analysis of the statistical parameters of the
sections required the number of independent points in a section to be
known.

The common relationship between the standard deviation of the
sample means $\sigma_{\bar{x}}$ and the population standard deviation σ_{x_p} is given
by

$$\sigma_{\bar{x}}^2 = \frac{\sigma_{x_p}^2}{n} \qquad\qquad 3\text{-}6$$

where n is the number of random uncorrelated observations in the
sample. However, if observations within the sample are correlated
with a correlation function $C_x(\tau)$ then it has been shown by
Bendat and Piersol (34) that

$$\sigma_{\underline{x}}^{2} = \frac{\sigma_{xp}^{2}}{L} \int_{-\infty}^{\infty} C_{x}(\tau) \, d\tau \qquad\qquad 3\text{-}7$$

where L is the sample length. Using the Gaussian autocorrelation

function of equation 3-4 in equation 3-7 yields

$$\sigma_{\underline{x}}^{2} = \frac{\sigma_{xp}^{2}}{(L/T\sqrt{\pi}\,)} \qquad\qquad 3\text{-}8$$

This gives

$$n = \frac{L}{T\sqrt{\pi}} \qquad\qquad 3\text{-}8$$

Each section has 240 observation points 2 mm apart and a mean

autocorrelation length, calculated in Appendix 2, of 19 mm giving

$$n = 14$$

The number of independent points was far fewer than the data

collected.

3.4.4 The Chi-Squared test

A normalised Gaussian curve was used to generate a theo-
retical histogram with calculated values for the number of points
on the surface which lie between certain height levels. These
were then compared with the measured values, and a Chi-Squared
test carried out. The test is defined as

$$\chi^2 = \frac{\sum (O-E)^2}{E} \qquad\qquad 3\text{-}10$$

Where O is the observed value and E the expected. Using the
correct number of independent points in a sample gave

$$\chi^2 = 9.64 \qquad V = 5$$

Where V is the number of degrees of freedom in the system. At
the 5% significance level the hypothesis that the measured values came
from a Gaussian distribution cannot be rejected.

3.4.5 The t-test

This is a test to see if any of the section means differ
significantly from what would be expected of a Gaussian distribution.
The test is

$$t = |u-\bar{x}| / (s/\sqrt{n}) \qquad\qquad 3\text{-}11$$

Where u is the population mean; $\bar{x}$ the mean, s the standard

deviation, and n the number of uncorrelated points in a

sample. Using the t-test sixteen of the nineteen means are

within the 1% significance level and over half are inside the

5% level, however, three lie outside the 1% level indicating a

lack of homogeneity, and this was due to the presence of low

frequency trends in the surface. The mean levels of the 'A' profiles

had a linear trend , and those of 'B' a trend as seen in figure 5.

If all the height readings are pooled together and the

standard deviation calculated when the zero mean is stationary

the standard deviation is equal to the root-mean-square height

of the rough surface. However, when the height distribution has

low frequency trends the roughness of the surface is super-

imposed on these trends. If the mean value is now calculated

for the height distribution and this value is used over the whole

surface, then the deviations from this plane are larger than those

introduced by roughness alone, and the weak low frequency effects

increase the deviations, giving a larger root-mean-square height

than that attributed to roughness alone. These trends, although

weak, effectively give an overestimate of the surface roughness.

To reduce this problem areas over the rough surface approxi-

mately 10 cm x 16 cm were investigated using the section height

profile measurements. This method is analogous to the acoustic

sampling, as the insonified areas were approximately of the

same dimensions. The mean plane was calculated for the area, and

this local value represented a zero plane over which the

deviations from the plane are introduced by roughness, and not

roughness superimposed on surface trends about a zero plane for
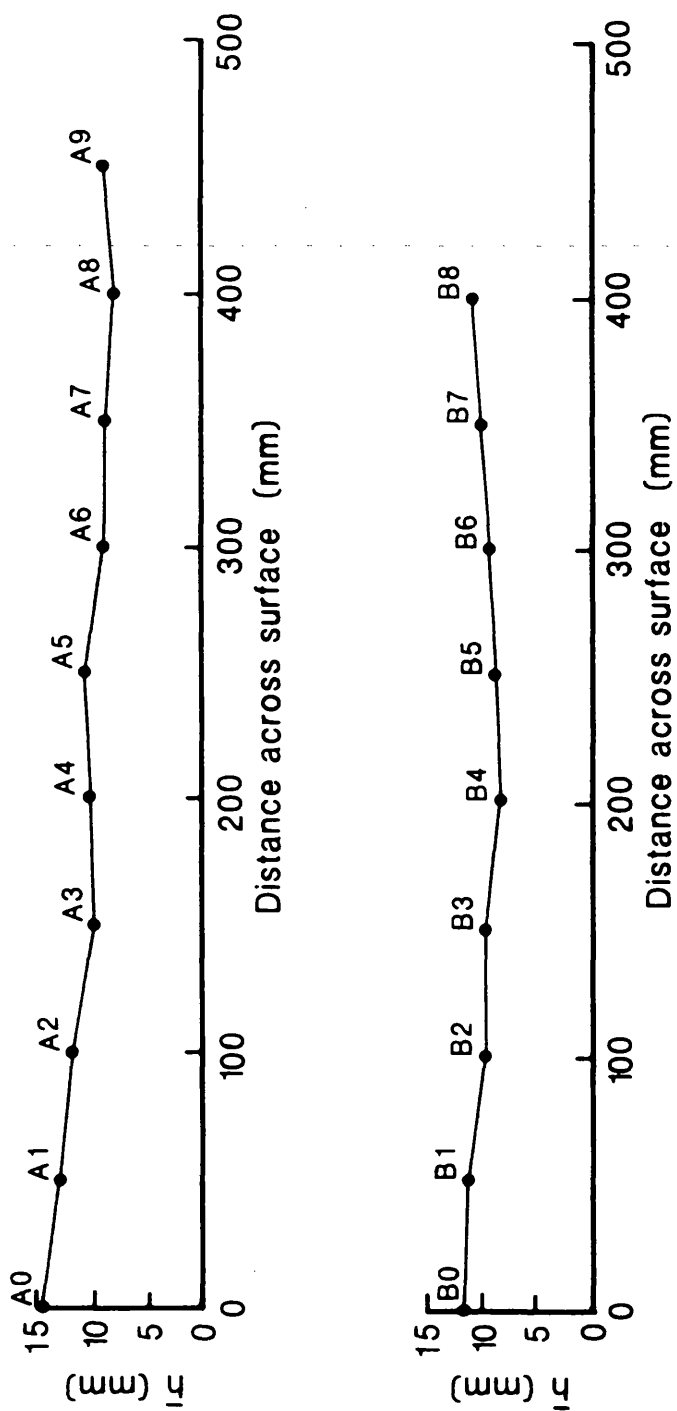
Fig 5   The mean height variation of the section profiles.

the whole surface. The root-mean-square height 'h', calculated

for the surface using this method reduces the low frequency effects

and is given by

$$h = [\sum_{i=1}^{N} \sigma i^2/_N]^{\frac{1}{2}} \qquad\qquad 3\text{-}12$$

Where σ^2_i are the variances of the height distribution in the areas.
The t-test therefore indicated problems with the surface which

resulted in using local areas to calculate the root-mean-square

height for the rough surface.

3.4.6 Variation in the standard deviations

An analysis can be made of the standard deviations to see

if they are consistent with a Gaussian distribution. One test

which can be used is the F test given by

$$F = (\frac{S_1}{S_2})^2 \qquad\qquad 3\text{-}13$$

Where S_1 and S_2 are the standard deviations of the area samples. The

standard deviations used were obtained by dividing each profile

into three equal lengths, and combining the same sample sections

on three adjacent profiles. Each area then contained the same

number of sample points as a section. Calculations were made on

each of these areas for the two sets of profiles measured at

right-angles to one another. The standard deviation for these

areas are shown in table 2. If the largest and smallest standard

deviations are used, and found not to differ significantly from one

another then it follows that there will be no significant difference

between any pairs. Using these gave

$$F_A = 3.54 \qquad\qquad F_B = 3.29$$

The number of degrees of freedom is $V = n - 1$, when 'n' is the

number of independent points in each area. This is the same as

the number of independent points in a section, ie fourteen. At

the two percent significance level, the hypothesis that within

each group, A and B, the standard deviation came from the same

Gaussian population cannot be rejected. Pooling the standard

deviations of the two groups yields the same results. At the

5% significance level the null hypothesis cannot be rejected

for eight of the nine area standard deviations in each group.

The same is true for fifteen of the combined eighteen standard

deviations.

Another test that can be applied which uses all the standard

deviations simultaneously is known as Bartletts Test. This is a

special application of the X^2 test and is given by Kennedy and Neville

(35) as

$$\chi^2 = 2.3026 \ (n-1) \ [K \log \bar{s}^2 - \sum_{i=1}^{K} \log s^2_i] \qquad\qquad 3-14$$

Table 2

Standard deviations of the area sampling over the surface

A0-A9 Sections

2.02 mm	2.31	2.56
2.27	1.71	2.84
1.51	2.25	2.15

B0-B8 Sections

2.45	2.94	1.75
1.88	2.27	2.05
2.18	2.04	1.62

where n is the number of independent points in each area, s_i is the estimate of the area standard deviation, $\overline{s^2}$ is the mean estimate of the square of the standard deviation, and K is the number of areas used in the test. Using table 2 gives

$$\chi^2_A = 7.289 \qquad\qquad \chi^2_B = 6.992$$

The number of degrees of freedom are k-1=8. For each of the values of χ^2 the standard deviations do not significantly differ from one another at the 50% significance level, and this is also the case for the pooled standard deviation. This is strong evidence that the standard deviations are homogeneous, and the surface roughness, with the effects of the low frequency trends reduced, isotropic.

Calculating the root-mean-square height 'h' of the surface by taking the root-mean-square value of the area standard deviations as in equation 3-12, yields the same value using either groups A or B or pooling the area standard deviation. The magnitude is

$$h = 2.2 \pm 0.1 \text{ mm}$$

which is a value consistent with the design requirements.

3.4.7 Variation in the autocorrelation lengths

The variance in the value of a particular lag position in the autocorrelation function can be estimated using Schwartz and Shaw (36).

$$\text{Var } C_N(L) = \frac{2}{N} \sum_{r=0}^{N-1-L} [1-((L+r)/N)][C^2[r]+C[r+L].C[r-L]] \qquad 3-15$$

where C[r] is the true autocorrelation function, N is all the

points in a sample, and L is the lag position. The lag position

chosen was the mean autocorrelation length of the sample profiles,

and the true autocorrelation function used was Gaussian.

$$C(r) = \exp[-(r^2/T^2)] \qquad\qquad 3-16$$

where T is the autocorrelation length. Since T = 19 mm, and the

sample points in a profile are 2 mm apart, then L = 10, and N = 240.

Using these values for L and N in equation 3-15 gives

$$\text{Var}\ \ C(T) = 0.06$$

$$\text{S.D.}\ \ C(T) = 0.245$$

The value of 0.245 is an estimate of the standard deviation of the

autocorrelation function at a lag equal to the autocorrelation

length, for a Gaussian process with a Gaussian autocorrelation

function. This spread in values can be used directly to derive the

expected spread in autocorrelation lengths when sampling such a pop-

ulation. The value of C(r) at T is (1/e)and therefore at this lag position

$$\exp[-(T^2/t^2)] = 0.368 \pm 0.245$$

This gives a lower value for t of 13 mm and an upper value of

27 mm. Therefore, if the autocorrelation lengths measured came

from a Gaussian surface with a Gaussian autocorrelation function,

then the measured values should lie within the range 13-27 mm.

As can be seen in table 1, the measured values do fall within this

interval, and therefore the spread in measured autocorrelation

lengths is not significantly different from that which would be

expected from a surface with Gaussian features. The root-mean-square

correlation length and its standard error are

$$T = 19 \pm 2 \text{ mm}$$

The autocorrelation length combines with the root-mean-square

height to give a root mean square surface slope, S_ℓ given by

$$S_\ell = \frac{\sqrt{2} \, h}{T} \qquad\qquad 3\text{-}17$$

The value of which is 0.16 and this was compatible with the

design requirements.

3.5 Summary

In the analysis of the surface statistics an important

parameter required to carry out some statistical tests, is the

number of uncorrelated data points. The technique used to obtain

this value was the relationsip between the standard deviation of

a correlated and uncorrelated population. Using this value,
tests were carried out. These tests cannot prove that the samples
came from a Gaussian height distribution, but they are used to show
that the samples cannot be rejected as coming from such a popula-
tion at a particular significance level. The usual criterion is
the 1% or 5% significance level, which states that there is a
one in a hundred or one in twenty chance respectively, of
obtaining the sample values measured from a Gaussian population.
If the measured values are found to be less likely to occur, then
the null hypothesis may be rejected for that test.

If the χ^2 test is used at the 5% significance level, the
heights sampled cannot be refuted as coming from a Gaussian
distribution. This is an indication that the surface probably
has an overall height profile which is close to Gaussian. The
t-test showed up some low frequency trends, and these can be
observed in figure 5. Because the low frequency effects cause the
surface roughness to be overestimated if no account is taken of
them, the surface was divided into areas, and these areas
were investigated. The F-test showed that all the area standard
deviations were homogeneous at the 2% level, and nearly all of
them at the 5% level. The Bartletts Test, which used all the
standard deviations concurrently, showed that roughness measured
over the areas was strongly homogeneous. Also, the Gaussian
autocorrelation function fitted to the experimental data, gave
a spread in autocorrelation lengths consistent with that expected
from a Gaussian surface.

The surface had a high reflection coefficient with a structure which dissipated the acoustic energy propagating into the material. Also the rough surface boundary had statistics which approximate to those of a Gaussian surface, and thereby allowed the analysis for the scattered intensity derived in the previous chapter to be applied in this case. The sculptured rough surface therefore had the main specifications for carrying out the investigation.

Chapter 4   Design And Construction Of The Equipment

4.1   Tank And Gantry System

In previous chapters little mention has been made of the hard-
ware used for data collection. In this chapter therefore, a more
detailed explanation is given of the equipment used. All measurements
unless otherwise stated, were taken in a reinforced fibre glass tank
with internal dimensions of 110 x 122 x 245 cm. Quarter inch
aluminium angle was fitted along the top of the longer sides of the
tank. These two lengths of aluminium angle were used as rails and
they formed the base upon which the gantry system for the transducer,
hydrophones and acoustic filter were constructed. The rails were
levelled to run parallel to the water surface, and they were parallel
to one another in this horizontal plane.

Figure 1 shows in a schematic fashion the experimental arrangement
for taking many of the measurements. Figure 1 of Chapter 5 shows a
photograph of the system. Trolley A in figure 1 was constructed to
run on the rails along the tank length. Onto trolley A was added
another trolley, labelled B, which moved at right angles to the
rails on the tank. Mechanical adjustments on trolley B allowed the
transducer to be moved up and down, rotated in a horizontal plane
about the centre of the radiating face, and tilted forwards or
backwards in a vertical plane about a pivot located at the same
height as the tank rails. Simpler constructions allowed the hydro-
phones and acoustic filter to move along the tank rails, move at
right angles to the tank rails, traverse up and down, and rotate

about the vertical axis. These degrees of freedom are illustrated
in figure 1.

Scales were attached to the transducer, hydrophone and
acoustic filter which allowed the position of the acoustic centre
of the first two and centre of gravity of the latter to be known
relative to the water surface and the rails. The arrangement
allowed both freedom of movement for any of the instruments through-
out the water, and their relative positions to be known.

4.2 Transmitter Requirements

For the model rough surface described in the previous chapter,
a narrow beam transmitter operating over the frequency range 20-300 kHz.
was needed to investigate the frequency response of the rough surface.
For this frequency range the normal incidence backscattered intensity
changed from being predominantly coherent through to almost completely
incoherent. A narrow beamwidth was required over the full frequency
range because of the relatively small dimensions of the tank facility
and the limited area of rough surface which had been practicable to
construct.

For a transducer with an approximately Gaussian beam profile the
e^{-1} point needed to be a few surface correlation lengths long for the
insonified area to contain a region of surface roughness, yet it was
also required to be less than approximately 10 cm so that a number of
independent intensity measurements could be obtained over the surface.
This constraint on beamwidth was required for a range of distances
of between 30 and 100 cm from the transducer over the broad frequency
band in order to conduct the scattering measurements.
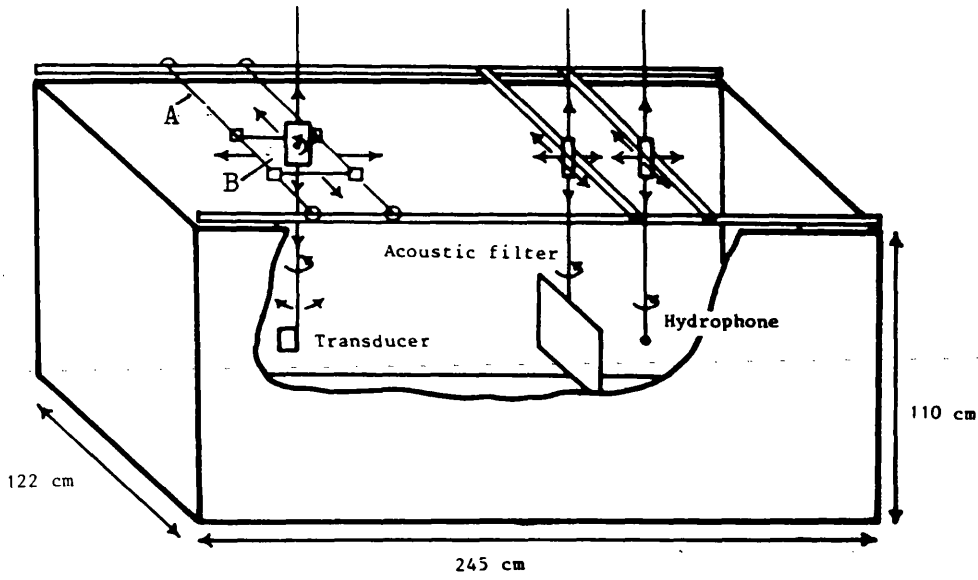
Fig 1   Tank arrangement with the degrees of movement shown.
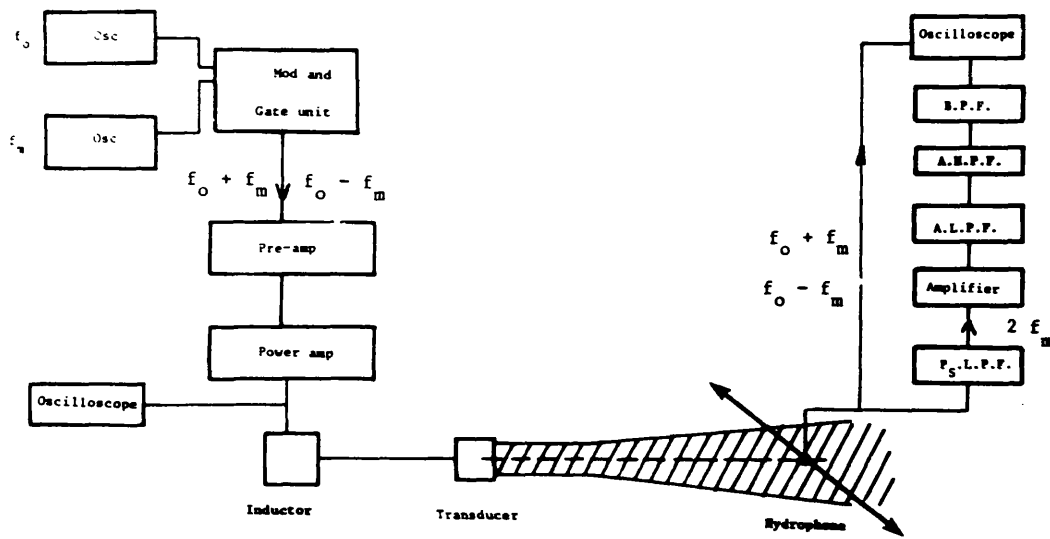
Fig 2   Block diagram of the equipment used. //////
Interaction zone.   Diagram nomenclature, A-Active, L-Low, H-High,
B-Band, P-Pass, F-Filter, P_s-Passive

To construct a transducer with these design features would not have been practical using conventional acoustic techniques. Even the construction of a number of transducers would still have presented problems, for example in the low kilohertz region the transducer would have become prohibitively large to obtain the required beamwidth. An alternative was to utilise the unique properties of the parametric or acoustic endfire array. This made available an acoustic source that had transmitter characteristics compatible with the requirements. Details of an experimental investigation into the parametric array are given in Appendix 4 and only those results of immediate interest to the scattering problem are presented in this chapter.

In brief, two high frequency primary waves of finite amplitude and slightly different frequencies were launched simultaneously from a small transducer which was resonant and highly directional at the primary frequencies. Because the propagation of these waves was not completely linear intermodulation occurred, one component of which was the difference frequency. A source density function for this interaction was derived by Westervelt (37) and integration over these secondary sources yields the difference frequency field. Using conventional acoustics it was relatively simple to obtain the high frequency narrow primary beams, which were used to generate a highly directional difference frequency that could be operated over a wide range of frequencies with low quality factors at each of these frequencies.

4.3   Transmitting Instrumentation

A block diagram of the equipment used is given in figure 2. In this chapter the function and response of the equipment used is considered.   Details of the electronic circuitry designed and built are given in Appendix 3.

4.3.1   Modulating and gating unit

This unit was used to obtain the pulsed primary frequencies from two continuous wave oscillators.   Into one input of the modulator and gating unit was delivered a modulating frequency f_m at half the required difference frequency.   Using digital circuitry a rectangular pulse of variable length and repetition frequency was derived from this input.   The edges of the rectangular pulse were phase locked with the zero-crossover points on the modulating frequency.   The rectangular pulse was used to gate the modulating frequency, giving a quasi-monochromatic pulse, starting and terminating at   zero-crossover points on the waveform.

This pulsed continuous wave modulating signal was then used to modulate a carrier frequency, which in the difference frequency experiments was the primary centre frequency, f_o.   From this signal a double-side-band suppressed carrier was obtained with a spectrum concentrated at $f_1 = f_o + f_m$ and $f_2 = f_o - f_m$.   The difference frequency was given by $f_1 - f_2$ which was equal to $2 f_m$.   The difference frequency was simply changed by retaining f_o at the resonance frequency of the transducer, and varying the modulation frequency.   The unit also had a facility to output only the gated

modulating frequency which could be varied from 1 kHz-1.5 MHz. This option was used when carrying out primary frequency beam plots, and for other experiments where a single frequency pulse was required. The rectangular digital pulse was also output for triggering purposes. Figure 3 shows the input and output signals.

4.3.2 Amplifying section

The output from the modulating and gating unit was fed into a pre-amplifier. The gain of the pre-amplifier is shown in figure 4 for a constant voltage input of 100 mV. A gain of over 20 db was obtained over the frequency range of interest. The output from the pre-amplifier was fed into a Marconi power amplifier which had a fixed gain of 50 db for the primary frequencies used. The output impedance of the power amplifier was 50 Ω to which the transducer was well matched. The maximum output voltage across the transducer was limited by a cut out overload in the power amplifier to 40 V pk for the combined primaries.

4.3.3 The transducer

A simple air-backed transducer was constructed to operate at the primary frequencies. The design of the transducer is shown in figure 5. The size and resonance frequency of the transducer had to be selected so as to achieve a reasonable signal level and directivity at the difference frequencies in the range 20-300 kHz.

A lower limit for the primary frequencies was set by the practicality of reducing the level of the received primaries by filtering to values negligible in comparison with the difference

Input carrier frequency

Input modulating frequency

Modulated carrier

Output modulated signal

Output modulating signal

Output digital signal
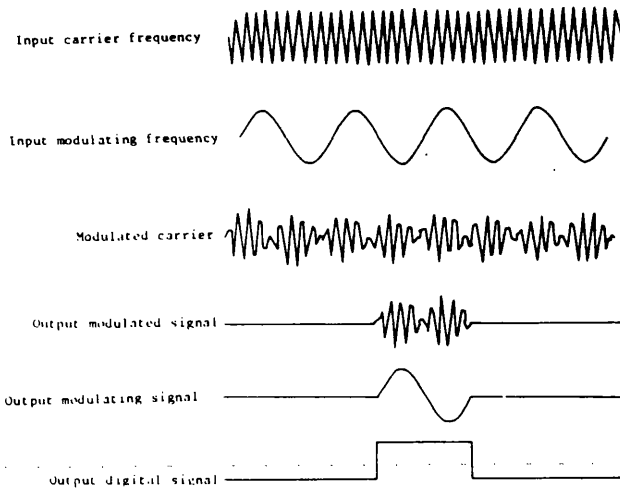
Fig 3   Waveforms generated by the modulating and gating unit.
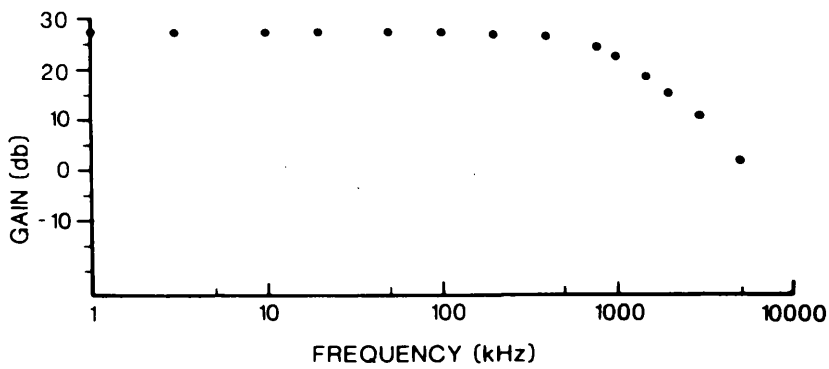
Fig 4   Gain of the transmitting preamplifier.
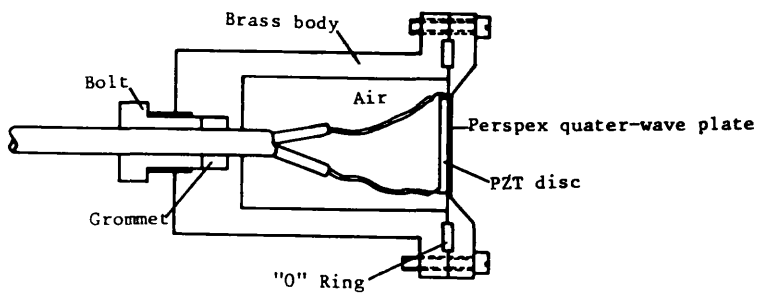
Fig 5   Transducer design. Scale ≈ 0.35

frequency signal received. The attenuation of an acoustic filter used is shown in figure 14b, and this imposed a similar lower limit for effective truncation of the primaries. The production of the transmitting electronics, which initially involved the building of a power amplifier, would have been difficult to design and construct for operation much above a few megahertz. Therefore an upper limit was also in effect. A one megahertz resonant transducer was chosen because this offered the possibility of obtaining the required range of difference frequencies and of overcoming the practical difficulties mentioned.

A single 2.5 cm diameter disc was chosen because this had calculated primary beamwidths of less than $4°$, and a Rayleigh distance of 30 cm, both of which were suitable for obtaining the directivity required at the difference frequencies. Also a single radiating element allowed a lightweight simple transducer to be constructed which took full advantage of the parametric array.

The transducer was used over a broad frequency range from 0.85-1.15 MHz to generate difference frequencies up to 300 kHz. Rather than allowing the disc to radiate directly into the water through an oil window, it was decided to widen the transducer bandwidth by taking advantage of a quarter-wave matching layer as outlined by Kossoff (38). The layer transforms the water loading impedance, Z_w, near resonance to (Z_m^2/Z_w) where Z_m is the impedance of the material from which the matching layer is made. The bandwidth of the half power points of an air backed ceramic transducer is given by Tucker and Gazey (39) as approximately

$$\Delta f_{-3db} \simeq \frac{2}{\pi} \frac{Z_L}{Z_C} f_0 \qquad\qquad 3\text{-}1$$

Where Z_L and Z_C are the load and cermanic element impedences, and f_0 is the resonance frequence of the ceramic. When an air-backed transducer loads directly into water $Z_L = Z_W$ and for the ceramic used this offered about a 3% bandwidth. Using a matching layer transforms Z_L form Z_W to Z_M^2/Z_W near resonance, and thereby increases the bandwidth by $(Z_M/Z_W)^2$. The optimum value for the matching impedence is shown by Koymen, Smith and Gazey (40) to be

$$Z_M = (Z_W^2 Z_C)^{1/3} \qquad\qquad 3\text{-}2$$

This would have increased the bandwidth by about a factor of eight. A convenient material with an impedance close to the optimum value for Z_M was perspex, which has a value of 3.16 rals.

The admittance response of the transducer in water is compared with predicted values calculated using reference (38) for a lossless transducer in figure 6a. Figure 6b shows the response with the static capacitance tuned out. At resonance the input impedance was 47Ω and a bandwidth of 185 kHz was obtained. Self reciprocity measurements gave an estimated efficiency of 70%.

In Appendix 4 primary frequency beam plots are given in cartesian form which show the response over a small range of angles for a number of frequencies; to show that the transducer was well behaved at larger angles off axis, a polar plot is shown in figure 7a. An axial pressure response is also shown in figure 7b.
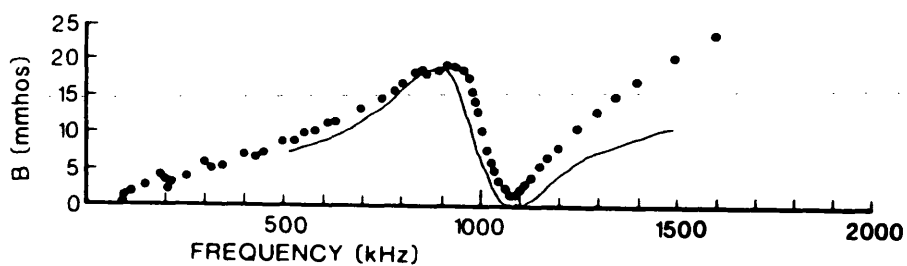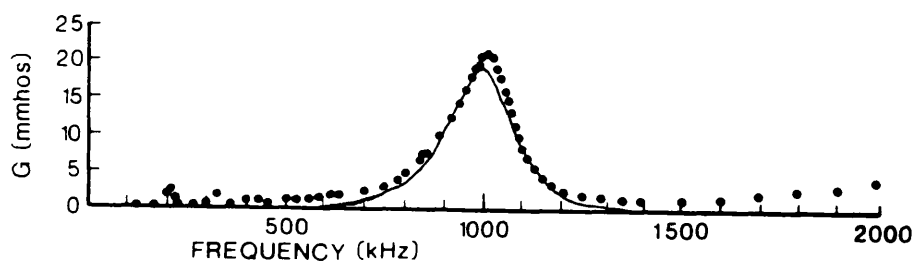
Fig 6a Conductance and susceptance of the transducer.
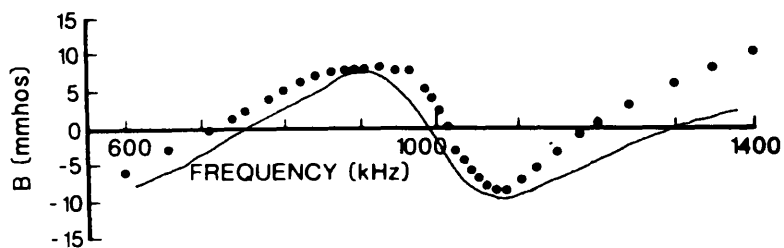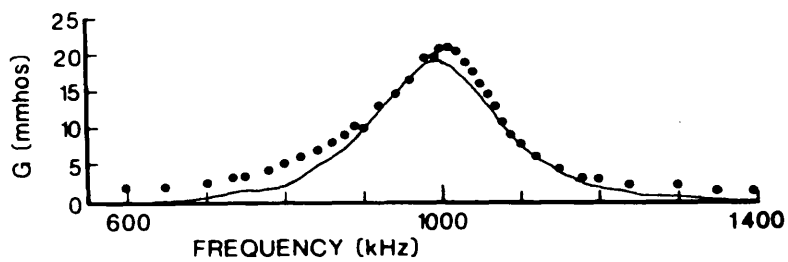
Fig 6b Conductance and susceptance of the transducer with the static capacitance tuned out.
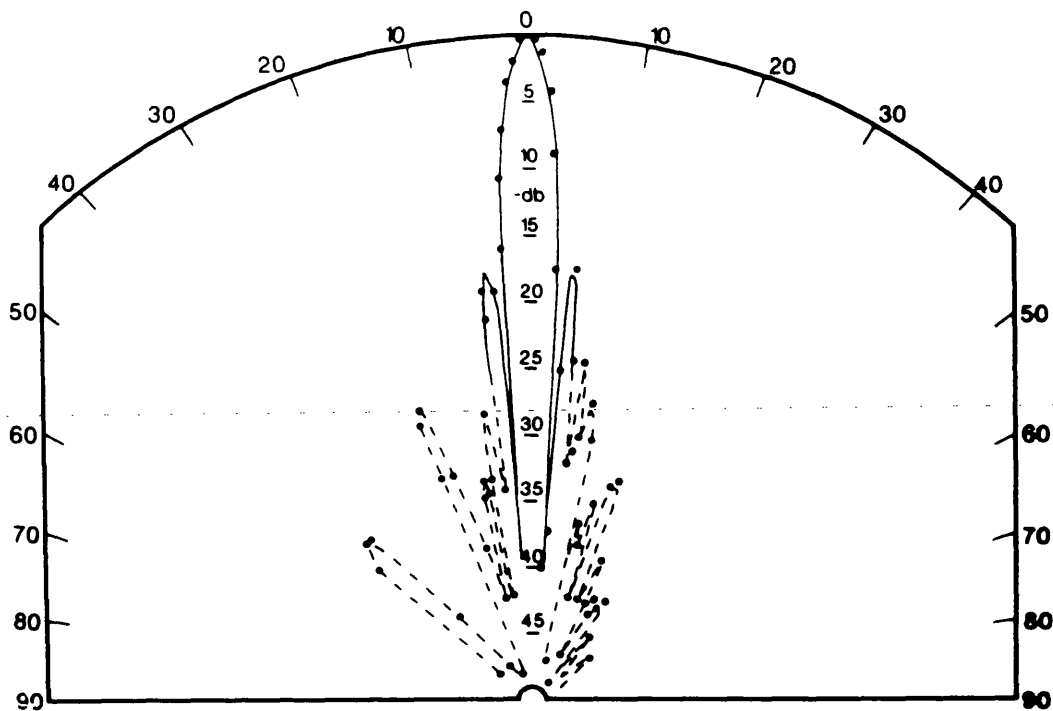
Fig 7a   Polar beamplot of the transducer at 1 MHz. ——
Calculated using $2J_1(x)/x$ where $x = kaSin\theta$ and a is the
transducer radius.

RANGE, r (cm)
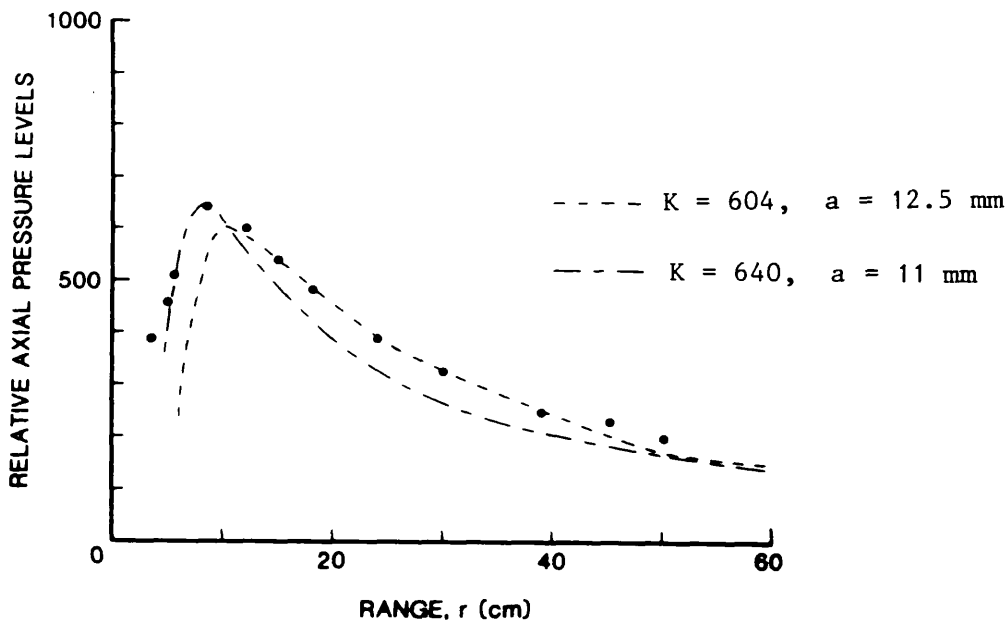
Fig 7b   Axial pressure level versus range near the transducer.
Two curves are calculated using the expression for the axial
pressure level of a piston radiator, $p = KSin^2[(k/2)([r^2 + a^2]^{\frac{1}{2}} - r)]$
where a is the piston radius and K a constant emperically chosen
to fit the data.

4.3.4 Linearity of the transmitting system

Before the difference frequency measurements were taken, the non-linearity of both the transmitting and receiving systems were measured. For the transmitting measurements the magnitude of the difference frequency pressure level over the range of frequencies used, was measured at one metre, with and without the acoustic filter placed almost flush against the transducer face. With the filter close up to the transducer, the primaries suffered approximately -20 db of attenuation immediately after transmission, and therefore there was only a very low intensity parametric array in the water. If there had been any significant directly radiated difference frequency, this could then have been observed. However, on-axis measurements showed a -30 db reduction in signal level, with the acoustic filter in place, relative to when it was removed. The direct radiation at the difference frequency for this range was therefore at least -30 db below that generated by the parametric array. When using another acoustic filter with a measured attenuation of 0.14 db kHz^{-1}, giving an estimated -140 db of attenuation at one megahertz only electrical noise was detected by the hydrophone when the acoustic filter was placed flush against the transducer. There was no evidence for significant levels of direct radiation at the difference frequencies used.

4.4 The Receiving System

4.4.1 Hydrophones

At the front end of the receiving system two hydrophones were employed, a Bruĕl and Kjaer 8103 and a Celesco LC5-2. The frequency

response of the Bruël and Kjaer 8103 is shown in figure 8, where

the solid line up to 200 kHz is the manufacturer's specification;

and beyond this frequency reciprocity was used to obtain the

nominal response up to one megahertz. This hydrophone was used for

all difference frequency measurements and some of the primary

frequency measurements. The horizontal directivity was quoted as

typically within ± 2 db at 200 kHz. Owing to the variation in

response for the horizontal plane, the hydrophone was always

orientated in the same direction when any comparative measurements

were being taken. Particular care was taken when comparing the

scattered intensities with reflected intensities from the plane

surface for normalisation. The Celesco LC5-2 was used to monitor

some of the primary frequency beam plots. The frequency response

of the LC5-2 is shown in figure 9 where it can be seen to be about

-15 db less sensitive than the 8103, over much of the difference

frequency range.

4.4.2 Filtering and amplifying

For the difference frequency measurements the output from the

hydrophone was fed into a low-pass passive filter. The response

of the filter for a source impedance of 1 KΩ and a terminating

impedance of the same value is shown in figure 10. Circuit details

of the constructed receiving electronics are given in Appendix 3.

The attenuation of the primaries by the filter was -80 db, and this

was sufficient to reduce them to negligible levels in comparison

with the observed difference frequency signals. Following on from

the passive filter was a linear Brookdeal amplifier which had a

variable gain setting between 20-100 db with 1 db intervals.
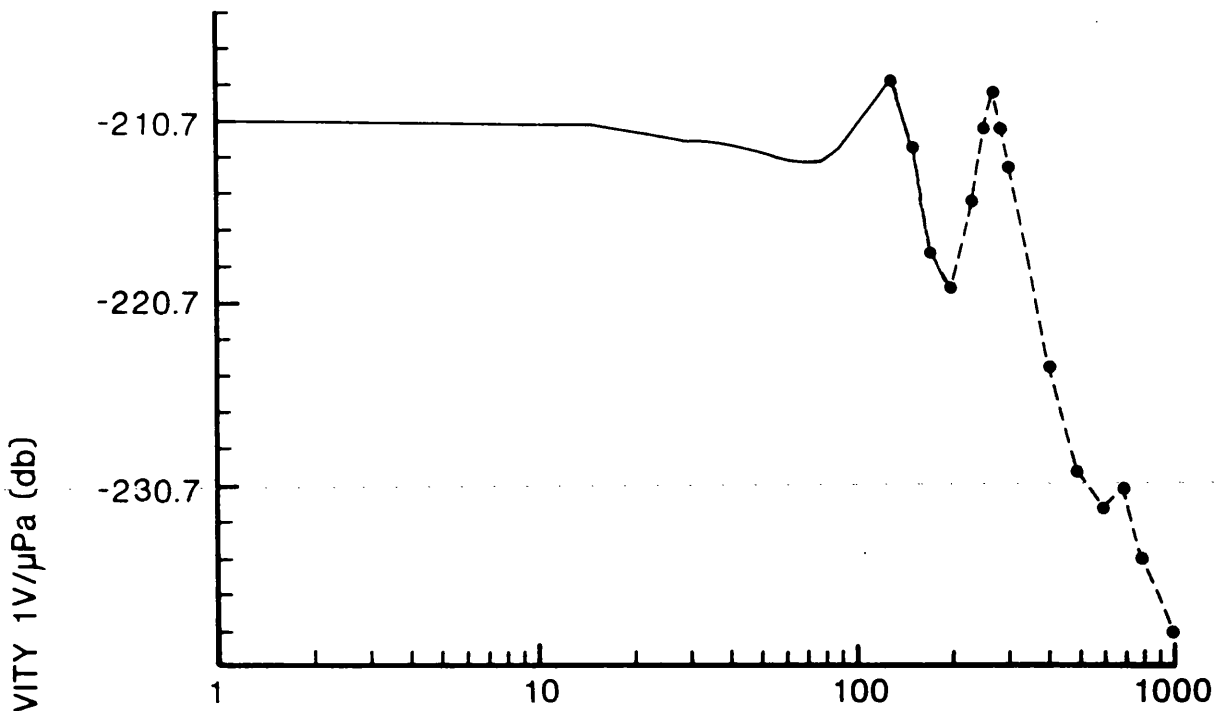
Fig 8   The response of the Bruёl and Kjaer 8103 hydrophone.

FREQUENCY (kHz)

Fig 9   The response of the Celesco LC5-2 hydrophone.

The electrical noise of the receiving amplifier was the limiting

detection threshold of the system. At a gain of 20 db the noise

level was measured as about 100 μVp-pdb^{-1} reducing to around

10 μVp-pdb^{-1} for gains of 60 db and above. This noise level

limited the minimum difference frequency scattering measurements

to 20 kHz. After the Brookdeal amplifier came two active filters,

a low-pass filter to reduce the high frequency noise of the amplifier,

and a high-pass filter to remove 50 Hz mains. The response of

these filters are shown in figures 11 and 12. Together the

receiving system acted as a variable gain band pass filter with a

flat response between 20-200 kHz. The frequency response of

different elements coupled together driven by an oscillator or

the hydrophone itself is shown in figure 13. When needed, a

Kronhite filter followed the high-pass active filter, to give a

much sharper frequency response about a particular frequency of

interest.

4.4.3 Linearity of the receiving system

By summing the output from two oscillators linearly, using

simple resistors and feeding the signal into the passive low-pass

filter, measurements were made on the linearity of the passive

filter. The two signals summed were at primary frequencies and

input voltage levels similar to those received on the hydrophone when

making measurements on the parametric array. Measurements of the out-

put could only detect the input high frequency signals attenuated by

-80 db and on passing this signal through another low-pass filter,
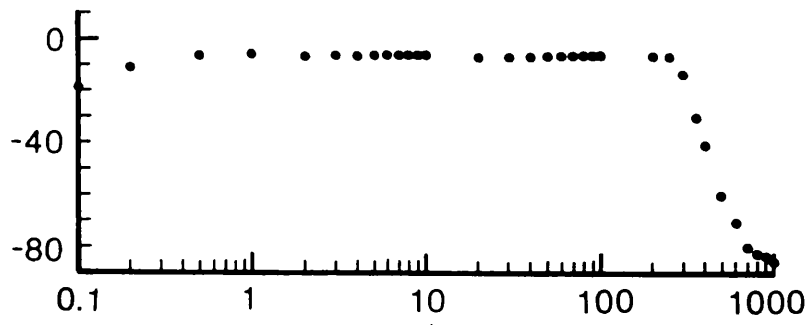
Fig 10   Response of the low pass passive filter.
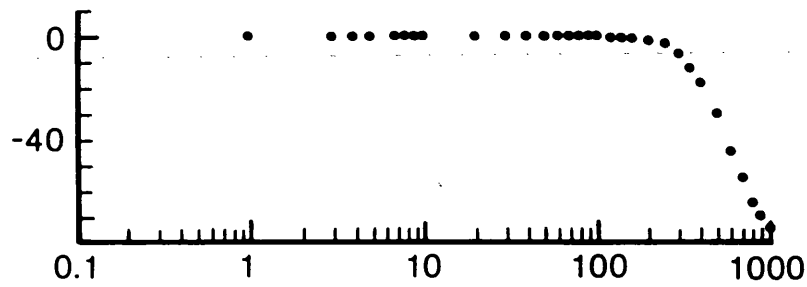
Fig 11   Response of low pass active filter.
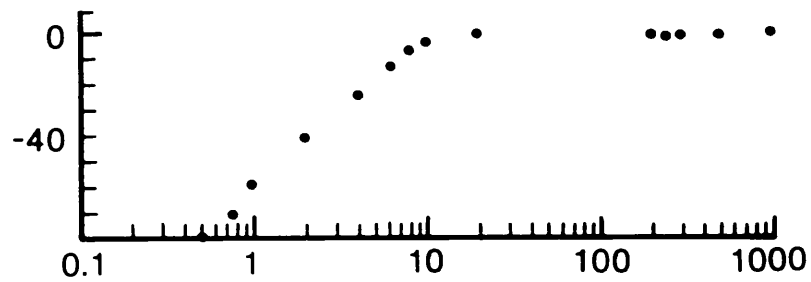
Fig 12   Response of high pass active filter.

FREQUENCY (kHz)
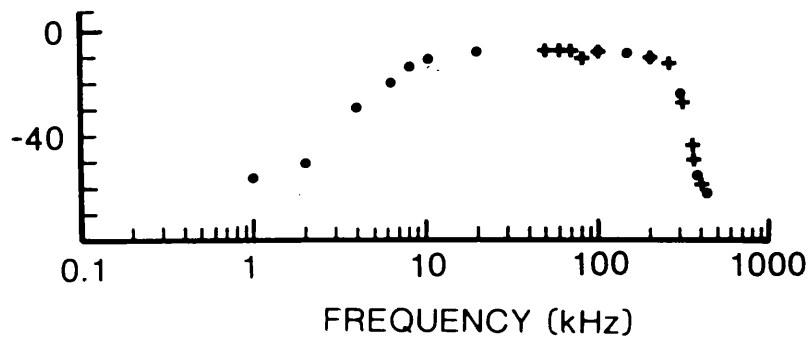
Fig 13   Response of the filters and Brookdeal amplifier coupled together when driven by an oscillator ●, and the Bruёl and Kjaer hydrophone +.

ATTENUATION (db)

only electrical noise was observed. Since no non-linearity could be detected in the passive filter and it reduced the carrier levels by -80 db; while measurements on the Brookdeal amplifier and active filters showed non-linearities of the order of -50 db down on the input, there was no significant difference frequency generated in the receiving electronics.

Another opportunity for non-linearity to arise was the hydrophone itself undergoing non-linear deformation by the primary pressure levels. This problem was investigated by Humphrey and Hsu (41). It shows itself by an overlaying of the primary beam pattern with its sidelobes upon the difference frequency beam pattern, and by a change in the slope of the difference frequency beam profile, which gives a "peaky" directivity near the axis. The "peakiness" is due to the primary frequencies major lobes generating difference frequency at the hydrophone element itself. Since the majority of beam profiles and scattering measurements were taken behind an acoustic filter which reduced the primary levels by -20 db, the problem of this type of hydrophone non-linearity was removed. For the beam profiles shown in figure 4, Appendix 4, no acoustic filter was used. Out of the beam profiles the one which might have been expected to display the hydrophone non-linearity to the greatest effect was the 10 kHz profile. However, when the 1 MHz primary beam profile was overlaid upon the 10 kHz difference frequency beam plot, there was no correspondence in profiles to suggest that hydrophone non-linearity was affecting the difference frequency beam patterns.

4.5   The Acoustic Filter

There was the possibility in the rough surface scattering experiment, that the difference frequencies generated by the primary waves scattered from the rough surface, could by interference affect the intensity of the difference frequencies scattered from the rough surface.   To remove the uncertainty involved in this process, the primary field was prematurely truncated before the rough surface, using a low-pass filter with dimensions of 30 x 30 x 0.7 cm.   The filter transmitted the difference frequencies, but attenuated the primaries by approximately -20 db.

The acoustic filter was a cork loaded butyl rubber sheet. The density of the material was measured and found to be 980 kgm^{-3} and the velocity of sound was observed to be 1700 ms^{-1}.   This gave the material an impedence value of the 1.67 rals making it very close to that of water.   The intensity reflected from the filter was measured relative to a plane expanded polystyrene surface. The relative intensity was found to be frequency dependent and was at least -15 db down on the level reflected from the expanded polystyrene.   The measured values are shown in figure 14a and compared with values predicted from a finite thickness plate of the same impedence calculated from equation 3-3 given by

$$R = (\frac{R_2}{R_1} - \frac{R_1}{R_2}) \; [\, 4 \, Cot^2 k_2 d \, + (\frac{R_2}{R_1} + \frac{R_1}{R_2})^2 \;]^{-\frac{1}{2}} \qquad\qquad 3-3$$

which was taken from Wood (42). R_1 and R_2 are the acoustic impedences of the water and filter respectively, k_2 is the wave number of the
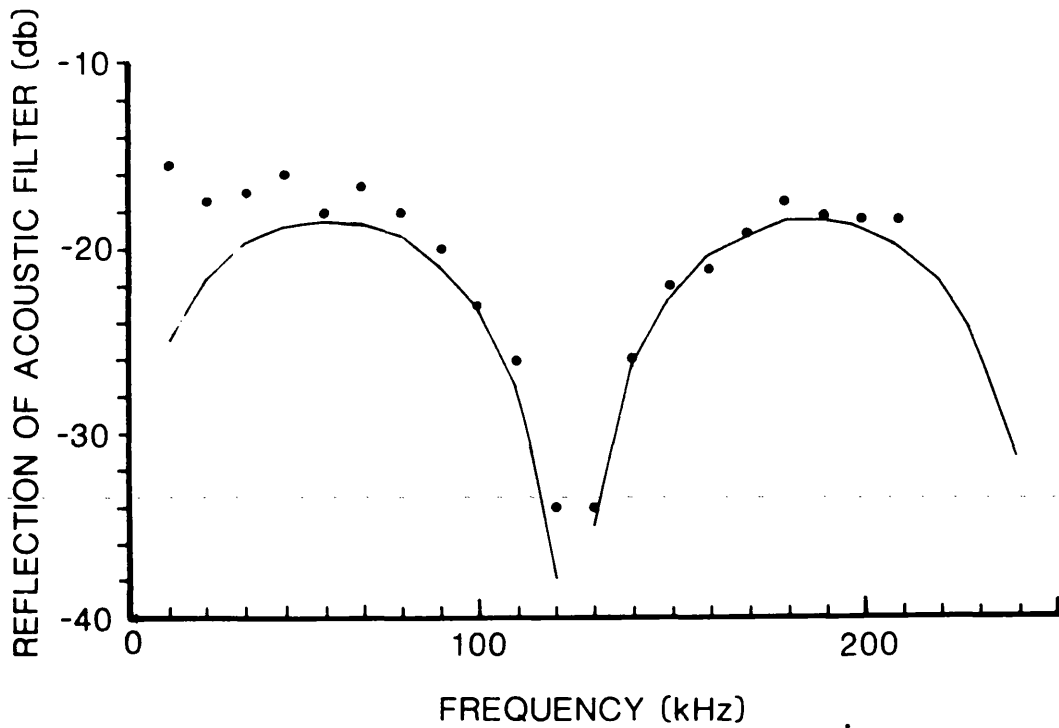
Fig 14a   Reflection of the acoustic filter relative to a plane

expanded polystyrene surface.
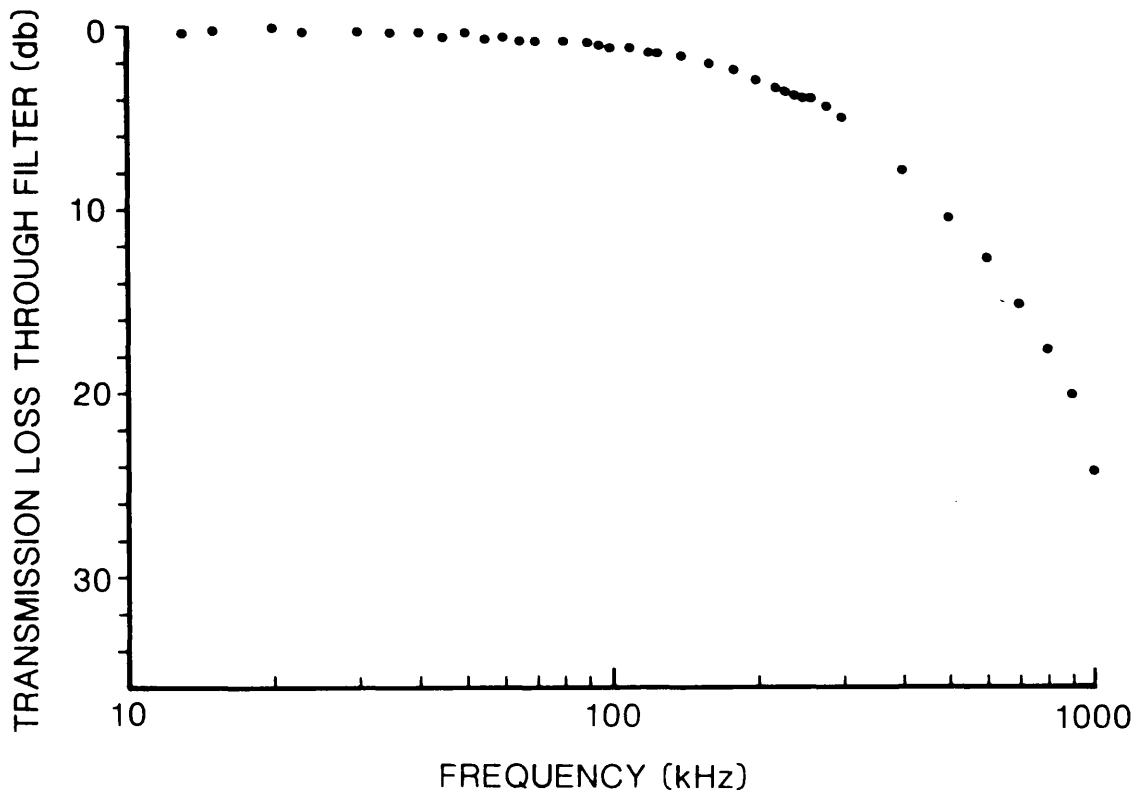
Fig 14b   One way transmission loss through the acoustic filter.

sound in the filter, and d is the thickness of the filter.

The attenuation through the filter was measured over the frequency range 14 to 1200 kHz. The frequencies between 14 and 300 kHz were measured using the difference frequency signals. This was done by truncating the primaries with another similar acoustic filter before they reached the filter under investigation. This avoided difficulties which might have been introduced by terminating the parametric array with the filter whose response was to be measured. The attenuation of the filter being measured was obtained by observing the on-axis difference frequency signal levels with and without this acoustic filter in front of a hydrophone placed on the acoustic axis. Above 300 kHz measurements were made by removing the truncating filter, and radiating single frequency continuous wave gated signals directly from the transducer. Figure 14b shows the one way signal loss through the acoustic filter due to atten-uation measured relative to no filter being present. There was sufficient attenuation at the primaries to efficiently truncate the parametric array.

4.6   Characteristics Of The Parametric Array

4.6.1   Beam profiles

Two sets of rough surface experiments were carried out, one where the transducer remained at a fixed distance from the surface and the receiving position moved progressively closer to the rough surface, and the other where the transducer and the hydrophone moved together, towards the surface. In both cases near normal incidence backscattering measurements were taken.   In the first

case, the transducer remained at 100 cm from the rough surface and
the hydrophone was placed on the acoustic axis at 70,50,30 and
20 cm from the surface. In the second series of experiments the
hydrophone occupied the same position, but was displaced slightly
off the acoustic axis with the transducer at a fixed 16 cm behind the
hydrophone. For each series of experiments the acoustic filter
was placed on the acoustic axis 10 cm in front of the rough surface.

With the transducer, hydrophone and acoustic filter occupying
identical positions to those described, beam pattern measurements
were made in the horizontal plane containing the acoustic axis at
the position the rough surface occupied in the scattering experiments.
Gaussian directivity functions were compared with the measured values.
A selection of measurements for the transducer fixed at 100 cm and the
hydrophone at 50 cm from the rough surface are shown in figure 15 and
these illustrate the beam profiles observed for identical geometries
to those used in the first series of scattering experiments. The
sidelobe structure at the higher frequencies is due to the presence of
the on-axis hydrophone in front of the transducer. Figure 16 shows
beam profiles for the transducer at 46 cm from the surface and the
hydrophone at 30 cm. No breaking up of the beam pattern was observed
because the receiving hydrophone had been displaced off the acoustic
axis. The Gaussian beam profiles are in reasonable agreement with
the measured values in figure 16 but less so in figure 15 due to the
beam pattern fluctuations. However, in the latter case good agree-
ment is obtained above the -10 db level for these patterns and this
is the region which would have had the major influence on the scattered
intensity.
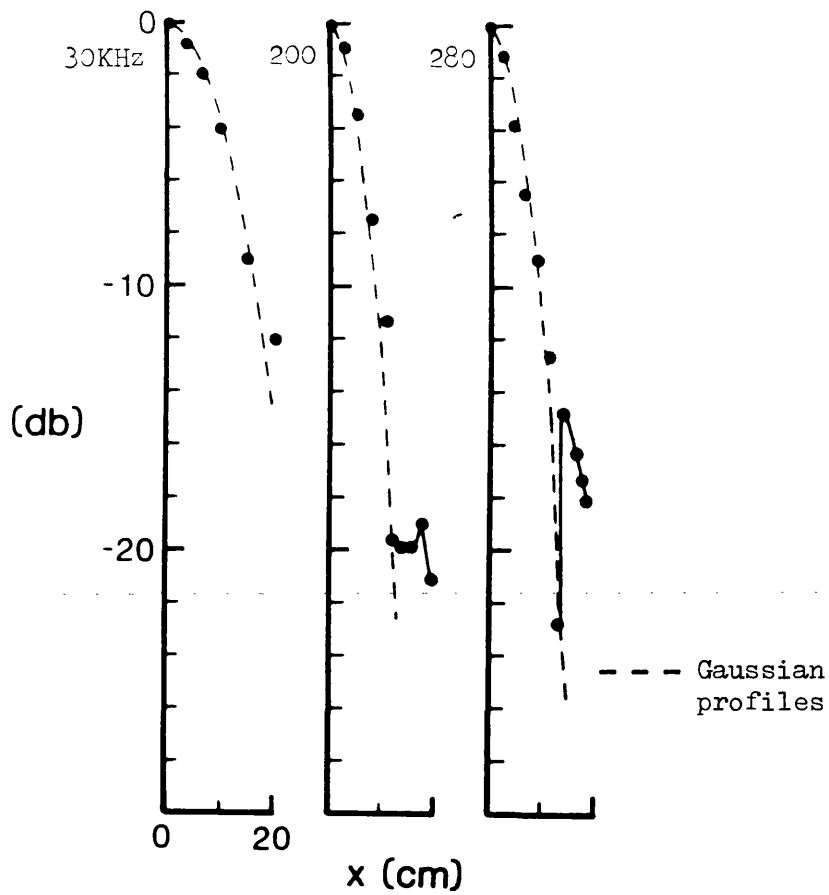
Fig 15   Difference frequency beam profiles.   The transducer-surface separation was 100 cm and the surface-hydrophone distance was 50 cm.
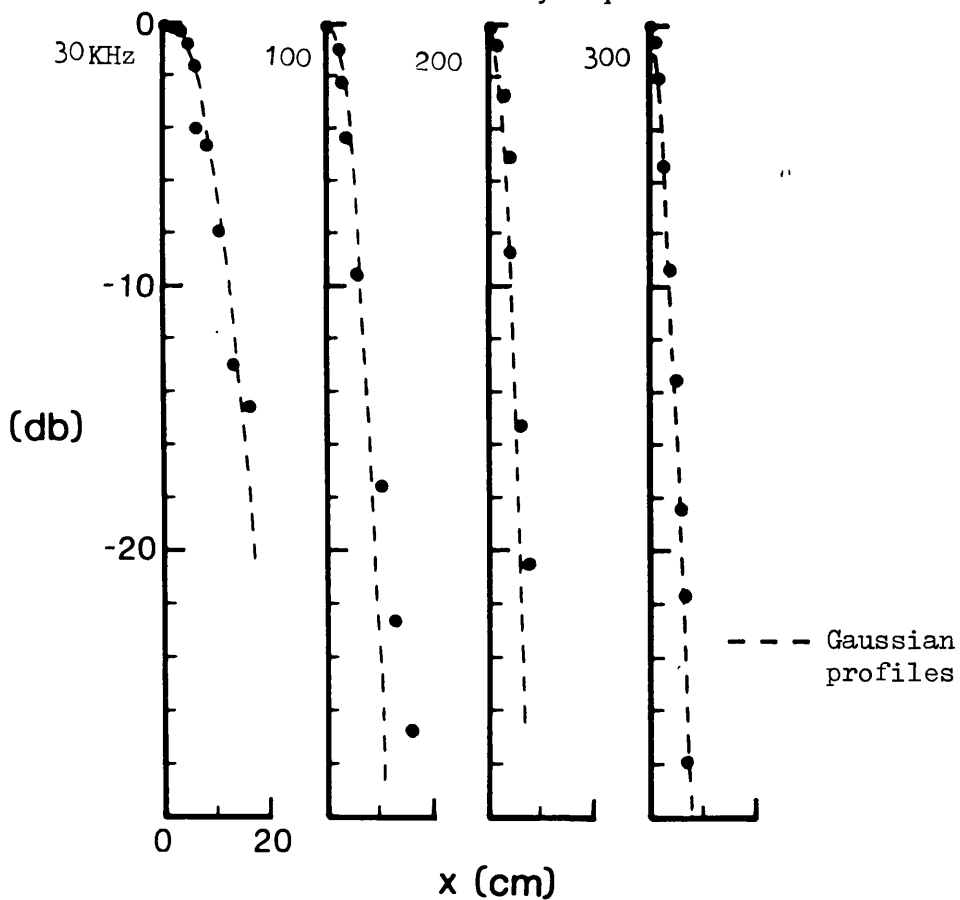
Fig 16   Difference frequency beam profiles.   The transducer-surface separation was 46 cm and the surface-hydrophone distance was 30 cm.
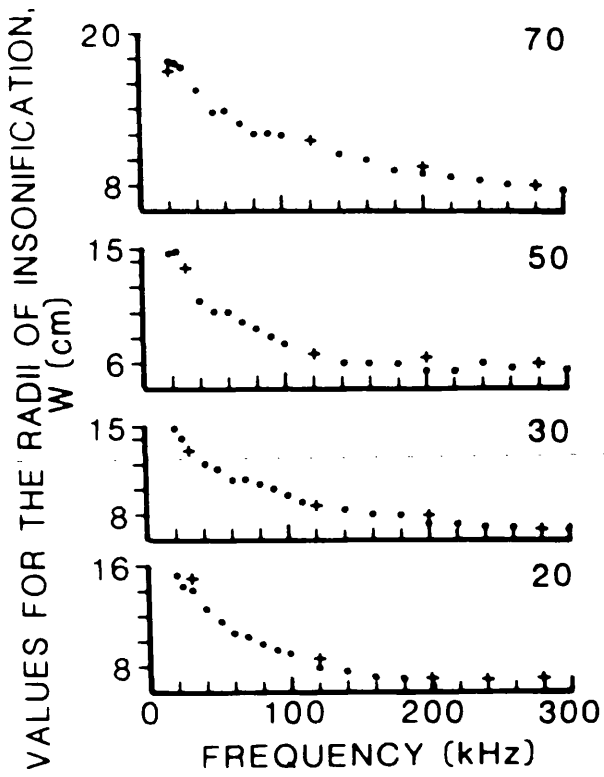
Fig 17
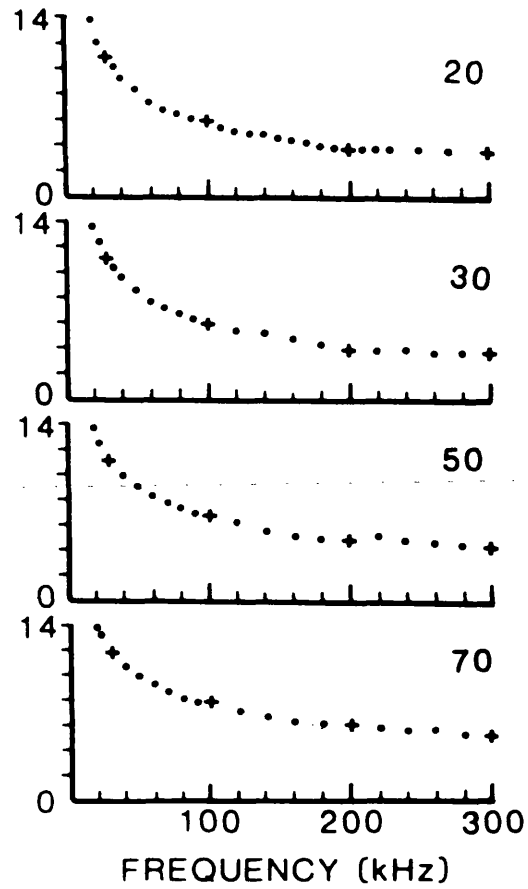
Fig 18

Fig 17   Radii of insonification, W, for the transducer at 100 cm
and the hydrophone 70, 50, 30 and 20 cm from the rough surface.

Fig 18   Radii of insonification, W, for the transducer at 86, 66,
46 and 36 cm, and the hydrophone at 70, 50, 30 and 20 cm
respectively from the surface.

. measured from axis   + taken from a beam profile

The 1/e points on the beam profile for both sets of experiments are shown in figure 17 and 18, these are the values of W used in the equations derived in chapter 2, and are used in the following chapter to predict the scattered intensity.

4.6.2 Axial pressure measurements

It was convenient for this study to treat the axial pressure levels after truncation, as though they were generated from a spherically spreading source located within the primary inter-action zone between the transducer and the acoustic filter. This approach is dealt with in more detail in Appendix 4. Since only the axial pressure relationship with distance needed, was that between the surface at R_o, and that at the receiver position R_1, then by allowing R_o to be a variable, its position could be chosen so that the truncated parametric array appears as a conventional spherically spreading source centred at R_o. Values of R_o are shown in figures 19 and 20.

4.6.3 Phase

In developing the scattering theory presented in chapter 2, the insonified region of the surface was assumed to be illuminated by a source which had a spherically spreading wavefront. However, because the truncated parametric array is a distributed source volume the phase variation of the wavefront near the truncation point does not necessarily have the form of a spherical wavefront. Measurements made by Humphrey (43) using a nominal 1 MHz centre primary frequency, at difference frequencies of 40, 50 and 80 kHz,
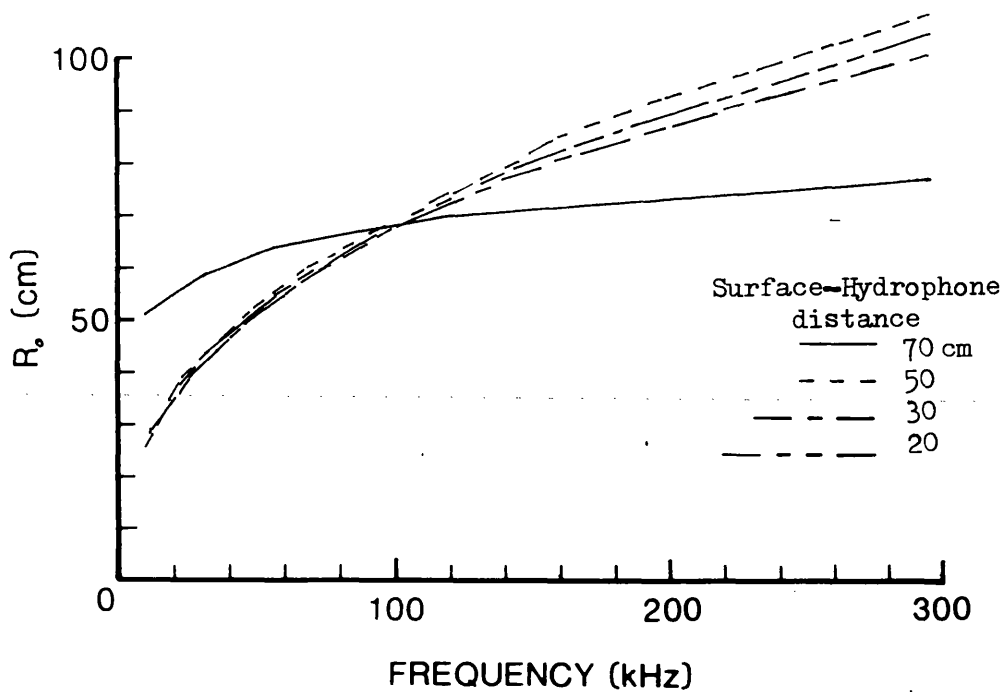
Fig 19   Values for R_0 the amplitude source centre for a fixed transducer distance of 100 cm.
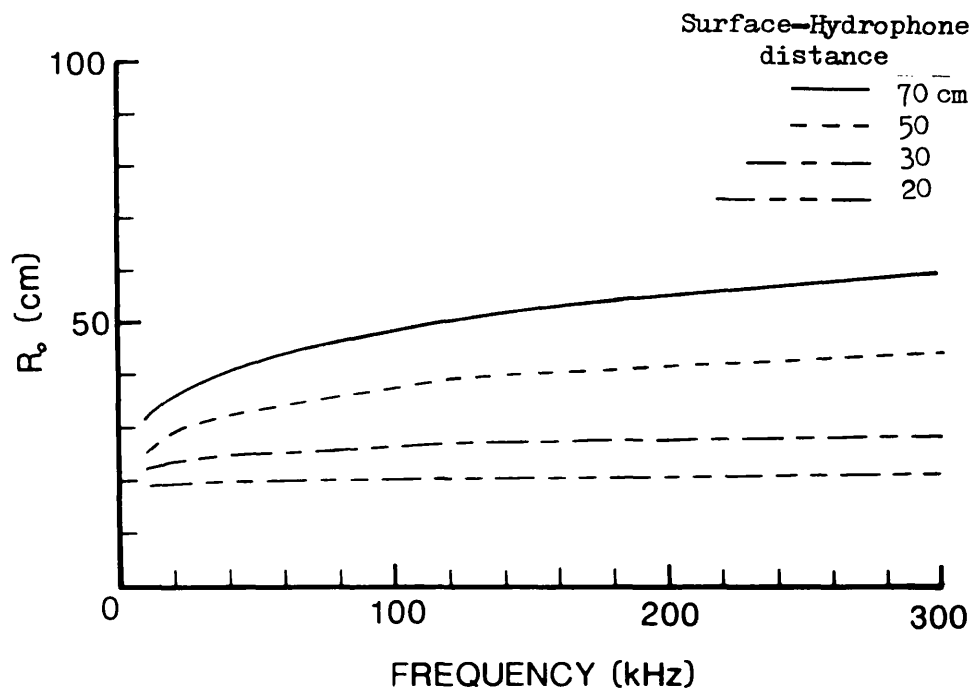
Fig 20   Values for R_0 the amplitude source centre as the transducer moves closer to the surface.

taken beyond the truncation distance, and within 10 cm of the
acoustic filter are shown in figure 21, 22 and 23. These show
that the phase variation is spheroid. Near the acoustic axis,
the phase appears to be derived from a spherical source located
between the primary source and the truncation point. On moving
further off the axis the curvature of the wavefront reduces and
the phase centre recedes from the position of observation. Never-
theless, similarity of the wavefront to that of a spherical
source, and the effects of the beam directivity and surface
roughness reducing the influence of the deviation from sphericity,
made the assumption that the phase was spherically spreading a
reasonable one.

The location of the phase centre was determined by axial
pressure measurements. The decrease in pressure from the point
of truncation followed a 1/R fall off, for the distances used in
this study, as measured from an apparent amplitude source situated
between the primary transducer and the acoustic filter. The
position of the phase and amplitude centres were considered to
be identical. Therefore measurements of the axial pressure levels
were used to locate the phase centre. In the case where the
experimental arrangement in (43) had the same geometry as in the
present work, which is the case for figure 21, the phase and axial
pressure measurements placed the source centres only about 1 cm apart.
However, the calculation of the scattered intensity is not particul-
arly sensitive to the precise location of the phase centre. As long
as it is within 20% of the apparent amplitude source, the estimated
intensity will be bounded by the uncertainty in the theoretical
prediction arising from the standard error in other parameters which
are involved in the calculation, for example T, h, W and R.
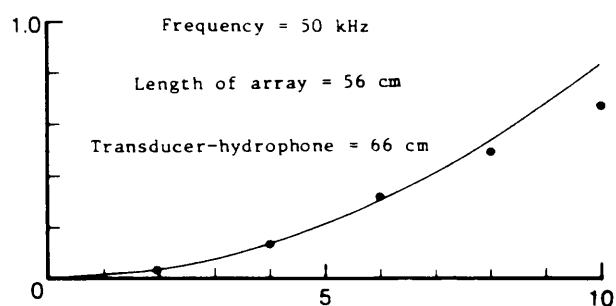
Fig 21   Phase variation of the truncated parametric array. —
Phase centre at 35 cm from the hydrophone.
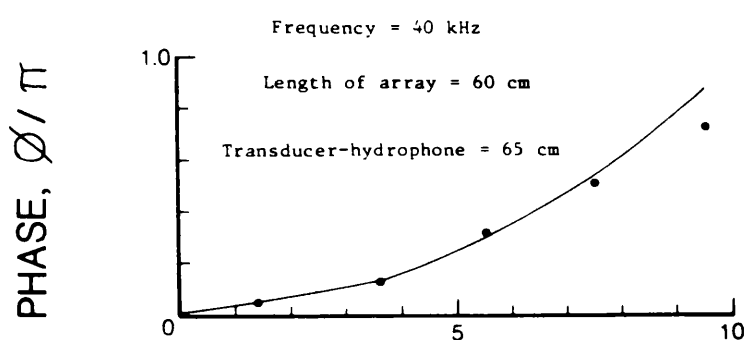
Fig 22   Phase variation of the truncated parametric array. —
Phase centre at 32 cm from the hydrophone.
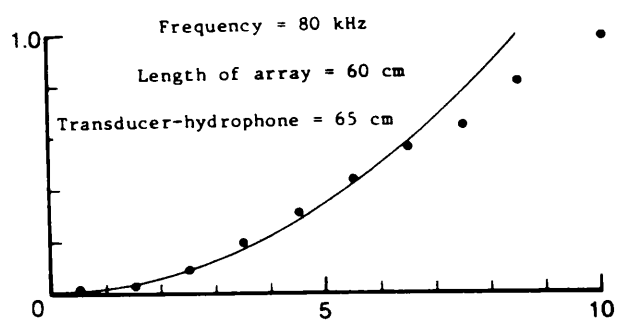
Fig 23   Phase variation of the truncated parametric array. —
Phase centre at 38 cm from the hydrophone.

DISTANCE OFF ACOUSTIC AXIS, ρ (cm)

Chapter 5   Rough Surface Scattering Measurements And Calculations

5.1   Setting Up The Model Rough Surface For Scattering Measurements

The properties and statistics of the model surface were considered in chapter 3; in this section the arrangement of the surface for taking scattering measurements is described.   A dexian framework was built to hold the surface, which allowed the surface to be rotated about a vertical axis, and tilted forwards or backwards.   The framework was attached to lead weights to overcome the buoyancy of the model rough surface underwater.   The photograph in figure 1 shows how the rough surface was held, and the experimental arrangement used for the scattering measurements.

Since the surface could not be acoustically aligned to be in a vertical plane perpendicular to the incident radiation, because of its roughness, a perspex sheet 60 x 60 x 1.5 cm was acoustically arranged to be in the plane that the surface was required to occupy. Firstly the transducer was aligned to have its acoustic axis horizontal and parallel to the rails that ran along the sides of the tank.   The perspex sheet was then hung vertically in the water at a distance of 100 cm from the transducer.   The transducer was traversed in a vertical plane at right-angles to the rails while transmitting a continuous wave pulse at 100 kHz.   The phase of the signal reflected from the perspex sheet was monitored with an on-axis hydrophone fixed in front of the transducer.   The sheet was then aligned to minimise the phase variation of the reflected signal as the transducer moved in its vertical plane.   This could be reduced to $\pi/8$.   The sheet was then in a vertical plane, parallel
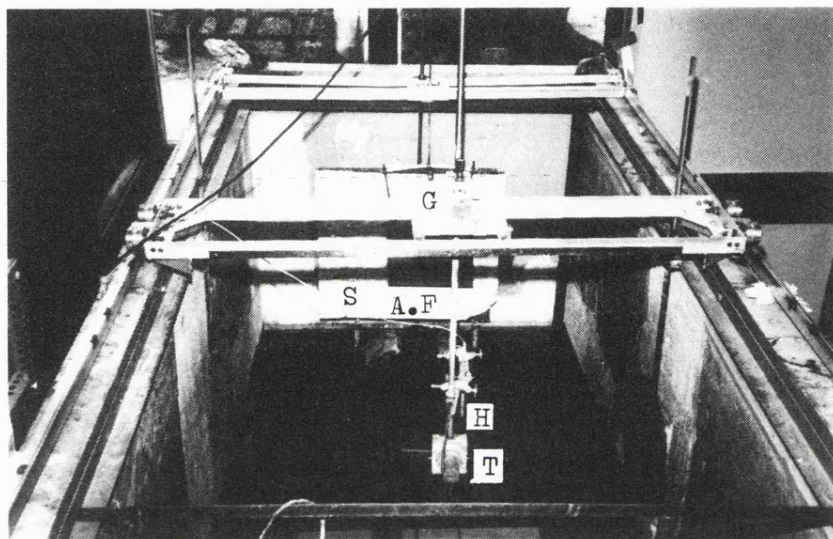
Fig 1   Experimental arrangement for the scattering measurements

T—Transducer H—Hydrophone A.F—Acoustic Filter G—Gantry S—Surface

to that which the transducer moved in, and at right-angles to the
acoustic axis. The rough surface was then placed close to the
perspex sheet and aligned to lie in the same vertical plane. The
adjustments on the framework which held the rough surface were
locked and the surface fixed in this normal incidence position
for the scattering measurements.

5.2 Measurement Of The Scattered Intensity

Measurement of the normalised scattered intensity was
common to all of the scattering experiments, and is therefore
described here before any of the particular experiments are
considered.

All the measurements were taken with the transducer and
hydrophone at near normal incidence to the rough surface. The
normally incident acoustic radiation insonified an area on the
rough surface with a quasi-monochromatic pulse. The transmitting
and receiving systems used were those shown in figure 2 of
chapter 4, with one exception which is discussed later. The centre
and modulating frequencies used to obtain the primaries were
continually monitored using a frequency counter. The primary voltage
across the transducer, and the difference frequency voltage level
generated by the outgoing transmitted pulse were also frequently
checked. The acoustic filter was centred on the acoustic axis at
approximately 10 cm in front of the rough surface.

To measure the ensemble average intensity, the transducer and
hydrophone positions for a particular experiment were fixed

relative to one another and at a constant distance from the rough

surface. The transducer illuminated an area on the rough surface

through the acoustic filter at one of the difference frequencies.

The backscattered signal was received at near normal incidence

on the hydrophone and recorded. The transducer, hydrophone and

acoustic filter were then displaced with no relative movement between

the three. Keeping the transmitting and receiving systems constant,

the backscattered signal from the second position was measured. This

procedure was generally repeated about thirty-six times, although

in some cases fewer values were measured, at an average spacing close

to 5 cm, thereby covering a total surface area of approximately

25 x 25 cm² Spacings of 5 cm gave backscatter signals which were

considered to be of sufficient variability to be treated as

independent. The insonified region was restricted to this central

portion of the model rough surface so that edge effects could be

neglected. From these measurements the mean intensity was

calculated at one frequency for fixed values of the distances

between the transducer, hydrophone and surface. The normalising

intensity was then measured and the normalised intensity calculated.

The next frequency was chosen, the procedure repeated and the

method continued over the frequency range of investigation to

obtain the frequency response of the surface for that particular

experiment.

5.3 Measurement Of The Normalising Intensity

The dimensions of the expanded polystyrene sheet used for

normalisation were 50 x 40 x 5 cm. Reflections from this sheet

were measured relative to an air-water interface and the results
are shown in figure 2. For these measurements an experimental
error of about 1 db is indicated. The values are scattered about a
relative reflection value of one. The magnitude of the reflection
coefficient between expanded polystyrene and water was therefore
taken to be unity. Reflection measurements were made on the
polystyrene between 20-300 kHz, with the same experimental
arrangements, ten weeks apart, and were generally found to be
within 10% of one another. This showed that consistent normali-
sation could be obtained.

After taking a set of measurements on the rough surface at
one frequency, the acoustic filter, hydrophone and transducer were
usually turned through 180° to face the plane surface situated at
the opposite end of the tank to the model rough surface. With
conditions identical to those used when measuring the scattered
intensity, the reflected intensity I_o, was measured and used for
normalisation.

5.4 Calculation Of The Normalised Intensity

The amplitude of the received voltage, V was measured. From
these measurements the total normalised mean scattered intensity
$<I>_T$ for a particular frequency and experimental arrangement was
calculated using

$$\frac{<I>_T}{I_o} = \frac{1}{N} \sum_{i=1}^{N} (V^2_i / V^2_o) \qquad 5-1$$
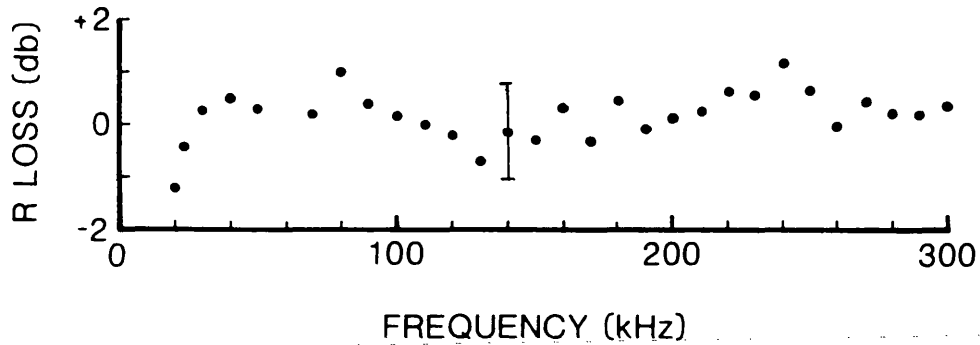
Fig 2   Reflection loss of the plane expanded polystyrene surface
relative to an air-water interface.
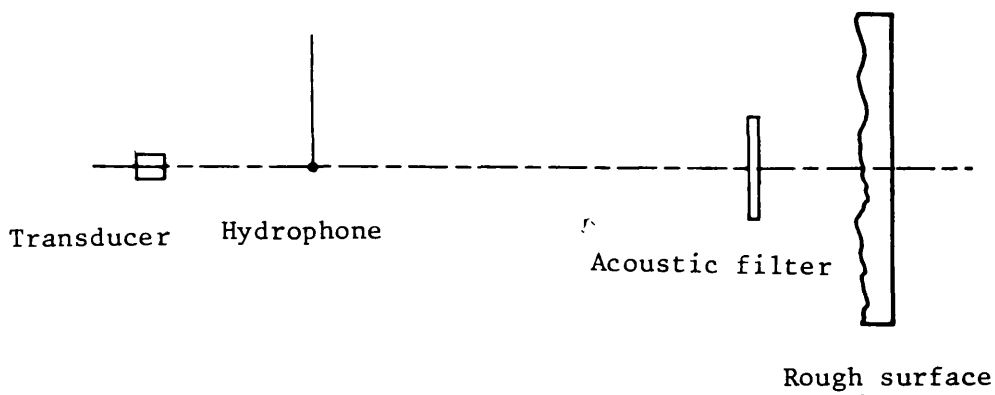
Fig 3   Scattering geometry.   The transducer insonifies the surface
through the acoustic filter at near normal incidence and the hydro-
phone measures the backscattered signal.

where I_o and V_o were the magnitude of the normalising intensity

and voltage respectively, and N is the number of intensity measure-

ments made. The standard error of $<I>_T$ was calculated as

$$\sigma(<I>_T) = \sigma(V^2)/\sqrt{N} \qquad\qquad 5\text{-}2$$

The usage of $\sqrt{N}$ is probably not strictly correct since each area of

insonification had a degree of overlap with other areas of

insonification. However as previously mentioned the scattered

signal level was unpredictable from one area to another, and

treating the readings as independent was judged to be

reasonable. A 10% standard error was estimated for the

normalising intensity

$$\sigma(I_o) \approx 0.1\ I_o \qquad\qquad 5\text{-}3$$

The combined error was obtained from Kendall and Stuart (44) who

show for a function

$$F = f(x_1, x_2, \ldots\ldots x_k) \qquad\qquad 5\text{-}4$$

the standard error of F is given by

$$\sigma^2 (F) = \sum_{i=1}^{K} [f_i^1 (\bar{x})]^2 \sigma^2 (x_i) \qquad \qquad 5\text{-}5$$

Where $f_i^1 (\bar{x})$ is the first order derivative of F evaluated at its mean value, and $\sigma(x_i)$ is the standard error of x_i . This gives a standard error of

$$\sigma (\langle I \rangle_T / I_o) = \frac{\langle I \rangle}{I_o} [\frac{\sigma^2 \langle I \rangle_T)}{\langle I \rangle^2} + \frac{\sigma^2 (I_o)}{I_o^2}]^{\frac{1}{2}} \qquad \qquad 5\text{-}6$$

The measured values of $\langle I \rangle_T / I_o$ were obtained using equation 5-1, with an estimated experimental standard error derived from equation 5-6.

5.5 Theoretical Estimates Of The Scattered Intensity

The observed data is compared with three theoretical expressions. The first is that derived by Boyd and Deavenport (20) for the normalised scattered intensity. For normal incidence backscattering their equation (1-12 of chapter one) reduces to

$$\frac{\langle I \rangle_T}{I_o} = R^2 \exp(-g) + \frac{R^2 W^2}{16} \frac{(R_0 + R_1)^2}{R_0^2 R_1^2} \frac{T^2}{h^2} H(g)[1-\exp(-g)] \qquad 5\text{-}7$$

$$H(g) = L(g) \ (B = 0, \ s = 0) = g \exp(-g) \sum_{n=1}^{\infty} \frac{g^n}{n n!}$$

Where R is the reflection coefficient, W is the radius of the
insonified area, R_0 is the distance of the apparent conventional
source from the rough surface, R_1 is the distance from the surface
to the hydrophone, T is the surface autocorrelation length, h is
the root-mean-square height of the surface and g is the roughness
parameter defined in chapter 2. This formula was obtained by
accurately deriving the coherent intensity, and then modifying
the incoherent intensity developed by Beckmann and Spizzichino (15)
for a Fraunhofer phase approximation.

The second expression to be compared with the measured values
of the scattered intensity is obtained by deriving the scattered
intensity in the manner outlined in chapter 2 but using a first
order phase approximation to obtain the incoherent intensity.

$$\frac{<I>T}{I_0} = R^2 \exp(-g) + \frac{R^2 W^2}{32} \frac{(R_0 + R_1)^2}{R_0^2 R_1^2} \frac{T^2}{h^2} H(g) \qquad 5\text{-}8$$

The coherent components are identical to those in equation 5-7,
while the incoherent terms differ by a factor of $(2[1-\exp(-g)])^{-1}$.
The factor of a half arises because of the Gaussian beam profile
used to derive equation 5-8, and the $[1-\exp(-g)]$ is not present,
since it was empirically introduced into equation 5-7.

The third expression used to predict the scattered intensity
is given by

$$\frac{<I>T}{I_o} = R^2 \exp(-g) + \frac{R^2 W^2}{32} \frac{(R_0 + R_1)^2}{R_0^2 R_1^2} \frac{T^2}{h^2} Z(g) \qquad\qquad 5-9$$

$$Z(g) = g \exp(-g) \sum_1^\infty \frac{g^n}{(sT^2 + n)n!}$$

$$s = \frac{1}{2}\left[\frac{1}{W^2} + g\left(\frac{WR_s}{h\gamma}\right)^2\right]$$

$$Z(g) = L(g)(B = 0)$$

$$H(g) = Z(g)(s = 0)$$

Where $\gamma = -(\cos\theta_1 + \cos\theta_2)$ and $R_s = \frac{1}{2}((1/R_0)+(1/R_1))$ equation

5-9 is identical to equation 5-8 for $s = 0$. This formula was

derived in chapter 2 using a Fresnel phase approximation with

some simplification of the second order terms. As the value of

s increases, $Z(g)$ decreases, and the predicted scattered intensity

is reduced in comparison with equations 5-7 and 5-8. The effect

of varying s upon $Z(g)$, which is equal to $L(g)$ when $B = 0$, was

illustrated in figure 3 of chapter 2. This showed that the magnitude

of sT^2 could have a pronounced effect on $Z(g)$ particularly for low

and intermediate values of g .

An estimate for the error in the predicted mean intensity was

also calculated. For any of the three formulae used, measured

values of R, W, R_0, R_1, T and h needed to be taken in order to

calculate the mean scattered intensity. There was an uncertainty

in each of these measurements which required consideration.
The standard errors of T and h were given in chapter 2 and
reasonable estimates were made for the other terms giving

$$\sigma(h) = 0.05h \qquad \sigma(T) = 0.10T \qquad \sigma(W) = 0.05W$$

$$\sigma(R) = 0.05R \qquad \sigma((R_0 + R_1)/R_0 R_1) = 0.05 (R_0 + R_1)/R_0 R_1$$

Applying equation 5-5 to 5-9 yields 5-10. The error in g and s
has been ignored so that the estimated standard error in equation
5-10 could be easily obtained.

$$\sigma^2(<I_T>/I_o) \simeq [\frac{2\sigma(R)}{R}]^2 [R^2 \exp(-g)]^2 + [(\frac{2\sigma(R)}{R})^2 + (\frac{2\sigma(W)}{W})^2$$

$$+ (\frac{2\sigma(T)}{T})^2 + (\frac{2\sigma(h)}{h})^2 + (\frac{2\sigma((R_0 + R_1)/R_0 R_1)}{(R_0 + R_1)/R R_1})^2]$$

$$[\frac{R^2 W^2}{32} \frac{T^2}{h^2} \frac{(R_0 + R_1)^2}{R_0^2 R_1^2} Z(g)]^2 \qquad\qquad 5\text{-}10$$

In equation 5-10 a cross product term between the coherent and
incoherent terms arising from the differentiation of R has been
neglected to keep the expression simple. Equation 5-10 has been
used when calculating the scattered intensity from equation 5-9

and the predicted values for the intensity are represented by an area of hatching which contains the mean value and one standard error.

5.6 First Set Of Scattering Measurements From The Rough Surface

5.6.1 Measured values

For the first set of measurements on the normal incidence backscattered intensity, the transducer was located at a fixed distance of 100 cm from the model rough surface. The acoustic filter was centred on the acoustic axis at approximately 10 cm in front of the rough surface. The hydrophone was placed on the acoustic axis between the transducer and the acoustic filter at four different distances from the rough surface. This is shown earlier in figure 3.

A 100 cm separation between the transducer and rough surface was chosen initially because for this distance, the area of insonification covered at least a few correlation lengths, yet was also small enough to obtain a number of independent measurements of the scattered intensity. The radii of the illuminated areas were for most frequencies relatively small compared to the distance from the apparent source centre to the surface. A premise in the theoretical development in chapter 2 assumed the insonified area to be much smaller than the separation between the apparent source and the surface.

This transducer-surface separation also allowed the on-axis

receiving hydrophone to be moved from a position where the radius

of insonification was small compared with the distance between the

receiver and the surface, to one where they had more similar values.

The distances chosen for the separations between the surface and

hydrophone were 70, 50, 30 and 20 cm. The first of these conformed

to the radius of the insonified area being much smaller than the

receiver distance, while in the latter cases the inequality was

adhered to less strongly. The magnitude of s was larger for nearer

receiving distances, and this allowed the value of equation 5-9

to be tested.

For each of the four positions occupied by the hydrophone

the mean normalised backscattered intensity was measured over a

range of frequencies. For these measurements the hydrophone was

on the acoustic axis. Care was exercised to ensure the same

hydrophone orientation was used for all measurements.

The need to take a number of intensity measurements to obtain

a reasonable estimate for the mean intensity is illustrated in

figure 4, where fluctuations in the normalised intensity for

particular frequencies as different areas on the rough surface

were insonified are shown. These were taken from measurements

where the receiver was 50 cm from the rough surface. At low

frequencies where the coherent component of the scattered intensity

dominated, the signal variations are relatively small; however at

the higher frequencies the fluctuations are much larger.

The backscattered near-normal incidence normalised intensities

measured on the acoustic axis are shown in figures 5, 6, 7 and 8
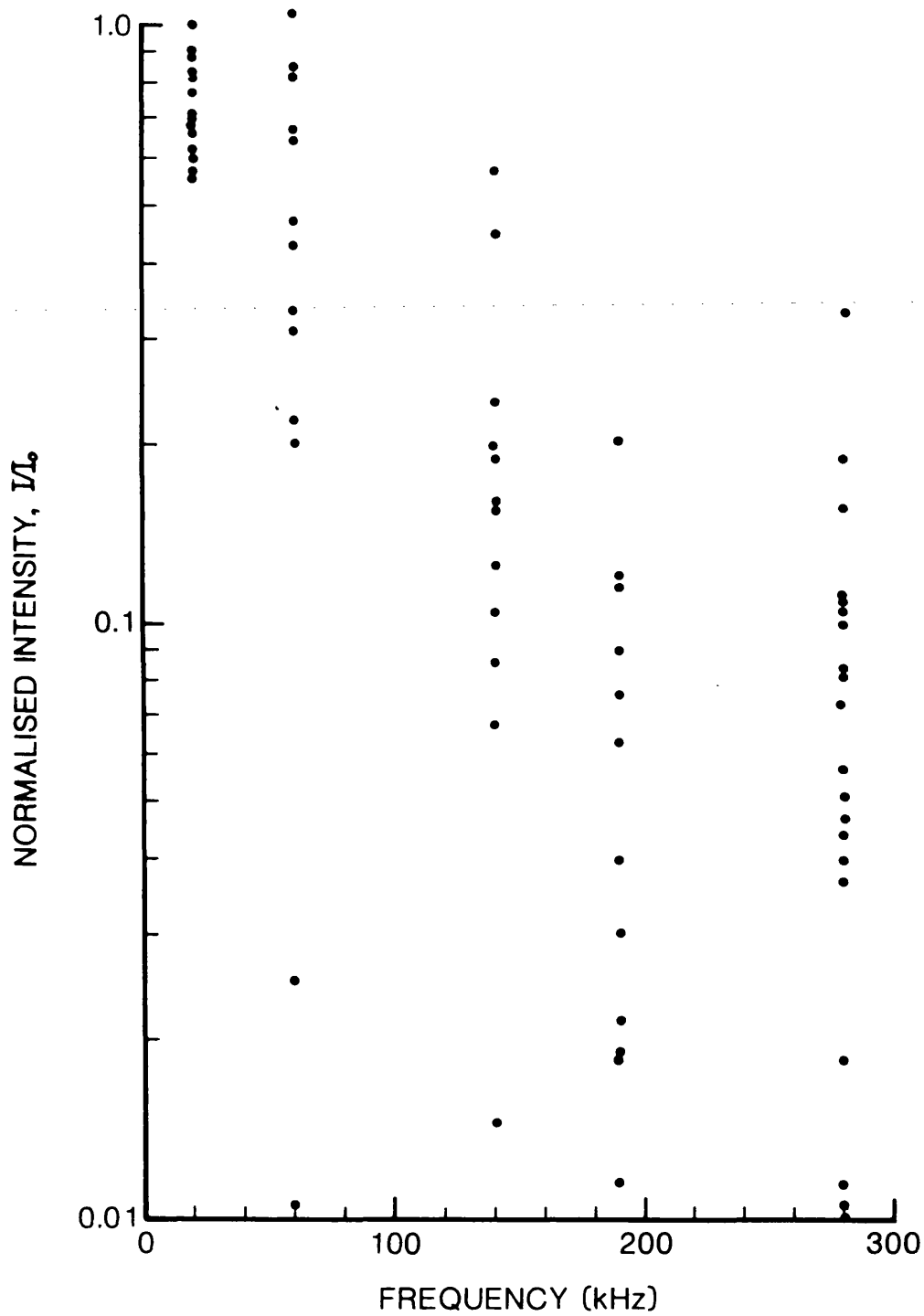
Fig 4   Selection of normalised intensity measurements for a
transducer-surface separation of 100 cm and a hydrophone-surface
separation of 50 cm.   This illustrates the signal variability
for different areas of insonification.

for receiver distances of 70, 50, 30 and 20 cm respectively from the surface, with the transducer at 100 cm from the surface. The abscissa represents the frequency or roughness parameter g, and the ordinate is the normalised scattered intensity in decibels.

The measured normalised intensities, shown by the circles with the error bars, decrease initially as the roughness parameter increases and tend to level out towards the higher values of g. About this general trend is a variation in the mean intensity from frequency to frequency, arising from the normal uncertainities associated with the measurement of a stochastic variable. The estimated error in the normalising intensity would also have increased this variability. As the distance between the hydrophone and surface decreases, the mean normalised scattered intensity increases for the larger values of roughness parameter.

At the low frequencies, when g is much less than unity, the received signal is predominately coherent. At the larger distances for these low frequencies, the small difference between the intensities received from the rough surface and the plane expanded polystyrene surface, are compatible with the estimation for the reflection coefficient of the expanded rigid polyurethane foam calculated from the measured bulk acoustic impedence of the material, and its reflectivity measured relative to the air-water interface. Above 40 kHz the incoherent component becomes important, and begins to dominate the scattered intensity at frequencies higher than 100 kHz. The curves show a dip in the incoherent intensity between 150-200 kHz which is then followed by a relatively steady value of intensity as the frequency changes.
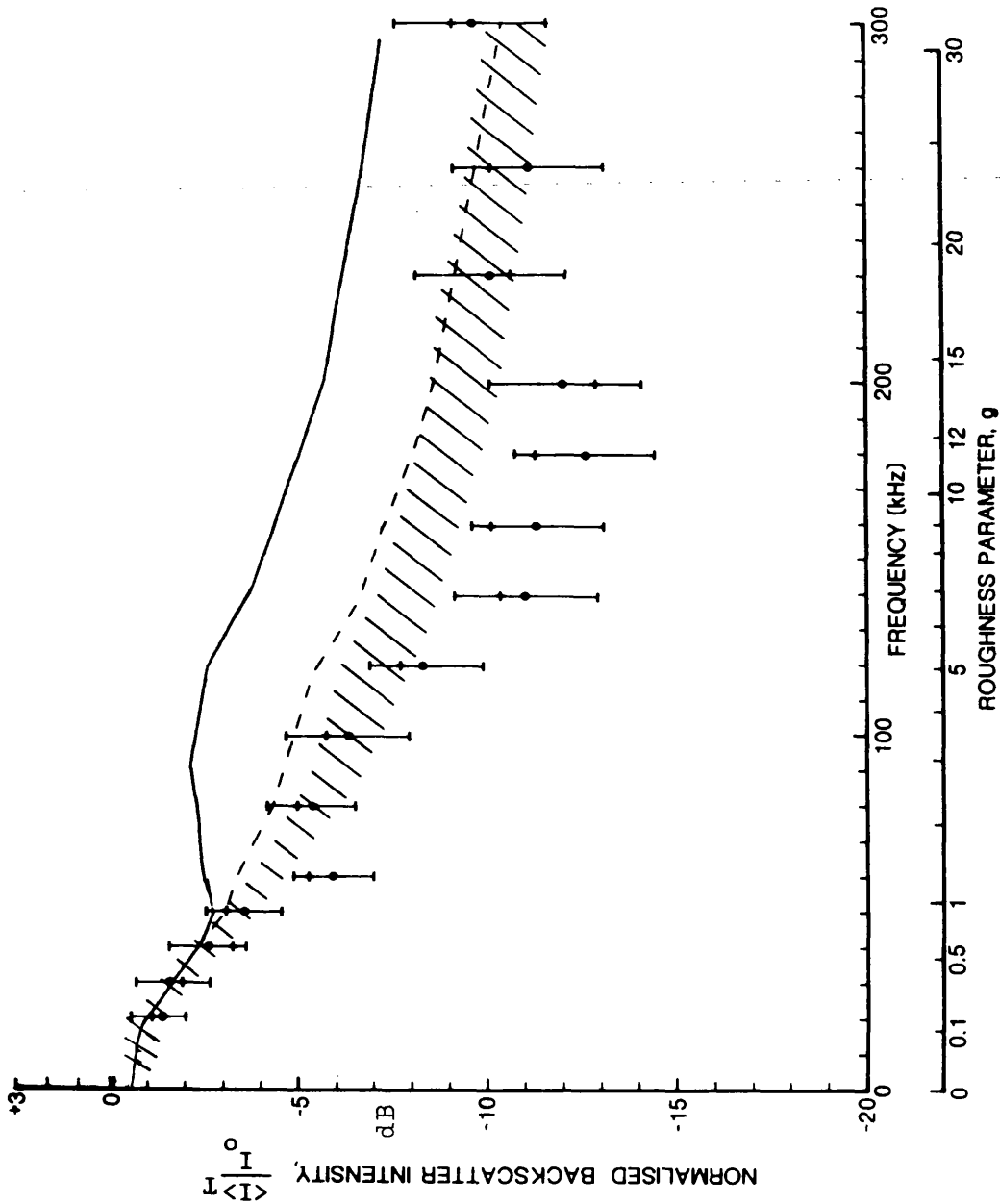
Fig 5   Frequency response of the mean backscattered intensity. Transducer-Surface = 100 cm.   Surface-Hydrophone =

70 cm.   — Equation 5-7.   ——— Equation 5-8.   ///// Equation 5-9, 5-10.   ●Measured + see page 114.
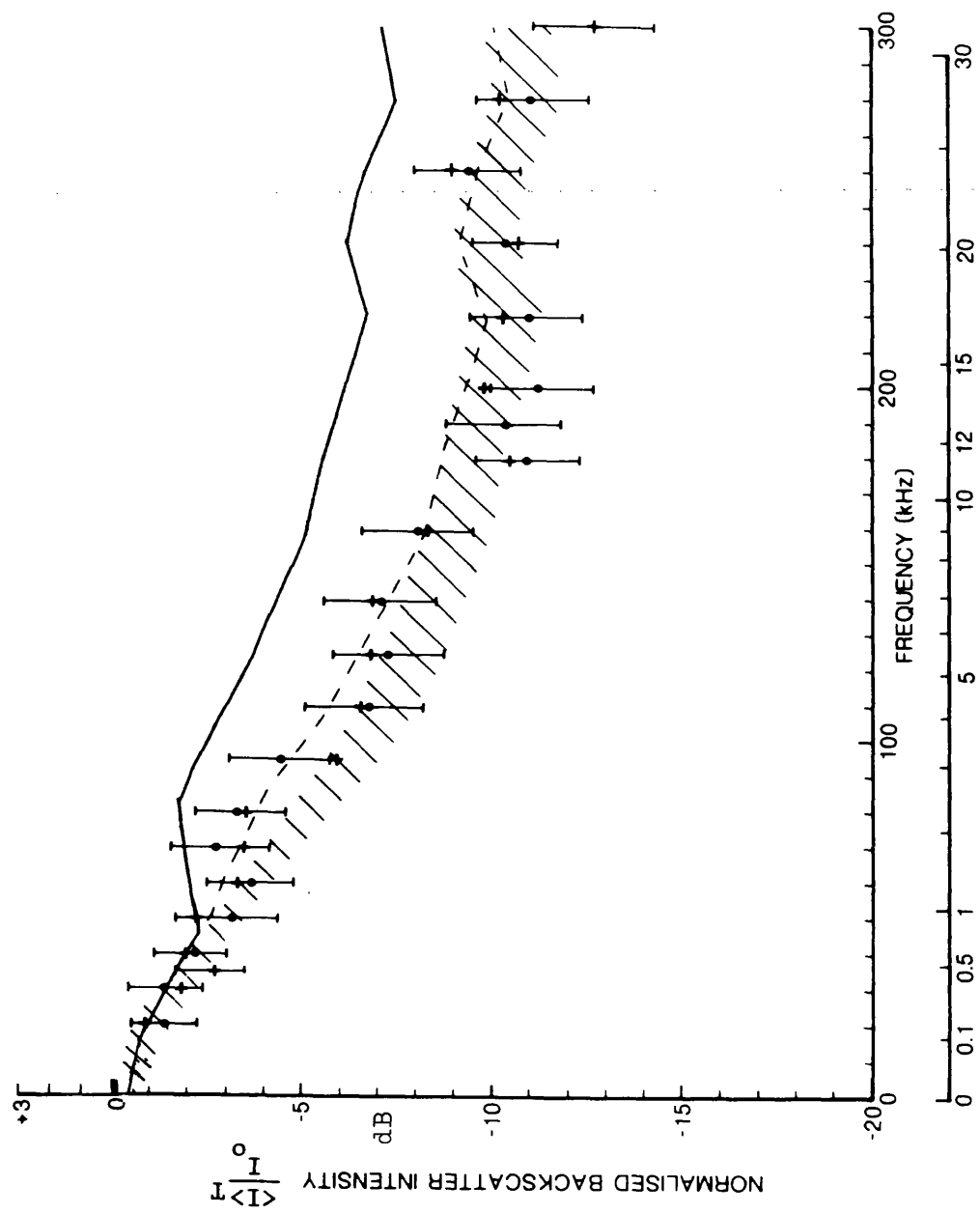
Fig 6   Frequency response of the mean backscattered intensity. Transducer-Surface = 100 cm. Surface-Hydrophone = 50 cm. ── Equation 5-7. ──── Equation 5-8. ///// Equation 5-9, 5-10. ●Measured + see page 114.
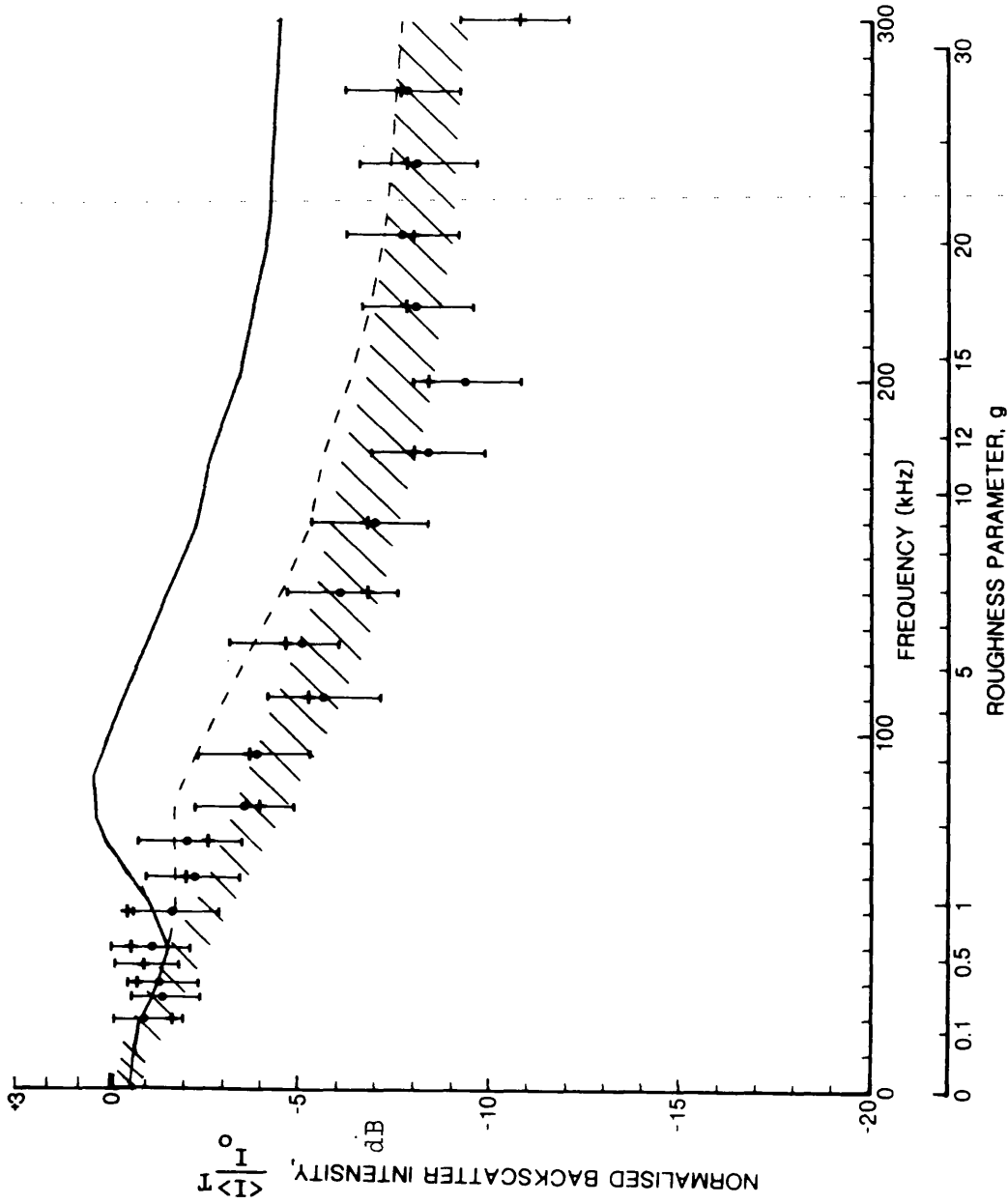
Fig 7   Frequency response of the mean backscattered intensity. Transducer–Surface = 100 cm.   Surface–Hydrophone =

30 cm.   — Equation 5-7.   ----- Equation 5-8.   ///// Equations 5-9, 5-10.   ●Measured ⁺ see page 114.
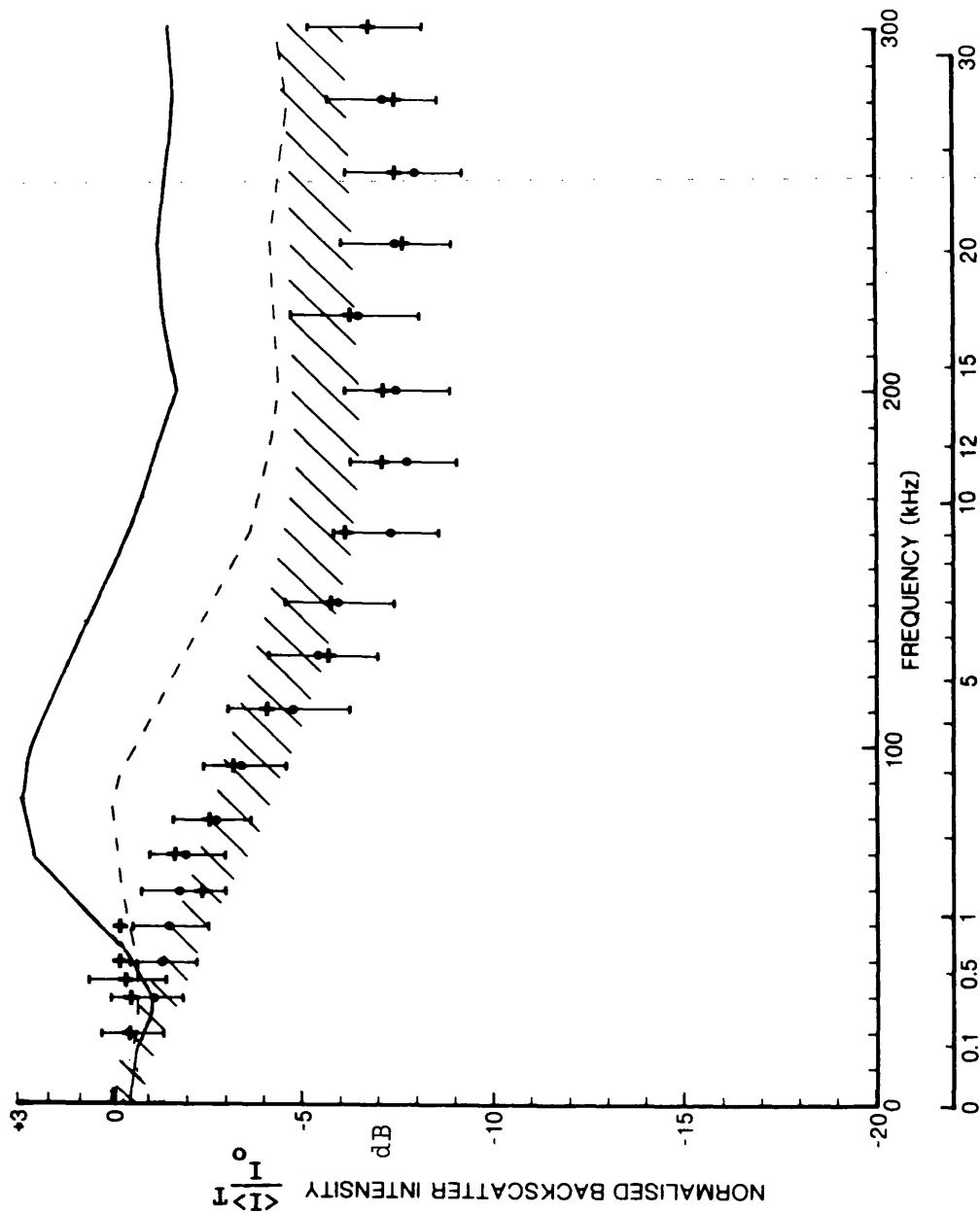
Fig 8   Frequency response of the mean backscattered intensity.   Transducer-Surface = 100 cm.   Surface-Hydrophone = 20 cm.   — Equation 5-7.   ---- Equation 5-8.   ///// Equations 5-9, 5-10.   ●Measured + see page 114.

5.6.2 Comparisons of the predicted intensities with the measured

values

Three theoretical curves were compared with the observed data.
To calculate the curves, the values of T and h used were those
obtained in chapter 3, R = 0.93, R_1 has the four values of the
hydrophone-surface separation, R_o is the apparent source distance
given in figure 19 of chapter 4 and the radius of insonification,
W, is taken from figure 17 chapter 4. The first of the three
to be considered is the solid line. This compares the predictions
of equation 5-7 with the normalised intensities shown in the four
figures. There is reasonable agreement at the lower values of g.
In this region the coherent component has a strong influence upon
the scattered intensity, and this indicates that the coherent
component is being estimated with reasonable accuracy. Since all
three estimates of intensity have the same exponential form for the
coherent component, similar agreement will be obtained using the
other two curves for low values of g and this can be seen in the
four figures. However, at the higher frequencies or larger values
of g, equation 5-7 overestimates the scattered intensity. This
became more pronounced as the hydrophone was moved closer to the
rough surface.

The second set of curves compared with the observed data are
shown by the broken line. These were calculated using equation 5-8.
Reasonable agreement was obtained for the range of roughness para-
meters investigated for the larger separations between the model
rough surface and the hydrophone. For the cases where the distance
between the hydrophone and the surface were 30 and 20 cm, the

calculated scattered intensities were in poorer agreement with the experimental values, particularly for the intermediate range of rougness parameter. This is the region where the value of sT^2 was expected to have an influence on the total scattered intensity.

The third comparison between the measured and calculated normalised scattered intensities was carried out using equation 5-9 with theoretical 'error bars' obtained using equation 5-10. These give the shaded areas on the figures. The calculation of these values was based on the Fresnel phase approximation and they are in better agreement with the experimental values than either of the two other curves. In the region where the values of sT^2 become important in the calculation of the scattered intensity, the effect this term has on the predicted scattered intensity is to give calculated values closer to those measured. This is especially noticeable for the case when the mean scattered intensity was measured at receiver distances of 20 and 30 cm. Therefore retaining the Fresnel approximation in the development of chapter 2 has led to values for the normal incident normalised backscattered intensity which are an improvement on those obtained using a Fraunhofer phase approximation.

The values for sT^2 are shown in figure 9. These show the values for sT^2 as the frequency is increased and the receiving range reduced.

5.6.3   Measurements with no acoustic filter

Mean near normal incidence backscattered intensities under identical conditions to those above were measured without the
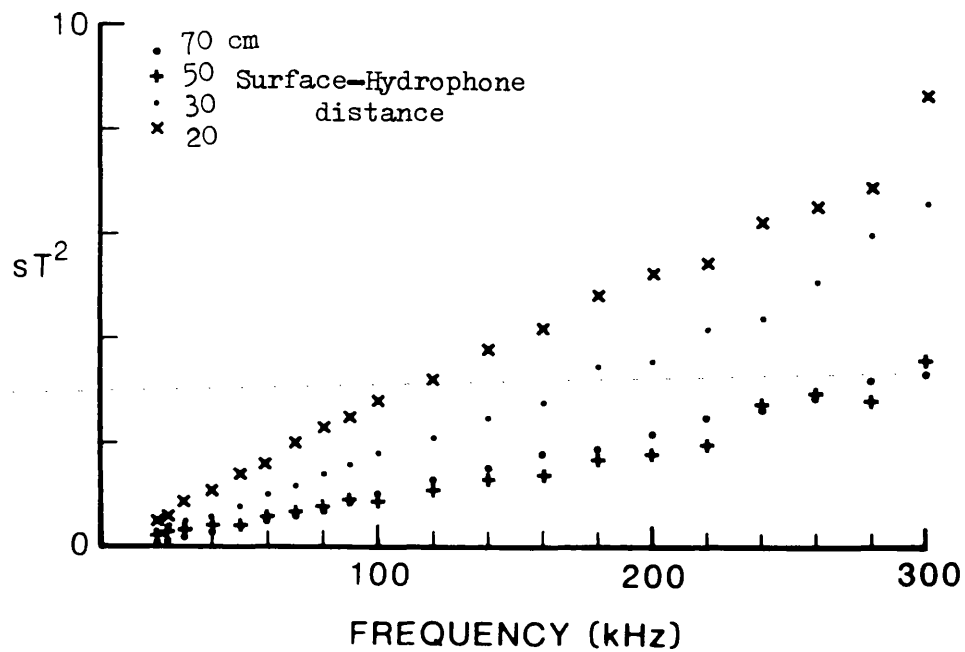
Fig 9 Values of sT² for the transducer-surface distance of
100 cm as the frequency and hydrophone position is altered.
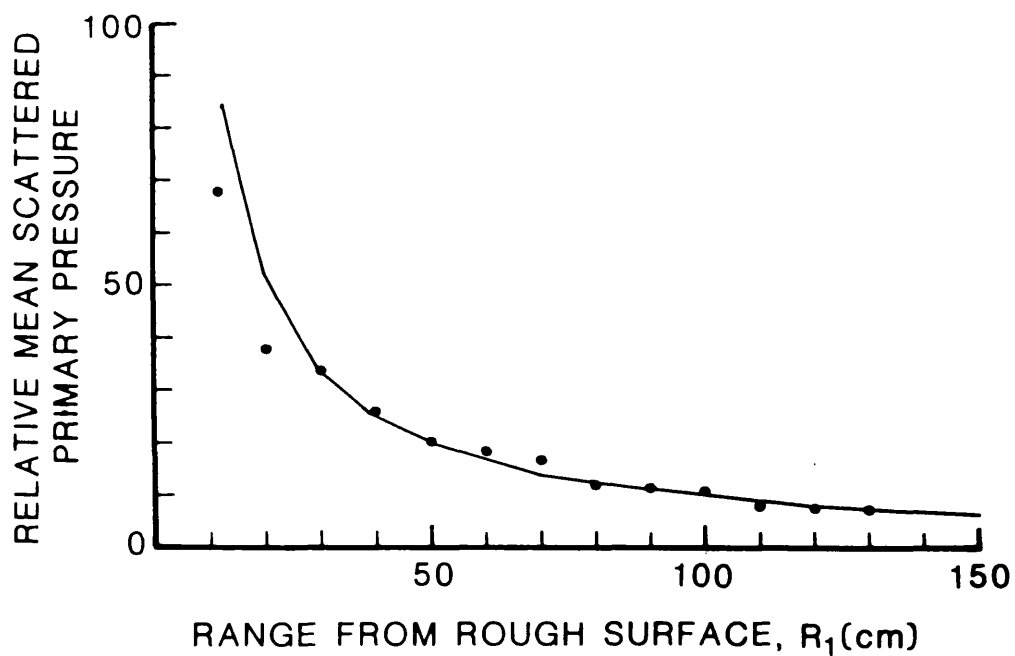
Fig 10 Mean scattered axial   primary pressure variation as
the hydrophone-surface separation increases. - PR_1 = constant;
spherically spreading curve centred on the rough surface.

acoustic filter in front of the rough surface. The effect of the

scattered primaries was considered by observing the scattered axial

intensity levels averaged over 22 positions on the rough surface

taken at 1 MHz. The average primary scattered axial intensities

are shown in figure 10. An approximate 1/R fall off from the sur-

face was observed, thus the surface would probably have acted as a

partial truncating screen for the primaries, however the effect-

iveness of truncation was difficult to quantify and so this led to

the use of the acoustic filter in the previous sets of measurements.

The scattering measurements taken without the acoustic filter

are shown as crosses in figures 5, 6, 7 and 8. The error bars

have the same values as those centred on the solid circles. Norma-

lisation measurements took place with the acoustic filter in front

of the plane surface since this surface did not have a truncating

effect on the primaries. When normalising the scattered intensity,

due allowance was made for the two-way loss through the acoustic

filter.

These measurements are consistently very similar to those taken

with the acoustic filter. Since R_o the apparent source distance and

the area insonified were similar to those measured at the surface

when the filter was used, the surface was reasonably efficient at

truncating the parametric array.

5.7 Measurement Of The Coherent Intensity

The coherent component of the signal was measured by averaging

the pressure with regard to phase. The transducer was at 100 cm from

the rough surface and insonified the surface at normal incidence.
The hydrophone was placed on the acoustic axis at 70 cm from the
surface. Since the normalised scattered signals were very similar
with and without the acoustic filter present, the filter was not
used. For these measurements the hydrophone was fixed to the trans-
ducer mounting so that no relative movement could occur. Measure-
ments were restricted to below 100 kHz to reduce the effect of
phase shifting which would have been introduced by relative movement
between the surface and the transducer.

The coherent measurements are the exception mentioned in
section 5.2, since the received signal after the usual amplifying
and filtering was fed into a transient recorder, and the digitised
signal delivered into a signal averager. The oscilloscope was used
to measure the output from the averager. The signal averager stored
the scattered signal from one area of surface insonification. By
moving the transmitter and receiver together, another area of the
rough surface was insonified. The backscattered signal from this
area was added, with regard to phase, to the stored signal received
from the first area, and the sum stored. In this manner forty areas
were insonified for each frequency and the received signal summed.
This final signal was divided by the number of signals averaged over
to give the mean value of the pressure with regard to phase <p>.
By definition, the square of this term is the coherent component of
the scattered intensity. Normalisation was carried out as usual.
For a Gaussian surface, the coherent component is given by

$$\langle p \rangle^2 / p_0^2 = R^2 \exp(-g) \qquad\qquad 5\text{-}11$$

$$\therefore \quad \ln[R^2 p_0^2 / \langle p \rangle^2] = (16\pi^2 h^2 / c^2) f^2 \qquad\qquad 5\text{-}12$$

A graph of $\ln[R^2 p_0^2 / \langle p \rangle^2]$ versus frequency squared is shown in figure 11a. Using the gradient from the graph, the root-mean-square height of the surface can be calculated. This was estimated to be

$$h = 2.3 \pm 2 \text{ mm}$$

Figure 11b shows the more usual $10 \log [\langle p \rangle^2 / p_0^2]$ versus g, where g was calculated using h = 2.3 mm. The value of the root-mean-square height compares favourably with that of 2.2 mm calculated using the measured surface statistics.

The exponential decaying form for the coherent intensity was derived on the basis that the surface had a Gaussian height distribution; there was no necessity to specify the autocorrelation function. Since the measurements closely follow this form, weight is added to the conclusion drawn in chapter 3 that the surface had a characteristic function that was approximately Gaussian.
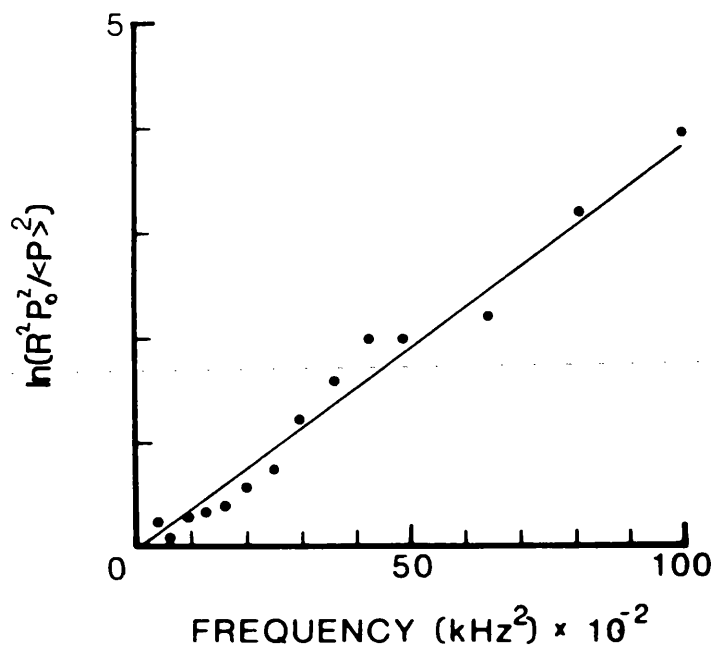
Fig 1.1a   Coherent component of the scattered intensity versus frequency - least square fit to the data.
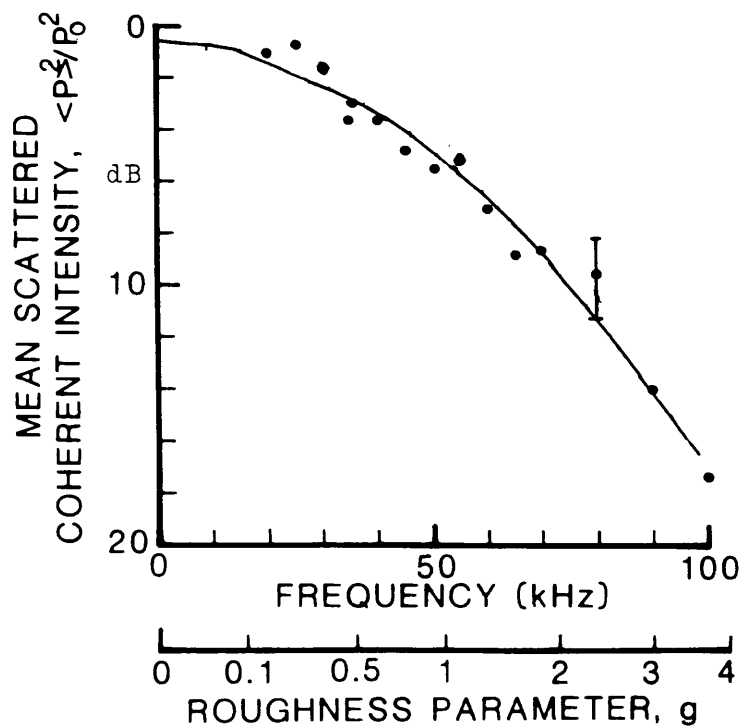
Fig 11b   Coherent component of the scattered intensity versus frequency $-R^2\exp(-g)$ for h = 2.3 mm.

5.8   The Second Set Of Scattering Measurements From The Rough Surface

5.8.1   Measured values

In this second series of experiments both the hydrophone and transducer were moved towards the rough surface. The hydrophone again occupied receiver positions that were 70, 50, 30 and 20 cm from the surface. However, for these measurements the transducer remained at a fixed 16 cm behind the hydrophone. For the larger distances from the rough surface, the values of R_0 and R_1 are again larger than the radius of the area of insonification. These were both reduced while the insonified area remained approximately constant for a particular frequency, and the effect on the scattered intensity was investigated.

To obtain each measurement of the mean near-normal incident backscattered intensity, 36 observations of the intensity were made. For all these measurements the acoustic filter was centred on the acoustic axis 10 cm in front of the rough surface. The acoustic filter was used because there was no guarantee that the scattered primaries contributed negligible secondary levels in the experiments where the transducer was in close proximity to the rough surface.

Unlike the previous set of experiments where for the majority of measurements the transducer and hydrophone had their own gantry arrangements, in this case the hydrophone was rigidly attached to the transducer mountings at 16 cm in front of the transducer. The hydrophone was also displaced 2.5 cm off the acoustic axis to prevent it from interfering with the transmitted signal. To ascertain

whether this displacement was important, beam profile measurements were made which indicated that the maximum error introduced into the coherent component of the scattered intensity was -0.5 db. Calculations on the incoherent intensity yielded a similar error, and this was for the case when the hydrophone was closest to the surface and the displacement error was at a maximum. Therefore when comparing these measured values with the predicted estimates of the scattered intensity, calculations were made as though the hydrophone was centred on the acoustic axis.

The measured values for the normal incidence backscattered normalised intensities are shown in figures 12, 13, 14 and 15, where the distances between the surface and the hydrophone was 70, 50, 30 and 20 cm respectively. The abscissa is the frequency or roughness parameter and the ordinate is the scattered normalised intensity in decibels. The measurements again show an initial decrease in intensity as the roughness parameter or frequency increases. At the higher frequencies the reduction in the scattered intensity continues but with a smaller gradient. The values for the scattered intensity follow a relatively smooth curve for the larger transducer and hydrophone distances.

For the measurements in figure 15 where the transducer and hydrophone were closer to the surface, the values were more variable from frequency to frequency than those of figures 12 and 13, and the coherent component was larger. This increase in scatter as the transducer and hydrophone moved closer to the surface could be a phenomenon associated with the observation position or simply intensity variability due to measuring a random variable. Further measurements are required to resolve the point.
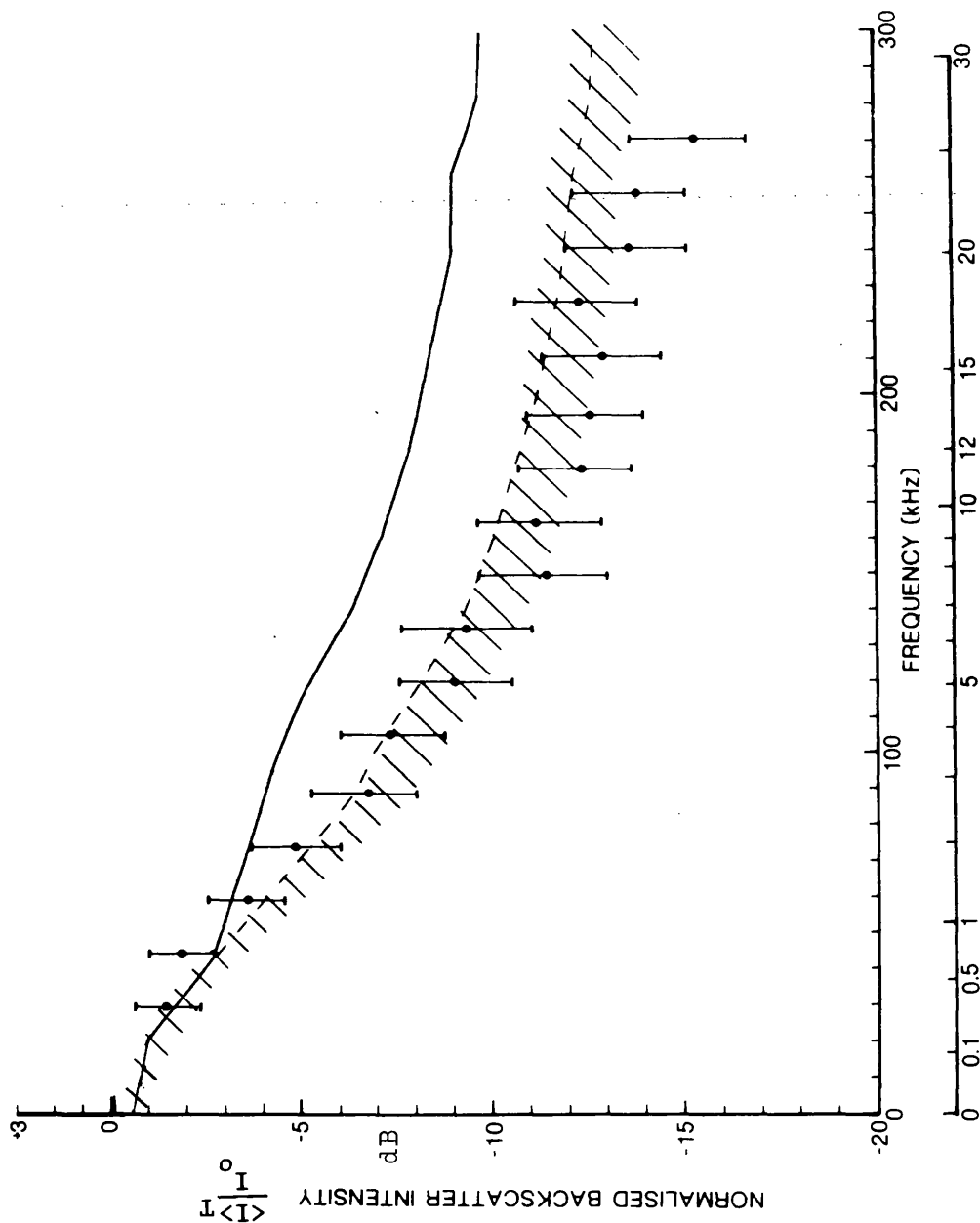
Fig 12   Frequency response of the mean backscattered intensity.   Transducer-Surface = 86 cm.   Surface-Hydrophone = 70 cm.   — Equation 5-7.   ---- Equation 5-8.   ///// Equations 5-9, 5-10.
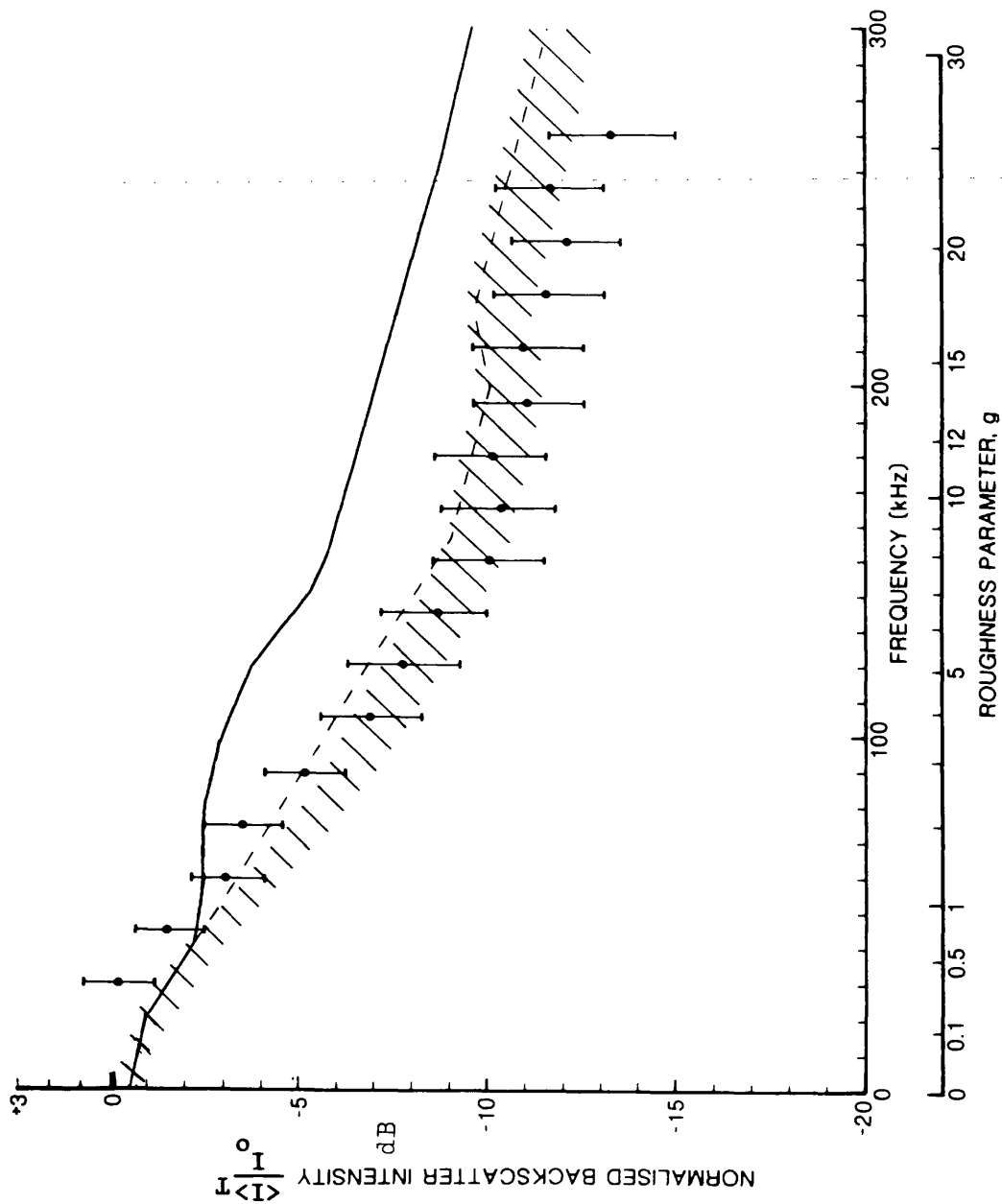
Fig 13   Frequency response of the mean backscattered intensity.   Transducer-Surface = 66 cm.   Surface-Hydrophone =

50 cm.   — Equation 5-7.   —— Equation 5-8.   ///// Equation 5-9, 5-10.
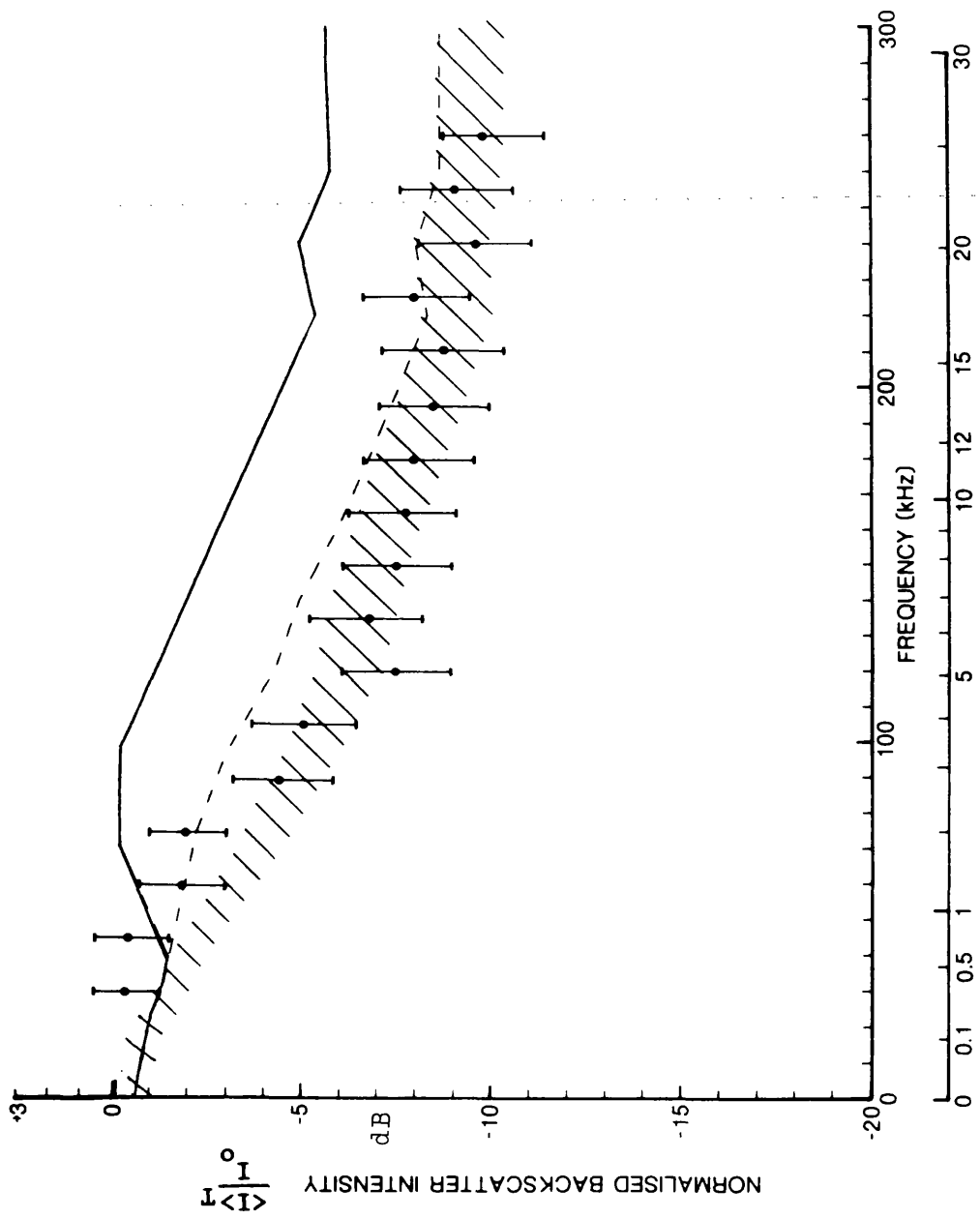
Fig 14   Frequency response of the mean backscattered intensity. Transducer-Surface = 46 cm. Surface-Hydrophone =

30 cm.   — Equation 5-7.   ---- Equation 5-8.   ///// Equations 5-9, 5-10.
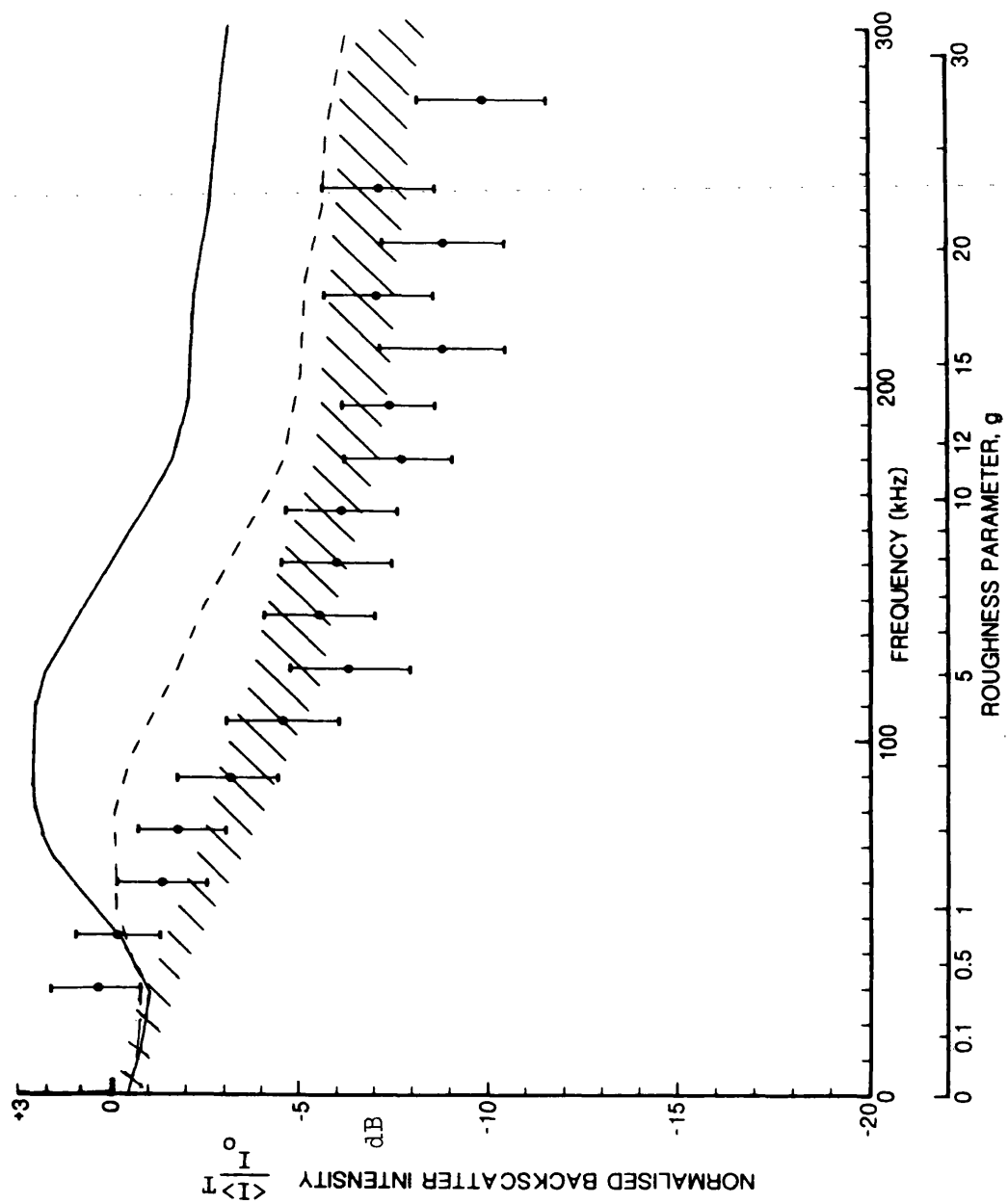
Fig 15   Frequency response of the mean backscattered intensity.   Transducer-Surface = 36 cm.   Surface-Hydrophone =

20 cm.   – Equation 5-7.   ---- Equation 5-8.   ///// Equations 5-9, 5-10.

5.8.2 Comparison of the predicted intensities with the measured values

Three curves are again compared with the experimental data.
Values for h,T,R and R_1 are the same as those used in section
5.6.2. The values for W and R_o are given in figures 18 and 20
respectively of the previous chapter. The solid line was calculated
using equation 5-7 the broken line was obtained using 5-8 and the
shaded area was computed using equation 5-9 and 5-10.

The values for the mean normalised intensity derived using
equation 5-7, compared favourably with the data at low frequencies,
but overestimated the scattered intensity at higher frequencies.
This was also observed previously. Equation 5-8 yields intensities
close to those measured when the hydrophone and transducer were
furthest from the rough surface, as in figures 12 and 13. When the
hydrophone and transducer moved closer to the surface s increased
and the neglect of this term resulted in less agreement between the
predicted and observed intensities. Values for sT^2 are shown in
figure 16.

Calculating the scattered intensities upon the basis of a Fresnel
approximation produced values in good agreement with experimental
measurements. The principal effect in using this phase approximation
is to reduce the computed scattered intensities and bring them into
closer agreement with the observed values. There is a tendency to
predict intensities at the lower frequencies which are slightly
too low and at the higher frequencies the predictions are too high.
This bias is also observed to a similar extent in figures 5, 6, 7
and 8. The low frequency differences become pronounced in figures
14 and 15. Again this could be due to experimental error since

only one standard deviation is given on the error bars, or an actual

effect which occurred when the transducer and hydrophone were close

to the rough surface. The problem cannot be readily reconciled

without further investigation. At the higher frequencies the

measured values suggest a larger mean-square slope than that

calculated from the measured surface statistics.

5.9   Scattering Measurements Taken At Higher Frequencies

Normal incidence backscattered measurements were also made at

frequencies above 300 kHz by conventional techniques. The 1 MHz

resonance transducer radiated directly at frequencies between 600

1200 kHz. As before the transducer insonified the surface at

normal incidence and the backscattered signal was measured on the

acoustic axis. The separation between the surface and the trans-

ducer was 100 cm and the distance from the surface to the hydro-

phone was 80 cm. The intensity was measured at twenty positions

over the surface and its mean value calculated.

Normalisation was not carried out by reflection from a plane

surface since slight surface roughness on the face of the expanded

polystyrene at these high frequencies could have caused problems.

A surface with the root-mean-square heights of 0.01 cm introduces

-3 db reduction into the coherently reflected signal at 1 MHz.

Normalisation was therefore conducted by transmitting the same

signal level as used in the scattering experiments over a path length

of 180 cm, and receiving the signal on the same hydrophone orientated

to give the same response in both cases.

The hydrophone used for the high frequency measurements was the LC5-2. The effect of placing the hydrophone on the acoustic axis, 20 cm from the transducer reduced the on-axis signal level by a mean value of -1.3 db at 100 cm over the frequency range covered. This value was used to compensate for the normalisation measurements. The influence the on-axis hydrophone had on the beam pattern was not investigated. The beam pattern measurements made over the frequency range 0.9-1.1 MHz were used to estimate the area of insonification. The main lobe directivity of the high frequency beam patterns were in very close agreement with the Gaussian profiles fitted at the e^{-1} point, and the distance from the acoustic axis to the e^{-1} point was used as the radius for the area of insonification.

Difficulties were encountered with the directivity of the LC5-2 hydrophone and the frequency dependence of its directivity, which made some of the data unreliable; these measurements were rejected. The remainder of the normalised intensities are shown in figure 17a.

The measurements cover a roughness parameter range from 128-512. They show a general decrease in scattered intensity as the frequency increases, which is principally ascribed to the reduction in the area of insonification rather than a frequency dependence of the scattered intensity. The error bars are estimated from the standard error of the measured scattered intensities and the normalisation procedure. A value of approximately ±2 db was estimated, as shown in figure 17a.

The predicted normalised intensities using the high frequency limit of equation 5-9 are compared with the experimental data. From equation 2-48b of chapter 2 it can be seen that $Z(g) \approx 1$ for $sT^2 \ll g$,
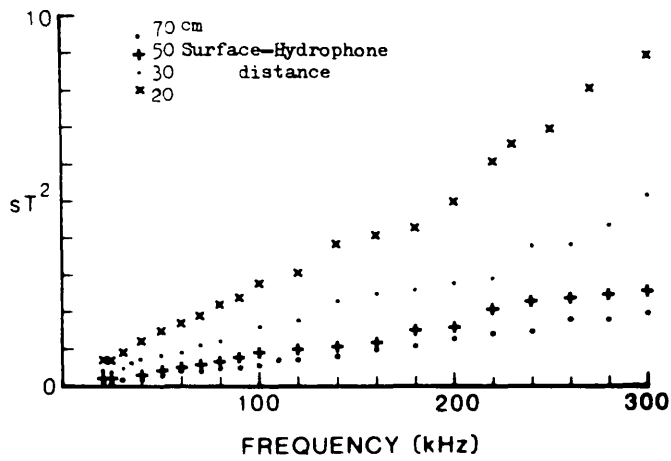
Fig 16 Values for sT² as the transducer and hydrophone distances
from the surface are reduced and as the frequency is changed.
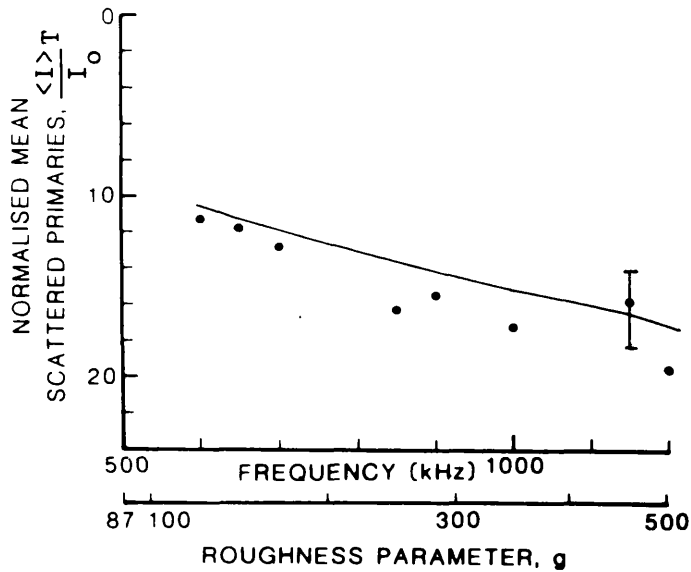
Fig 17a Scattered mean normalised intensity at the primary
frequencies - calculated from equation 5-13.
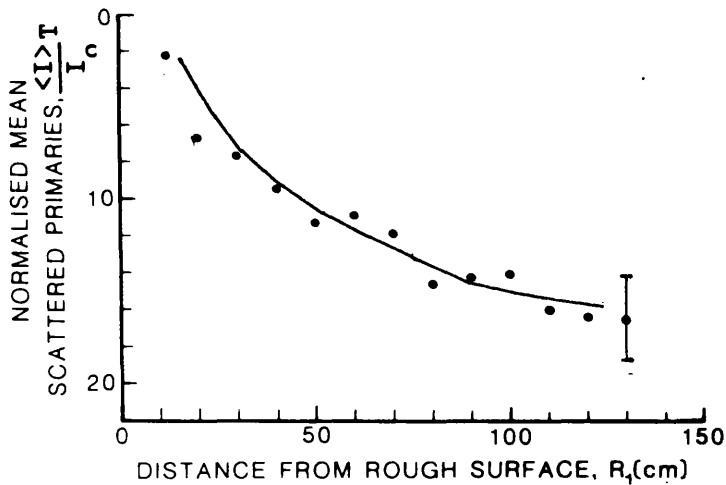
Fig 17b Scattered axial mean normalised intensity -
calculated from equation 5-13.

and $\exp(-g) \approx 0$ for large g; therefore, the scattered intensities
are given by

$$\frac{\langle I \rangle_T}{I_o} = \frac{R^2 W^2}{32} \frac{(R_0 + R_1)^2}{R_0^2 R_1^2} \frac{T^2}{h^2} \qquad 5\text{-}13$$

Considering the very large values of roughness parameter encountered
in this series of measurements, the predicted intensities compare
well with those measured, although higher levels of scattered
intensity are predicted than are observed. This tendency for the
higher frequency scattered intensities to be overestimated was also
noted previously.

The reduction in intensity of the scattered signal was also
measured along the acoustic axis at 1 MHz. This used the same
data as that used to obtain figure 10. The intensity was measured
at 22 positions over a strip of the rough surface, by traversing the
transducer and hydrophone across the surface at one height to obtain
each value of the axial mean intensity. Normalisation intensities
were estimated from the outgoing signal pressure levels measured between
the transducer and rough surface to which an 1/R curve was fitted.
Again care was taken with the hydrophone orientation when carrying
out scattering and normalisation measurements. No measurements were
made to investigate the effect of placing the LC5-2 hydrophone on
the acoustic axis. The separation between the transducer and the
rough surface was 164 cm and the distance of the hydrophone from the
rough surface varied from 12 to 130 cm.

The variation of normalised intensity with the range from the surface is shown in figure 17b. The scattered intensity can be seen to steadily reduce with range. A nominal estimate for the error is again ± 2 db.

The solid line is the computed axial intensity obtained from equation 5-13. The predicted values for the intensity compare favourably with the measured values, although there is again a tendency to over estimate the intensity.

5.10 Summary Of The Comparison Between The Predicted And Measured Intensities

The best agreement between the computed and measured backscattered normal incidence normalised intensity occurred using the Fresnel phase approximation to calculate both the coherent and incoherent components of the scattered intensity. Notwithstanding the comments made upon particular comparisons between the data and computed values, in most cases reasonable agreement was obtained over the whole frequency range. There was a reduction in intensity at the low frequency which approximately followed an exp(-g) form. The rate of decrease of the intensity in the intermediate frequency band, where both the coherent and incoherent components of intensity contribute to the scattered intensity, were predicted with very similar rates to those observed. At the higher frequencies, the measured values

do appear to be explicitly independent of frequency as predicted. The changes at the high frequencies are considered to be predominantly introduced because of the area of insonification changing and not due to an a priori frequency dependence.

The discrepancy between the measured and calculated values are not necessarily the inadequacy of the theory. The predicted values were calculated on the assumption that the surface statistics were exactly Gaussian. The measurements described in chapter 3 showed that the surface could not be rejected as having Gaussian statistics and were likely to be approximately Gaussian. Therefore part of the discrepancy is almost certainly due to the departure from Gaussian of the surface statistics.

Chapter 6   Discussion, Further Work, And Conclusions

6.1   Discussion

A certain amount of discussion has already been introduced throughout the text in the analysis of the measurements presented. In this section a brief summary of the Thesis is given, the developments of Chapter 2 are compared with other experimental data, and the use of the measured frequency response to obtain information about the scattering surface is considered.

6.1.1   Review

The principal objective at the outset of this study was to investigate the frequency dependence of the normal   incidence back-scattered intensity, from a rough surface of known statistics, at a number of transmitter and receiver distances. These observations were to be compared with a theoretical model which could predict the scattered intensity.

This work was considered of value because the majority of lab-oratory experiments on scattering had concentrated on the angular distribution of the scattered intensity at larger distances from the scattering surface than those used here. Further more, recent field studies, Cochrane and Dunsiger(45) for example, have been particularly orientated towards broadband investigations of rough surface scattering to obtain surface information.

Basic to the whole of this investigation was the rough surface model. The construction of the surface presented many problems,

however, moderate success was achieved with the final version which was produced by a process of sculpting, and judgement by eye. The surface statistics resembled those of a Gaussian distribution, and had surface parameters of root-mean-square height, autocorrelation length, and slope, consistent with the design requirements. The material used for construction was a rigid foam with a high value for the acoustic attenuation and reflection coefficient in water.

For the model rough surface a frequency range of 20-300 kHz was required to obtain measurements of the backscattered intensity at normal incidence, which had a large variation in the degree of phase coherency between the transmitted and the scattered signal. A parametric source was utilised to obtain the necessary bandwidth and directivity. This in itself required the development of specialised equipment, and an experimental investigation to obtain a working understanding of the nearfield parametric array. Although the wave-front deviated from sphericity as a consequence of working close to the parametric array, measurements showed the wavefront to be spherical near the acoustic axis, and in general the demands on the source were fulfilled by the array.

The values of the backscattered intensity presented in Chapter 5 were taken over nearly a year, and on one or two graphs where further measurements were added to the preliminary data observations were taken over a period spanning three months. The results of the measurements made show that a high degree of repeatability was obtained, as can be seen in the previous chapter.

The theoretical comparisons made with the backscattered data used the Helmholtz-Kirchhoff Integral. Many theoretical works adopt this approach as has been outlined in Chapters 1 and 2. The developments carried out in this work applied the analysis of Clay and Medwin (11) to a Gaussian surface. This yielded results which were consistent with the experimentally validified image solution for a plane surface, and predicted incoherent intensity levels lower in magnitude, particularly for low values of roughness parameter, than calculated on the basis of a linear phase approximation. The solution obtained in equation 2-47 applies for any frequency and incidence angle, and the predicted intensities are readily computed. However, it must be noted that grazing angles are represented inadequately.

The three computed curves calculated using equations 5-7, 5-8 and 5-9 show differing degrees of agreement with the experimental measurements. However, the closest agreement with the observed data was usually obtained when comparing the predictions based on the second order phase approximation. In the region of moderate roughness, between roughness parameter values of 1 and 20, the neglection of s, the extra term introduced by retaining higher order phase terms, yield predicted values for the scattered intensity which were overestimated. The inclusion of s reduced the calculated values for the backscattered signal level in this moderate roughness range and gave improved agreement with the experimental data.

## 6.1.2 Estimation of the surface roughness from the scattered intensity

From the difference frequency scattering experiments, the root-mean-square value for both the height and slope of the rough surface were estimated. A fit was obtained with the measured data by simply comparing by eye a series of calculated intensities for different values of height and slope. The results for the series of experiments where the transducer was at 100 cm from the surface are shown in figure 1.

For hydrophone position of 70, 50, 30 and 20 cm from the surface, the estimated root-mean-square heights were 2.2, 2.0, 1.5 and 1.5 mm respectively and the root-mean-square slopes were 0.21, 0.19, 0.16 and 0.21 respectively. These values are similar to those of 2.2 and 0.16 measured for the surface root-mean-square height and slope.

Although this demonstrates that reasonably accurate estimates of some surface parameters can be extracted from the frequency response of the scattered intensity, assumptions about the statistical distribution and reflection coefficient of the surface were needed. For an unknown surface a similar force of fit between the measured and predicted intensities could be made to estimate surface parameters and predict the scattered intensity under a different configuration. However, the assumptions made about the surface introduce uncertainties which could lead to poor estimates being obtained.

6.1.3 Comparison of the theoretical predictions with other experimental results

As mentioned above, the theoretical results developed agreed quite well with the experiments reported in this Thesis. It was
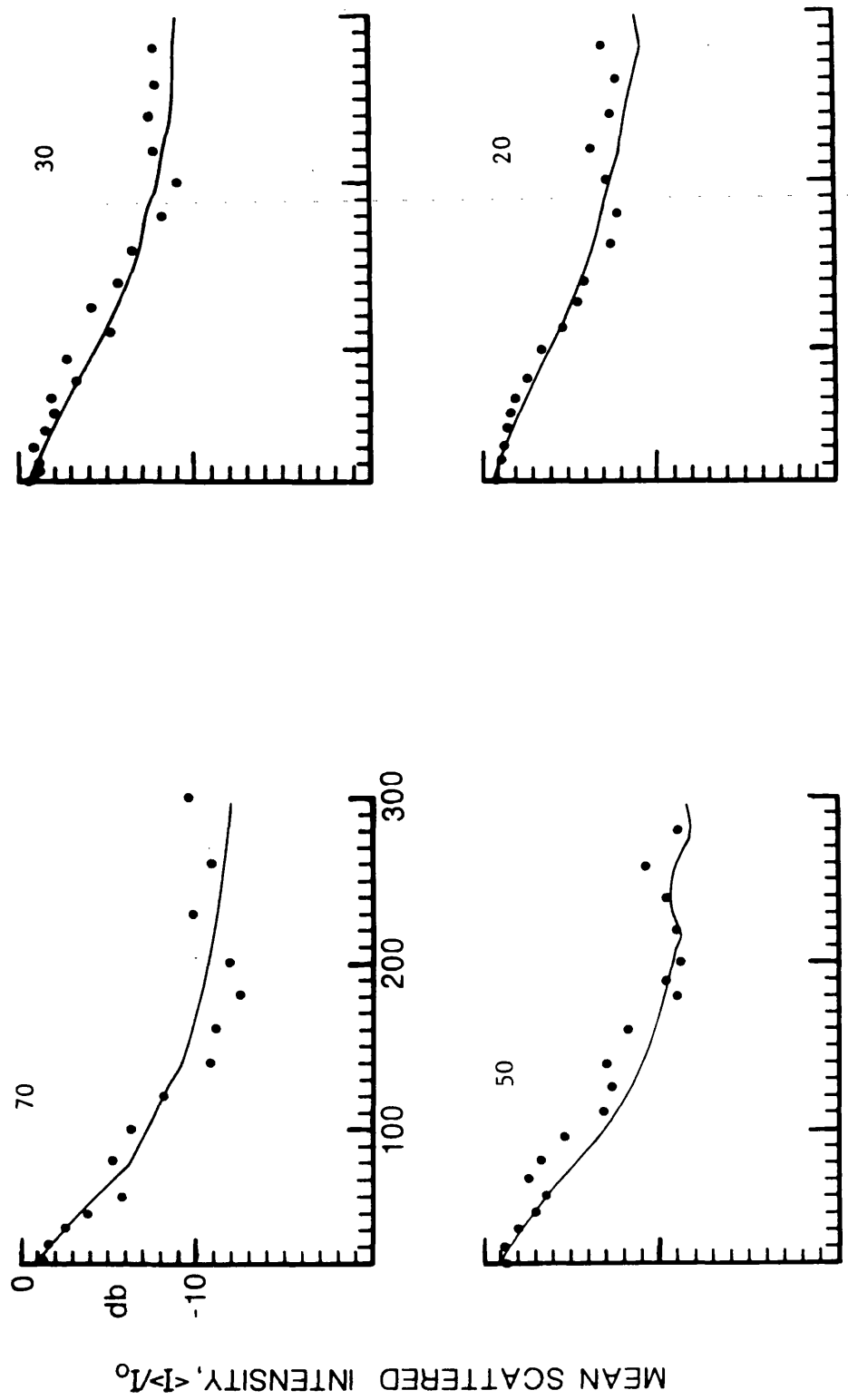
Fig 1   Estimation of surface parameters at four hydrophone distances from rough surface by fitting curves to the measured data. ● Measured. — Fitted curve using equation 2-49.

therefore considered that a comparison with other published
experimental data would also be of interest.

A comprehensive experimental investigation into the angular
distribution of the scattered intensity has been presented in
reference (22), and the data on the specularly scattered intensity is
compared here with predicted values calculated using equation 2-47.

Details of the surfaces used and further comparisons are
presented in Appendix 5, with a brief resume being given here.   In
figure 2 a series of measurements are shown for the specularly
scattered normalised intensity, for four surfaces with root-mean-square
heights h and autocorrelation lengths T, for an insonifying radiation of
220 kHz. Two curves are compared with the measured values which are
indicated by the dotted line. The first of these is the broken line
which was computed using the second order phase solution of equation
2-47, and the second is the solid line calculated using the same
expression but with s set equal to zero which is the result of using a
linear phase approach. Better agreement between the calculated and
measured intensities is obtained with the broken line. This is
consistent with the comparisons made in the previous chapter.

6.2   Suggestions For Further Work

There is an enormous amount of literature published on the subject
of scattering from rough surfaces, as illustrated by the bibliography,
which is by no means exhaustive, given in a recent monograph on the
subject by Bass and Fuks (46). Therefore it is acknowledged in making
suggestions for further work that similar interests may have been
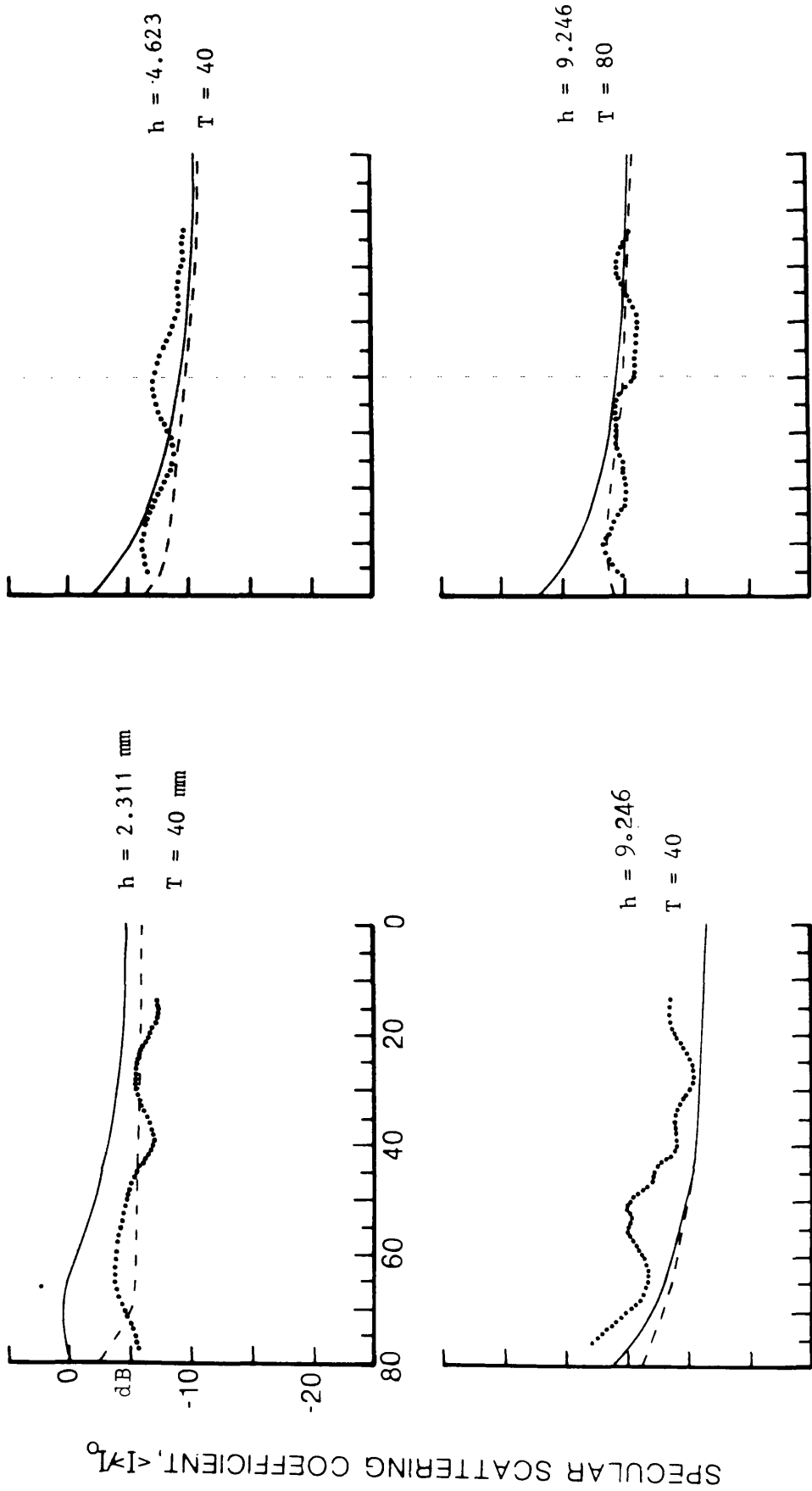
Fig 2 Predicted curves taken from equation 2-47 compared with measured values from reference (22). ● Measured, — equation 2-47 with s = 0, and ----- 2-47 with values for s used. Insonifying frequency 220 kHz.

considered in other areas of scattering.

Although many constructed rough surface models have been used to investigate the phenomenon of scattering, in almost all cases the surface statistics have deviated from the ideal case used in the mathematical analysis. Therefore a series of surfaces with statistics accurately modelled by analytical functions that could be manipulated in the scattering integral,would be valuable in allowing a variety of experiments to be conducted.These could be used to examine closely the limitations of the Helmholtz-Kirchhoff method and other theoretical approaches.

The majority of laboratory scattering investigations have principally been concerned with long pulse measurements at the resonant frequency of a narrow band transducer. However, the application of broadband transducers or the utilisation of the transient parametric array offers the opportunity of using broadband pulse techniques to rapidly analyse a rough surface. Experiments using this approach in parallel with the programme outlined in the previous paragraph could yield valuable results. Some progress has been made in this direction and is reported in reference (32).

The application of acoustic techniques under controlled conditions to distinguish between surface sediments has engaged a great deal of interest; a review of the subject is given by Pace (47). However, accurate measurments of the frequency and angular response of the intensity scattered from sediment surfaces, to acoustically estimated surface features, which have been independently measured, is a necessary area for further research. Studies by Pace (48) (49), Williams (50) and Gurcan, Creasey and Gazey (51) illustrate approaches

which have been adopted to solve this problem, however these are still experimental investigations and there is wide scope for innovation.

Although the above suggestions are concerned with laboratory studies, it should be briefly mentioned here that the consideration of the effects of scattering when analysing sidescan sonar, echo sounding, and subbottom profile records are areas of research being pursued and where further developments are required.

6.3 Conclusions

A theoretical and experimental study has been conducted into the backscattered intensity, at normal incidence, from a model rough surface over a wide band of frequencies and at different distances from the scattering surface. Predicted results based on the theory developed compare well with the experimental data obtained as well as with other published results.

Finally although this Thesis has been principally concerned with the subject of scattering it has also yielded an interesting investigation into the nearfield parametric array, and some of the problems which can arise in its application.

Appendix 1   Simplification Of The Scattering Integral
_____

The integral in equation 2-28 of chapter 2 is simplified in this

Appendix.   Starting with equation 2-28 we have

$$\Gamma_1 = \int\int\int\int_{-\infty}^{\infty} DD'\exp\{(\imath k[(x-x')\alpha + (y-y')\beta + U_x(x^2 - x'^2) + U_y(y^2 - y'^2)])\}$$

$$(<\exp(\imath k\gamma[\zeta - \zeta'])> - <\exp(\imath k\gamma\zeta)><\exp(-\imath k\gamma\zeta')>)$$

$$dxdx'dydy' \qquad\qquad\qquad\qquad A1\text{-}1$$

where

$$D = \exp-[(x^2/X^2) + (y^2/Y^2)] \qquad\qquad A1\text{-}2$$

Introducing variables

$$x = x'' + \epsilon/2 \qquad y = y'' + \eta/2 \qquad A1\text{-}3a$$

$$x' = x'' - \epsilon/2 \qquad y' = y'' - \eta/2 \qquad A1\text{-}3b$$

This gives

$$x - x' = \epsilon \qquad\qquad y - y' = \eta$$

$$x^2 - x'^2 = (x^{2\,\prime\prime} + \epsilon x'' + \epsilon^2/4) - (x^{2\,\prime\prime} - \epsilon x'' + \epsilon^2/4) = 2\epsilon x'' \qquad\qquad A1\text{-}4$$

$$y^2 - y^{2\,\prime} = 2\eta\,y''$$

$$x^2 + x'^2 = 2x^{2\,\prime\prime} + \epsilon^2/2$$

$$y^2 + y'^2 = 2y^{\,\prime\prime 2} + \eta^2/2$$

Also utilising the standard relationship for a change of variables where

$$x = x(u, v) \qquad\qquad y = y(u, v) \qquad\qquad A1\text{-}5$$

then

$$\iint\limits_{XY} f(x, y)\,dxdy = \iint\limits_{UV} f(x(u,v),\ y(u,v)) \left| \frac{\partial(x, y)}{\partial(u, v)} \right| dudv \qquad\qquad A1\text{-}6$$

where

$$\frac{\partial(x, y)}{\partial(u, v)} \quad \text{is the Jacobian transform given by}$$

$$\frac{\partial(x, y)}{\partial(u, v)} = \frac{\partial x}{\partial u} \cdot \frac{\partial y}{\partial v} - \frac{\partial x}{\partial v} \cdot \frac{\partial y}{\partial u}$$

Which for equation A1-3a and A1-3b has a value of unity. Using A1-2 to A1-6 allow A1-1 to be written as

$$\Gamma_1 = \int\int\int\int_{-\infty}^{\infty} \exp\left(-\left[\frac{1}{X^2}\left(2x^{2''} + \frac{\varepsilon^2}{2}\right) - \frac{1}{Y^2}\left(2y^{2''} + \frac{\eta^2}{2}\right)\right]\right) \exp(\imath k[\alpha\varepsilon + \beta\eta])$$

$$\exp(\imath k[2U_x\varepsilon x'' + 2U_y\eta y'']) (\langle\exp(\imath k\gamma[\zeta - \zeta'])\rangle$$

$$- \langle\exp(\imath k\gamma\zeta)\rangle\langle\exp(-\imath k\gamma\zeta')\rangle$$

$$dx'' \, dy'' \, d\varepsilon \, d\eta \qquad\qquad\qquad \text{A1-7}$$

Rearranging gives

$$\Gamma_1 = \int\int\int\int_{-\infty}^{\infty} \exp\left(-\left[\frac{2x^{2''}}{X^2} - 2\imath k \, U_x\varepsilon x''\right]\right)\exp\left(-\left[\frac{2y^{2''}}{Y^2} - 2\imath k U_y\eta y''\right]\right)$$

$$\exp(\imath k[\alpha\varepsilon + \beta\eta]) \exp\left(-\left[\frac{\varepsilon^2}{2X^2} + \frac{\eta^2}{2Y^2}\right]\right) (\langle\exp(\imath k\gamma[\zeta - \zeta'])\rangle$$

$$-\langle\exp(\imath k\gamma\zeta)\rangle\langle\exp(-\imath k\gamma\zeta')\rangle) \, dx''dy''d\varepsilon d\eta \qquad\qquad \text{A1-8}$$

Now by completing the square gives

$$(\frac{\sqrt{2}\,x''}{X} - \frac{ik\,U_x\epsilon X}{\sqrt{2}}\,)^2 + \frac{k^2 U\epsilon^2 X^2}{2}x^2 = \frac{2x''^2}{X^2} - 2ikU_x\epsilon\,x''$$

A1-9

Using A1-9 and a similar expression for the equivalent y'', η'' in A1-8 gives

$$\Gamma_1 = \int\int\int\int_{-\infty}^{\infty} \exp\left(-[\frac{\sqrt{2}x''}{X} - \frac{ik\,U_x\epsilon X}{\sqrt{2}}]^2\right)\exp\left(-[\frac{\sqrt{2}y''}{Y} - \frac{ikU_y\eta Y}{\sqrt{2}}]^2\right)$$

$$\exp\left(\frac{-\epsilon^2}{2}[\frac{1}{X^2} + k^2 U_x^2\,X^2]\right)\exp\left(-\frac{\eta^2}{2}[\frac{1}{Y^2} + k^2 U_y^2\,Y^2]\right)$$

$$\exp(ik[\alpha\epsilon + \beta\eta])(\langle\exp(ik\gamma[\zeta - \zeta'])\rangle - \langle\exp(ik\gamma\zeta)\rangle\langle\exp(-ik\gamma\zeta')\rangle)$$

$$d\,x''dy''\,d\epsilon d\eta$$

A1-10

The integral over x'' and y'' can now be carried out. Concentrating on x'', and letting

$$p = \frac{\sqrt{2}\,x''}{X} - \frac{ik\,U_x\epsilon X}{\sqrt{2}}$$

A1-11

$$dp = \frac{\sqrt{2}}{X}\,dx''$$

A1-12

and using the identity

$$\frac{X}{\sqrt{2}} \int_{-\infty}^{\infty} \exp(-p^2)\, dp = \sqrt{\pi}.\frac{X}{\sqrt{2}} \qquad\qquad\text{A1-13}$$

allow the integral over x" and y" to be evaluated, giving

$$\Gamma_1 = \frac{\pi XY}{2} \int_{-\infty}^{\infty}\!\!\int \exp\left(-\frac{\varepsilon^2}{2}\left[\frac{1}{X^2} + k^2 U_x^2 X^2\right]\right)\ \exp\left(-\frac{\eta^2}{2}\left[\frac{1}{Y^2} + k^2 U_y^2 Y^2\right]\right)$$

$$(\exp(\imath k[\alpha\varepsilon + \beta\eta])(\langle\exp(\imath k\gamma[\zeta - \zeta'])\rangle$$

$$- \langle\exp(\imath k\gamma\zeta)\rangle\langle\exp(-\imath k\gamma\zeta')\rangle\rangle)d\varepsilon d\eta \qquad\qquad\text{A1-14}$$

To simplify equation A1-14 approximations need to be made in the coefficients of the second order terms in the exponentials. The values used, correspond to the case of normal incidence back-scattering, which is the experimental arrangement for this case. Using these first order approximations on the second order coefficients yields

$$\frac{1}{X^2} + k^2 U_x^2 X^2 \approx \frac{1}{Y^2} + k^2 U_y^2 Y^2 \approx \frac{1}{W^2} + k^2 R_s^2 W^2 \qquad\qquad\text{A1-15}$$

where

$$R_s = \tfrac{1}{2}(R_0^{-1} + R_1^{-1}) \qquad\qquad\text{A1-16}$$

and

$$W = (X_0 + Y_0)/2 \qquad\qquad A1-17$$

The term s is introduced, and is given by

$$2s = \frac{1}{W^2} + k^2 R_s^2 W^2 = \frac{1}{W^2} + \frac{g R_s^2 W^2}{h^2 \gamma^2} \qquad\qquad A1-18$$

This allows equation A1-14 to be symmetrised and written as,

$$\Gamma_1 = \frac{\pi XY}{2} \int_{-\infty}^{\infty}\!\!\int \exp(-[\varepsilon^2 + \eta^2]s)\, \exp(\imath k[\alpha\varepsilon + \beta\eta])\, (\langle\exp(\imath k\gamma[\zeta - \zeta'])\rangle$$

$$- \langle\exp(\imath k\gamma\zeta)\rangle\langle\exp(-\imath k\gamma\zeta')\rangle)\, d\varepsilon d\eta \qquad\qquad A1-19$$

Equation A1-19 is used in chapter 2 to obtain a solution for the incoherent intensity. As s→o the integral in equation A1-19 becomes identical to that derived using a linear phase approximation.

Appendix 2   Profiles Of The Model Rough Surface

A2.1 Surface Sections

Two orthogonal sets of surface profiles were measured. These sections were labelled A0 to A9 and B0 to B8 and are shown in figures 1, 2, 3 and 4. Height measurements were made at 1.0 mm intervals along the 480 mm sections. The profiles were digitised at 2 mm spacings at height intervals of 0.2 mm. This digitisation interval yielded profiles which accurately represented the continuous height variation across the surface sections.

The surface profiles show the model rough surface to be a gently undulating surface with small slopes. The height varies in a random manner about the section mean with maximum excursions of approximately 1 cm. The form of the profiles are basically consistent in character and no qualitative significant differences are observed between the two sets of measurements at right angles to one another.

Some low frequency trends can be identified in addition to the general surface roughness. For example in B0 and B1 there is an overall reduction in height moving from the beginning of the profile to the end. Allowances are made for these trends in this Appendix and in Chapter 3.

A2.2 Comparison Of The Section Heights With A Gaussian Distribution

To fit a Gaussian curve to the measured data the mean and stand-ard deviation of the sections were calculated. Using these values a

Gaussian curve was computed using

$$f(h) = \frac{Nw}{\sigma\sqrt{2\pi}} \exp(-[h-\bar{h}]^2/2\sigma^2)$$ A1-2

where σ, $\bar{h}$ and h are the standard deviation, mean height, and particular profile height respectively. N is the number of observations, and w is the class width used in the histograms of the measured values.

Figures 5, 6, 7, 8 and 9 show the calculated Gaussian curves with the measured histograms. The abscissa represents the surface elevation and the ordinate is the frequency of the height distribution. For the majority of cases the qualitative agreement between the histograms and calculated curves are reasonable. Some bimodal and skewness tendencies are seen in some of the sections, however, the essential features of the height distributions appear to be approximately Gaussian. A comparison of the total distribution for the surface, calculated using areas rather than sections to suppress low frequency trends, is given in Figure 10. This compares well with a Gaussian distribution of the same mean and standard deviation as the measured distribution.

A2.3 Comparison Of The Measured Autocorrelation Functions With Gaussian Autocorrelation Functions

Firstly the mean height of each section was removed and the normalised autocorrelation function was calculated using

$$C[L] = \frac{1}{N} \left[\sum_{i=0}^{N-|L|-1} x_i x_{i+|L|} \right] /C[0] \qquad L = 0, \pm 1, \pm 2, \ldots\overline{+}N-1 \qquad A2-2$$

N is the total number of points in the sample section, that is 240, $C[0]$ is the variance of the section, x_i and $x_i + |L|$ are the displacement of the ith and $i + |L|^{th}$ terms in the section, and L is the lag position. If the number of samples N is large compared to the lag L then the sample autocorrelation function is a good estimate of the true autocorrelation function, therefore L is limited to a maximum value of $0.1N$.

Using the measured autocorrelation functions two mean surface autocorrelation functions were calculated. The first was obtained by averaging the values of $C[L]$, calculated from equation A2-2, at each lag position, giving

$$\overline{C[L]}_1 = \frac{1}{N'} \sum_{n=1}^{N'} C_n[L] \qquad \text{A2-3}$$

where $N' = 19$. The second method was to average the non-normalised autocorrelation functions, and then normalise these values by the mean zero lag value, this is given by

$$\overline{C[L]}_2 = \frac{1}{N'}[\sum_{n=1}^{N'} C[0]_n \ C[L]_n]/\overline{C[0]} \qquad \text{A2-4}$$

$$\overline{C[0]} = \frac{1}{N'} \sum_{n=1}^{N'} C[0]_n \qquad \text{A2-5}$$

Correlograms for $C[L]_1$ and $C[L]_2$ are shown in figure 11 . The values

for $C[L]_1$ and $C[L]_2$ are very similar, and within one standard

error of one another. The standard error was calculated from the

variance in the values of the sample section autocorrelation functions

for a particular lag.

The values for the mean normalised autocorrelation functions,

given in figure 11 show steadily decreasing values, with a reduction

in the gradient of the curves as the lag increases. For large lag

values the magnitude of the autocorrelation functions level out at

a value of approximately 0.2. This reduction in decrease of the

autocorrelation function arises in part due to the low frequency trends

previously mentioned having a particularly strong influence upon the

autocorrelation function of some of the sections. For example

inspection of section BO in figure 2 shows the surface roughness to

be superimposed upon a linear trend, which results in the autocorrelation

function for the section reducing less rapidly than would have occurred

if only small scale roughness had been present. This effect increases

the value of the mean autocorrelation function for the larger lag

positions.

A Gaussian autocorrelation function of the form

$$C[r] = \exp(-r^2/T^2) \qquad\qquad \text{A2-6}$$

Where T is the autocorrelation length,was compared with the experi-

mental data, this is shown as the solid line in figure 11. Because

of the influence the surface low frequency trends had on the auto-

correlation function the value of T chosen was one which gave good

agreement between the experimental and Gaussian autocorrelation func-

tions above the half value level of the measured mean normalised

autocorrelation functions. This gave an autocorrelation length of

$$T = 19 \pm 2 \text{ mm}$$

Gaussian autocorrelation functions were also fitted to each

of the surface profiles. Again the value of T chosen was one which

gave a good fit for $C(r) > 0.5$. Correlograms showing the measured

and Gaussian curves are in figures 12, 13, 14, 15 and 16, where for

the majority of cases the measured autocorrelation function is approxi-

mately Gaussian. For the sections A4 and B0 the curves were fitted

particularly close to the axis because the autocorrelation functions

of the profiles appeared to have been most notably influenced by the

low frequency trends on the surface.

In conclusion this qualitative analysis shows the measured and

compared Gaussian statistic to be similar. Further quantitative

calculations are presented in Chapter 3.
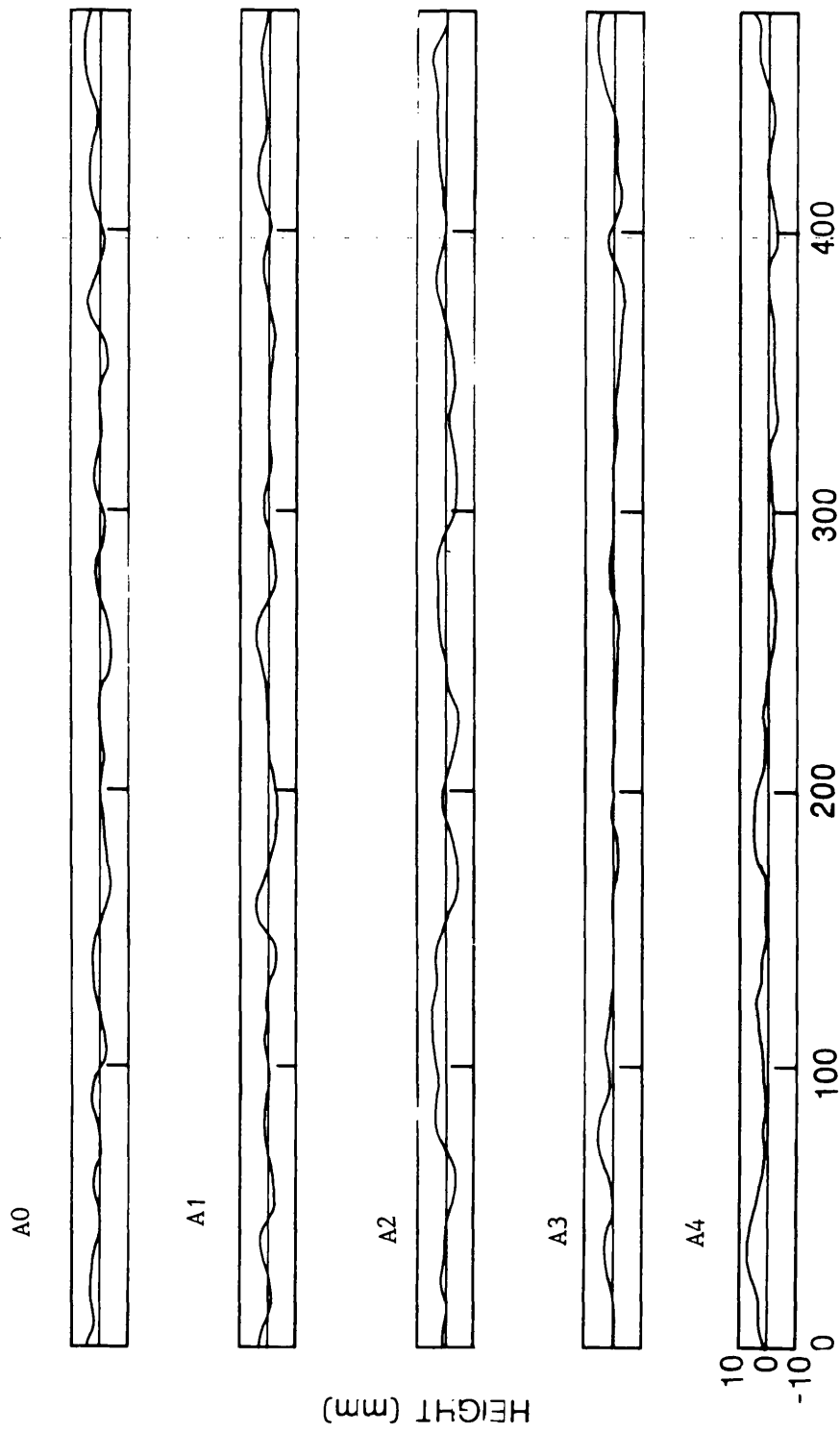
DISTANCE ACROSS THE SURFACE SECTION (mm)

Fig 1   Profiles of the surface sections.

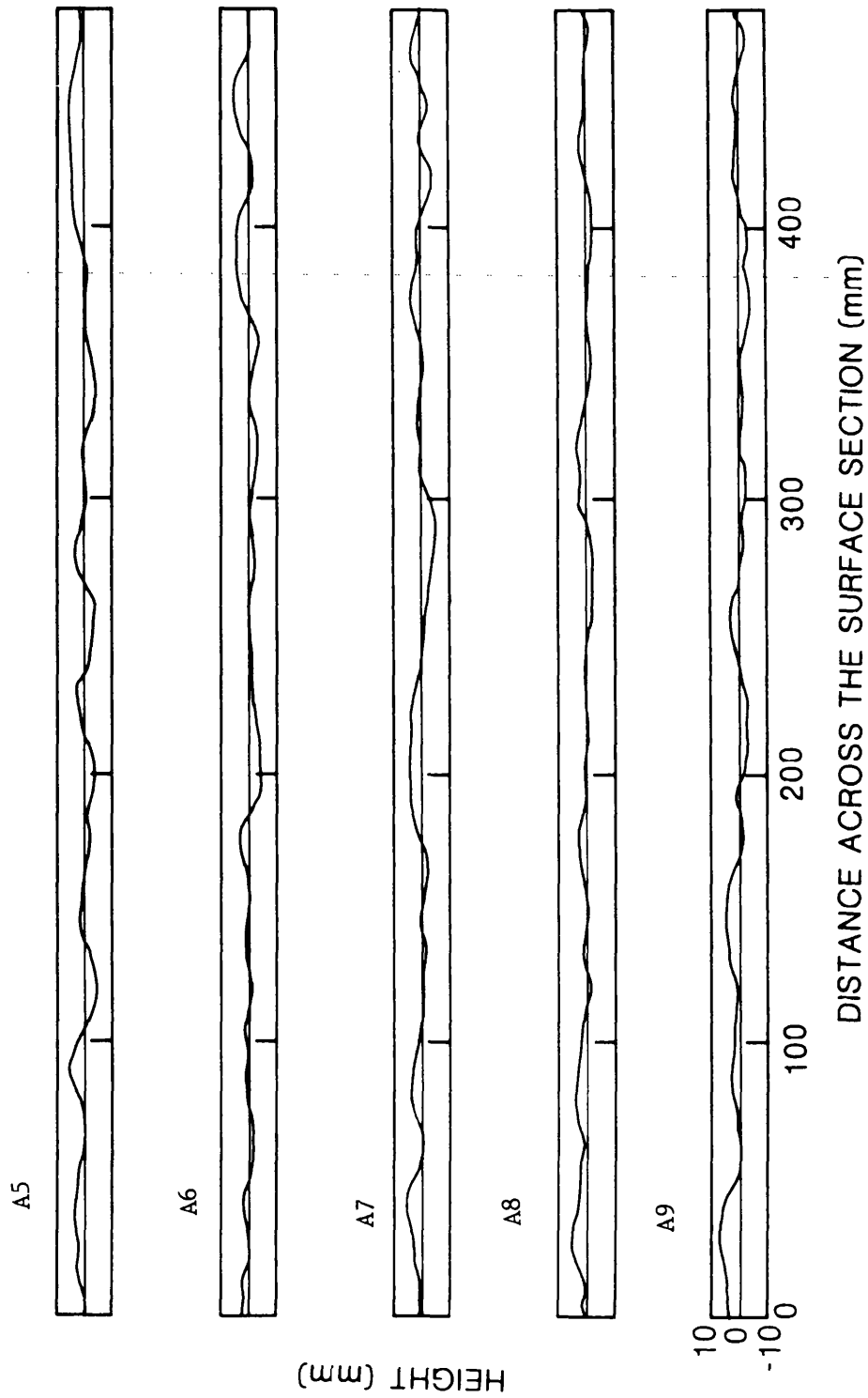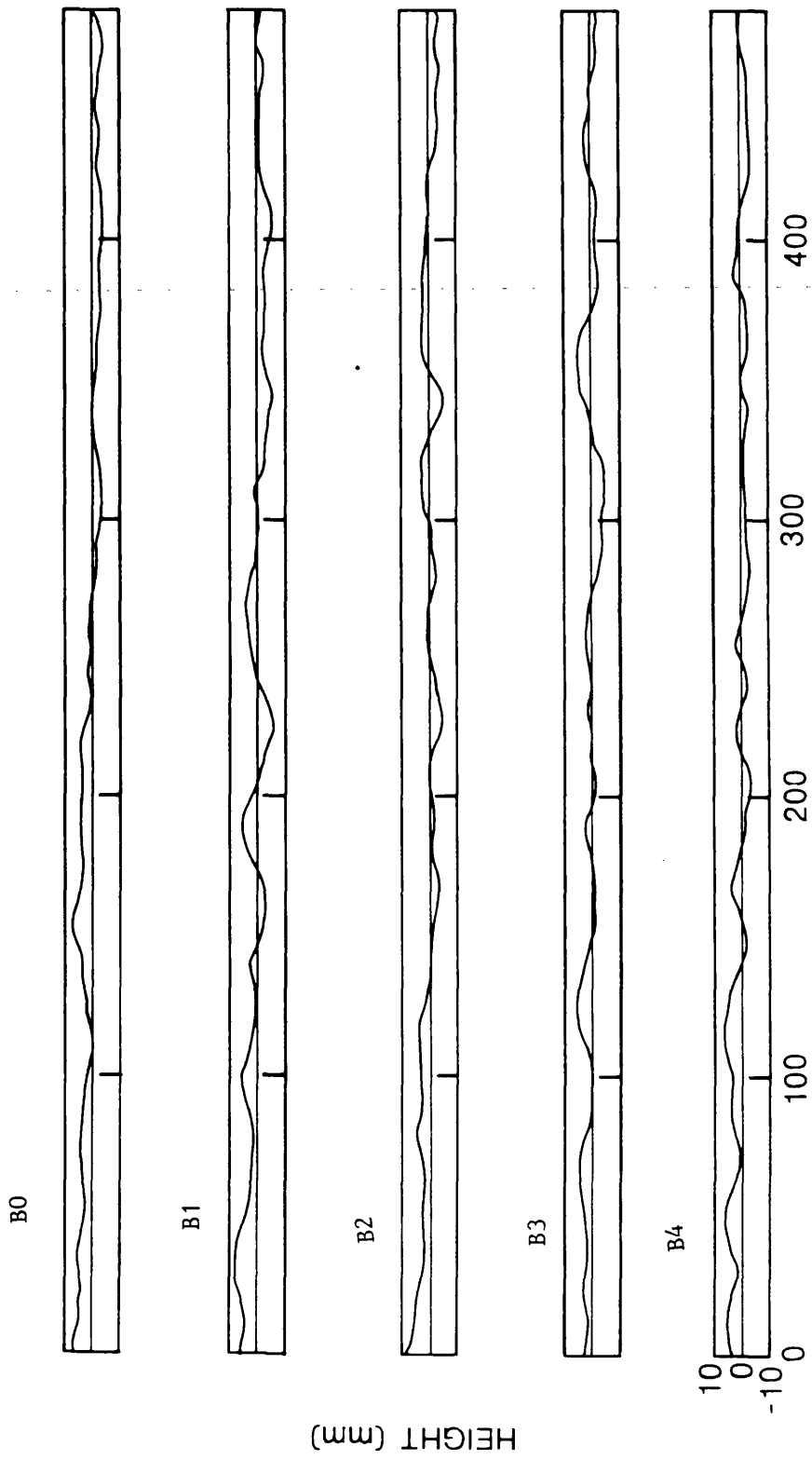DISTANCE ACROSS THE SURFACE SECTION (mm)

HEIGHT (mm)

Fig 2   Profiles of the surface sections.

DISTANCE ACROSS THE SURFACE SECTION (mm)

Fig 3   Profiles of the surface sections.

Fig 4   Profiles of the surface sections.

DISTANCE ACROSS THE SURFACE SECTION (mm)

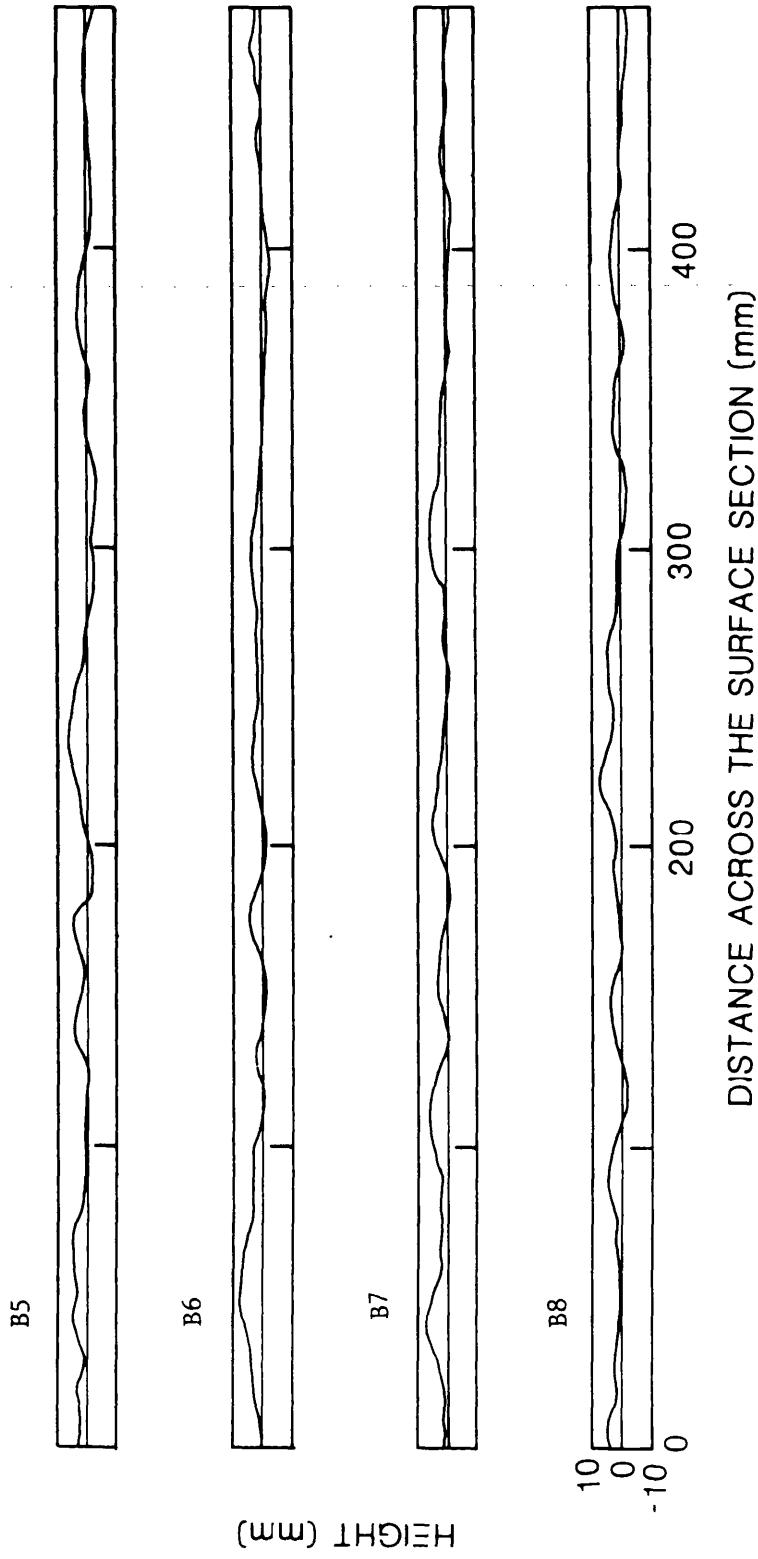HEIGHT (mm)

B5
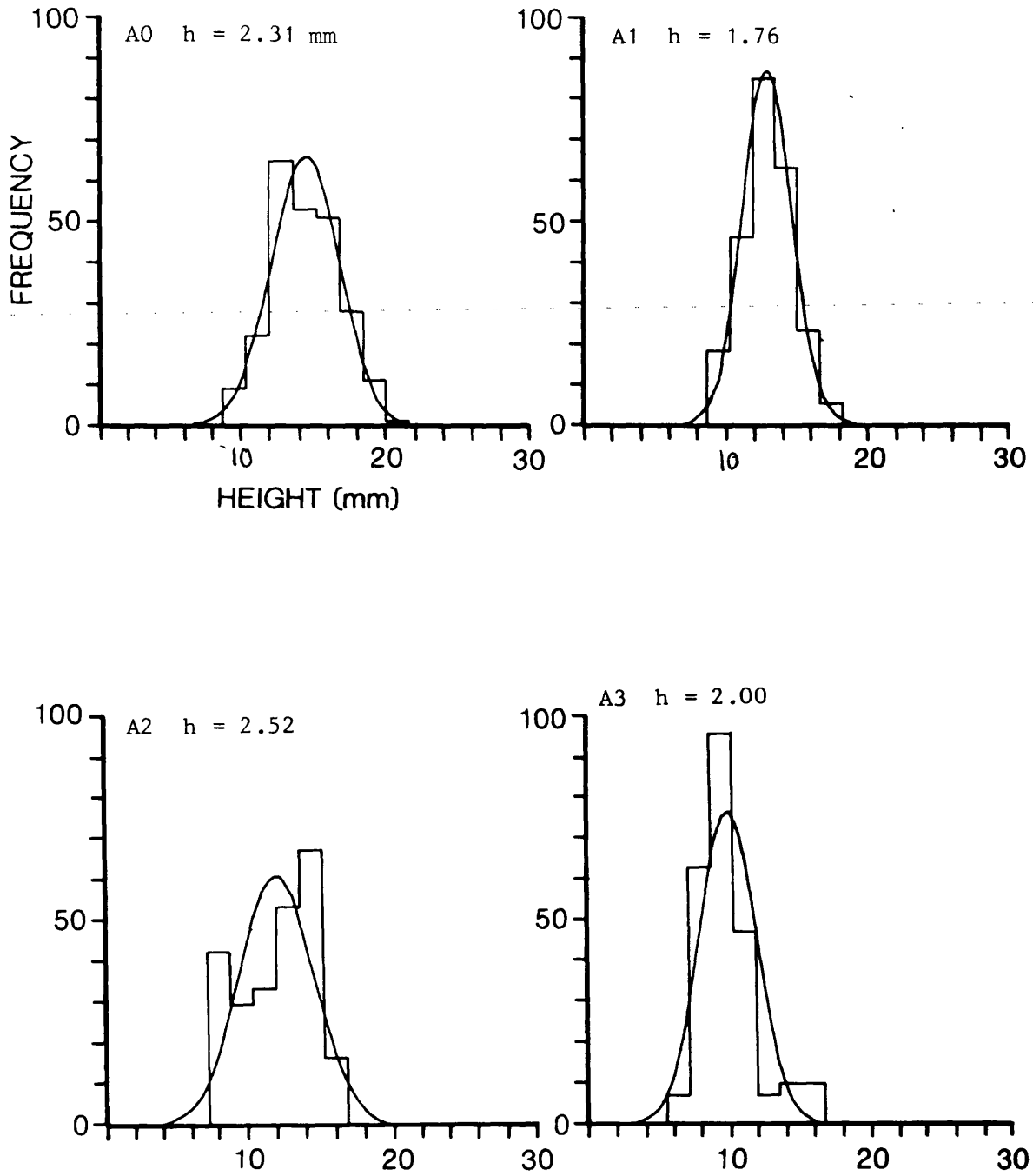
B6

B7

B8

0   200   300   400

10
0
-10

Fig 5   Histograms of the measured height distributions compared

with   Gaussian distributions of the same mean and
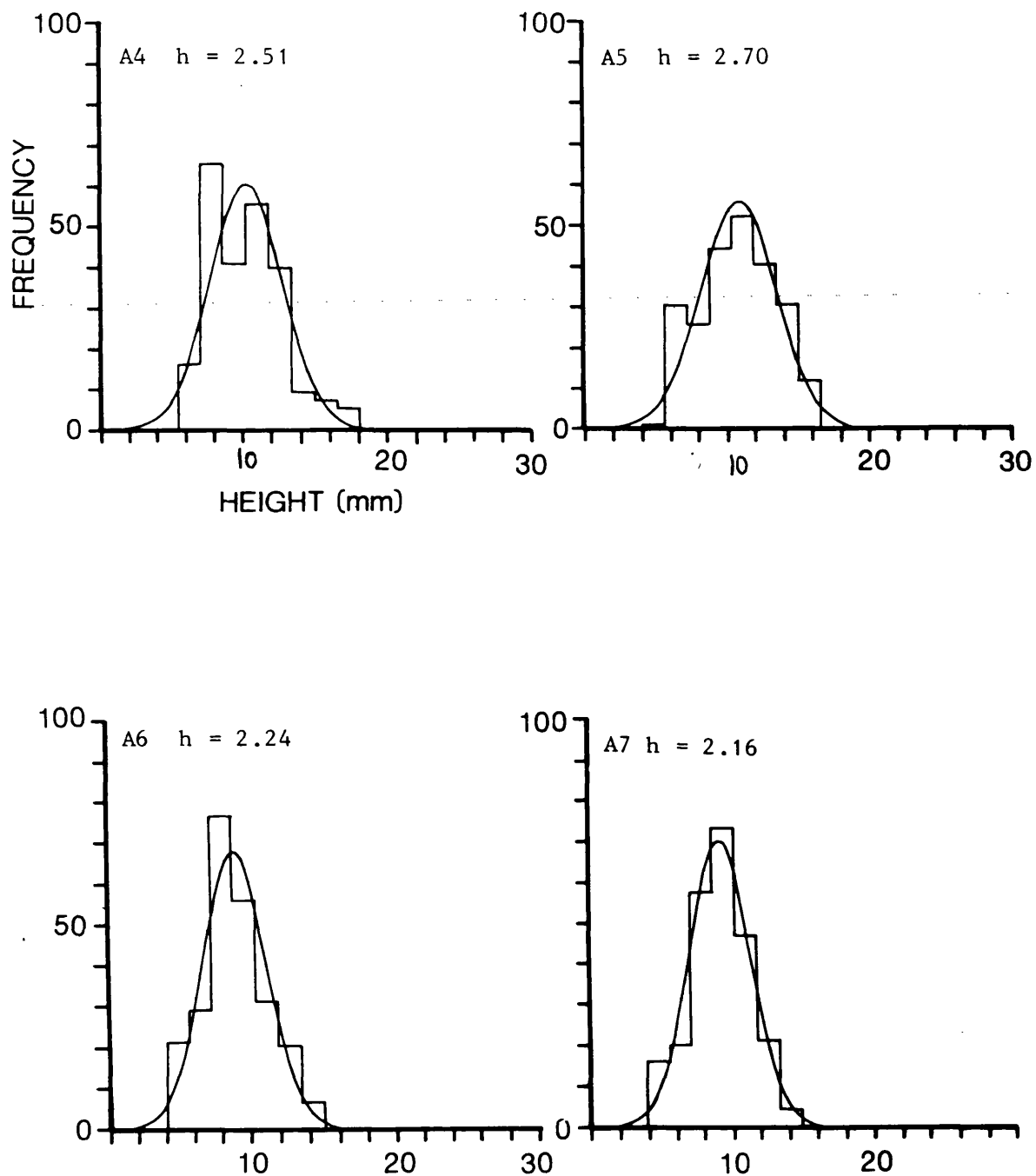
standard deviation h.

Fig 6   Histograms of the measured height distributions compared
         with   Gaussian distributions of the same mean and
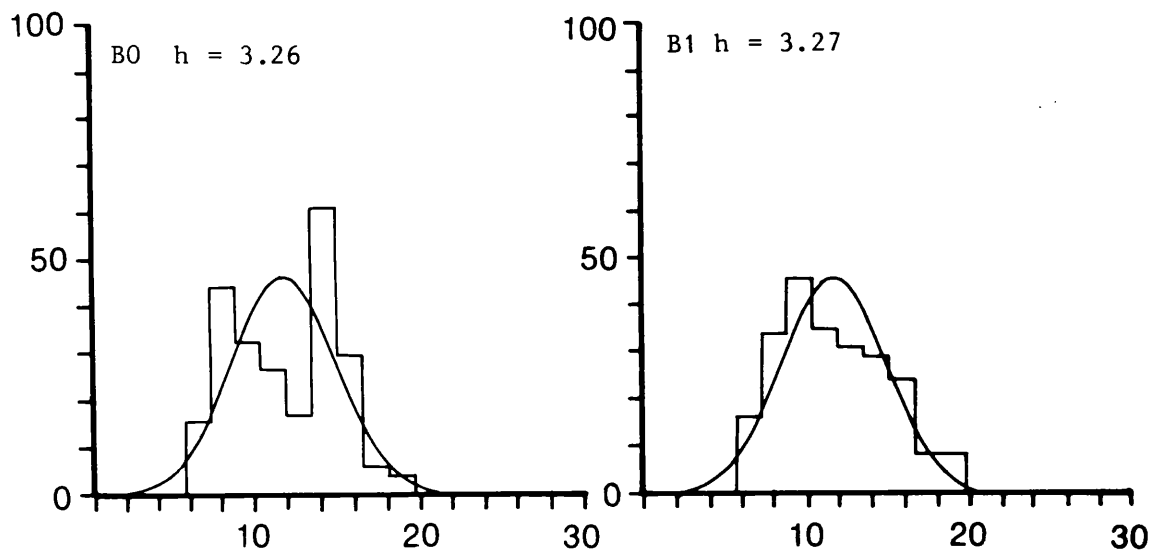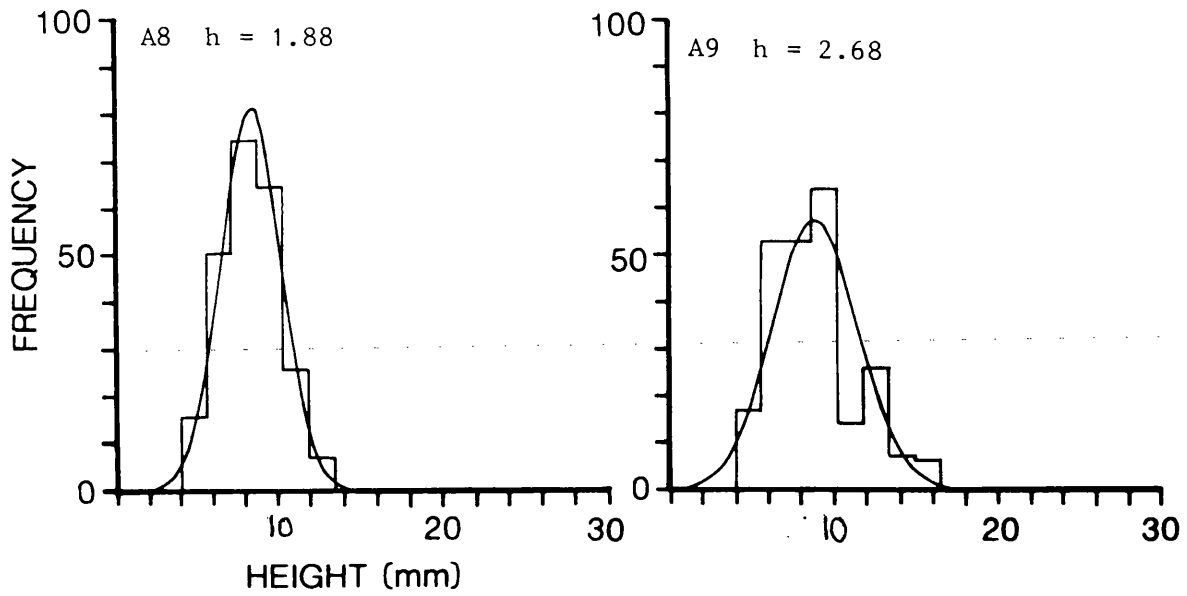   standard deviation h.

Fig 7   Histograms of the measured height distributions compared

with   Gaussian distributions of the same mean and
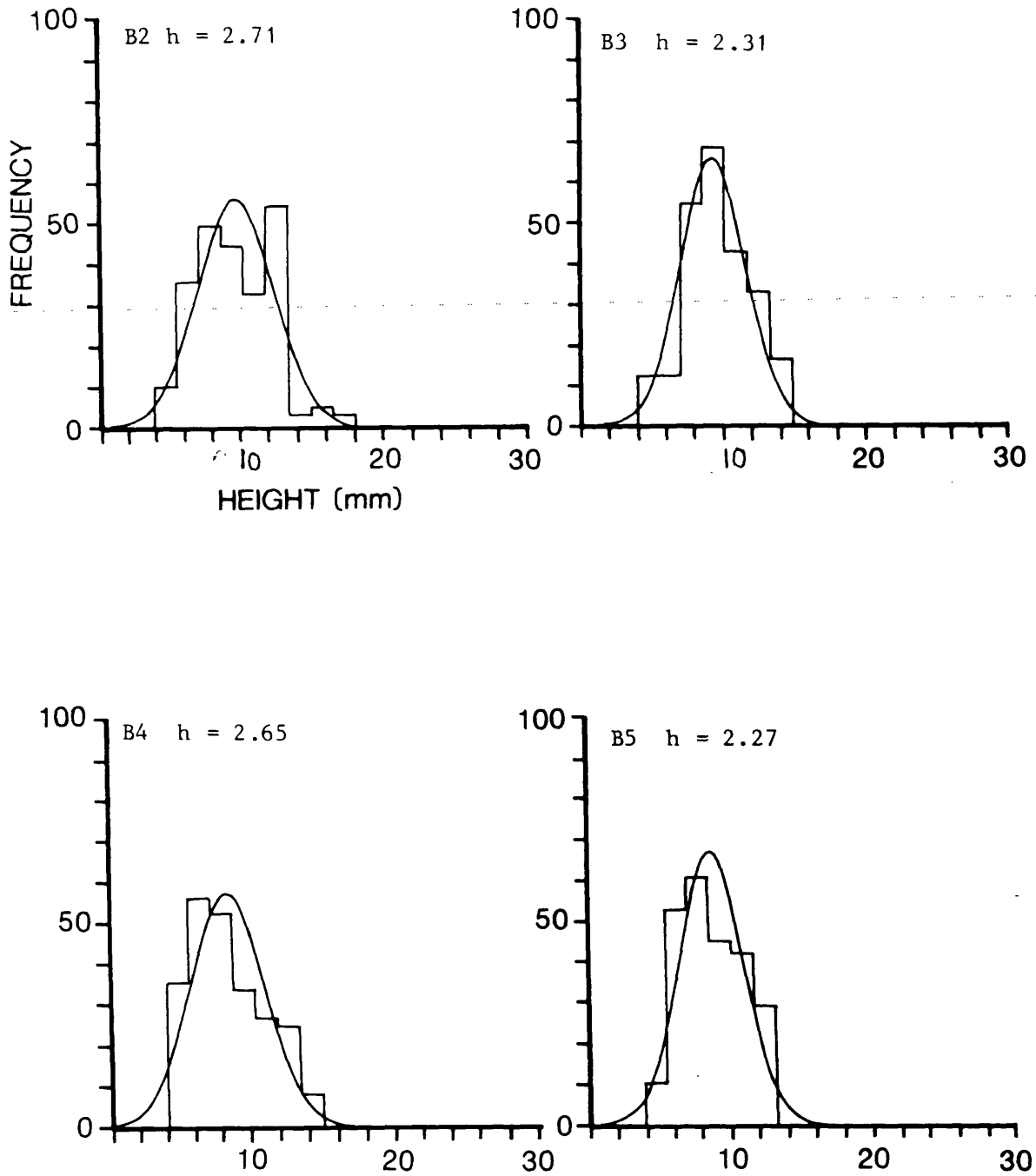
standard deviation h.

Fig 8   Histograms of the measured height distributions compared

with   Gaussian distributions of the same mean and
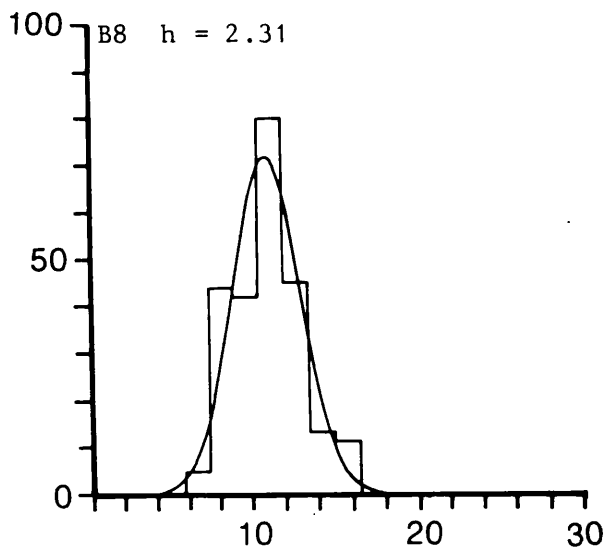
standard deviation h.
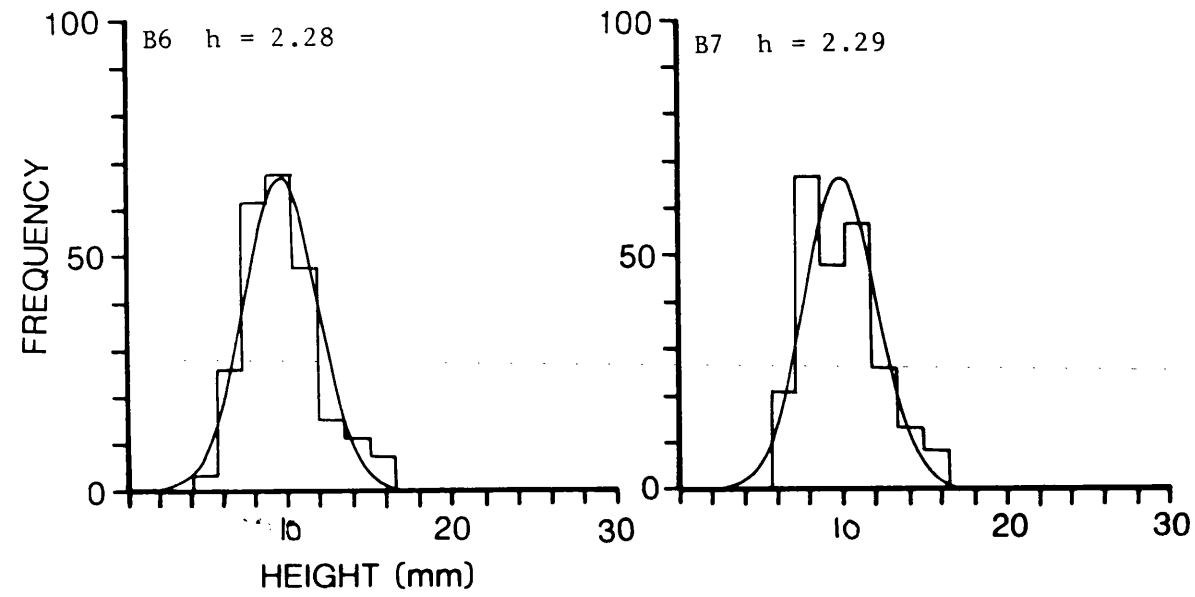
Fig 9   Histograms of the measured height distributions compared

with   Gaussian distributions of the same mean and

standard deviation h.
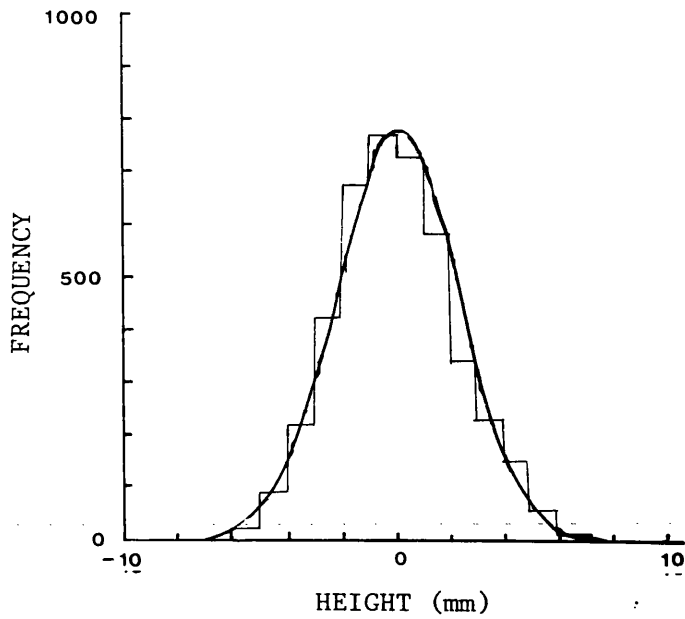
Fig 10   Comparison of the surface height distribution with a

Gaussian distribution with a zero mean plane and root-

mean-square height of 2.2 mm.
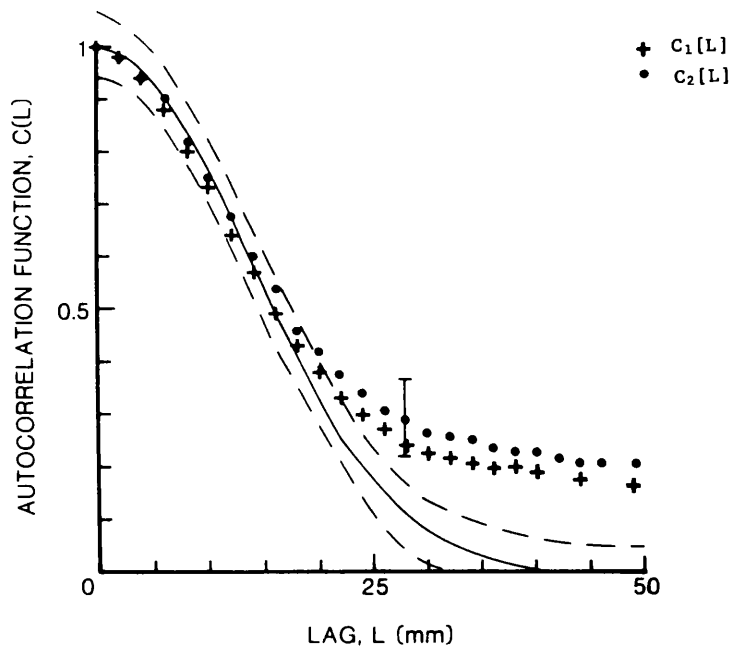
Fig 11   Averaged normalised values as a function of lag.

- Gaussian autocorrelation function $C(r) = \exp(-r^2/T^2)$

where $T = 19$ mm. ---- Expected standard error for a

Gaussian autocorrelation function.

Fig 12   Measured autocorrelation functions compared with Gaussian autocorrelation functions given by $C(r) = \exp(-r^2/T^2)$, where T is the autocorrelation length.   · Measured and - Gaussian.

Fig 13   Measured autocorrelation functions compared with Gaussian

autocorrelation functions given by $C(r) = \exp(-r^2/T^2)$

where T is the autocorrelation length.   • Measured and,

– Gaussian.

Fig 14   Measured autocorrelation functions compared with Gaussian
autocorrelation functions given by $C(r) = \exp(-r^2/T^2)$
where T is the autocorrelation length.   • Measured and,
- Gaussian.

Fig 15   Measured autocorrelation functions compared with Gaussian

autocorrelation functions given by $C(r) = \exp(-r^2/T^2)$

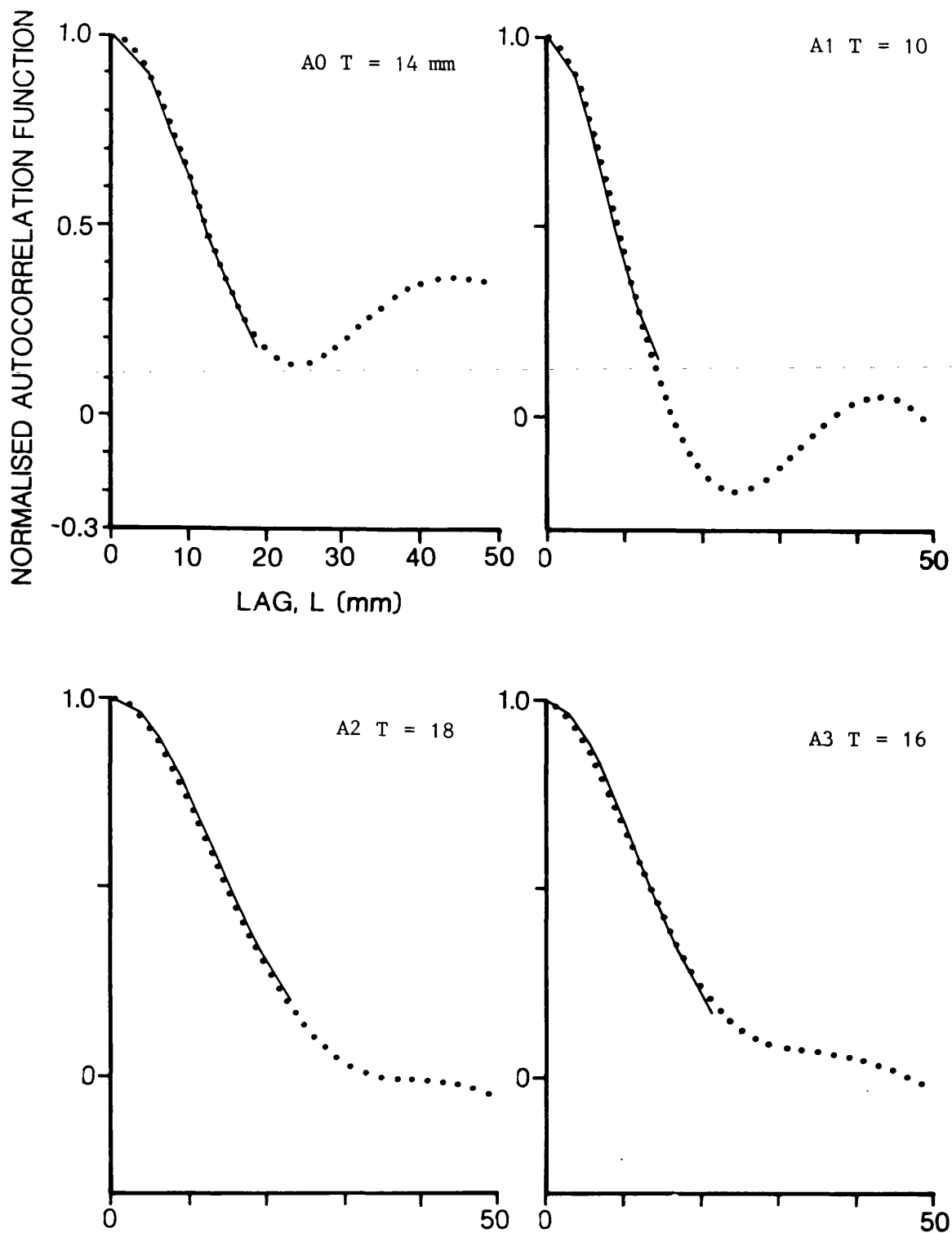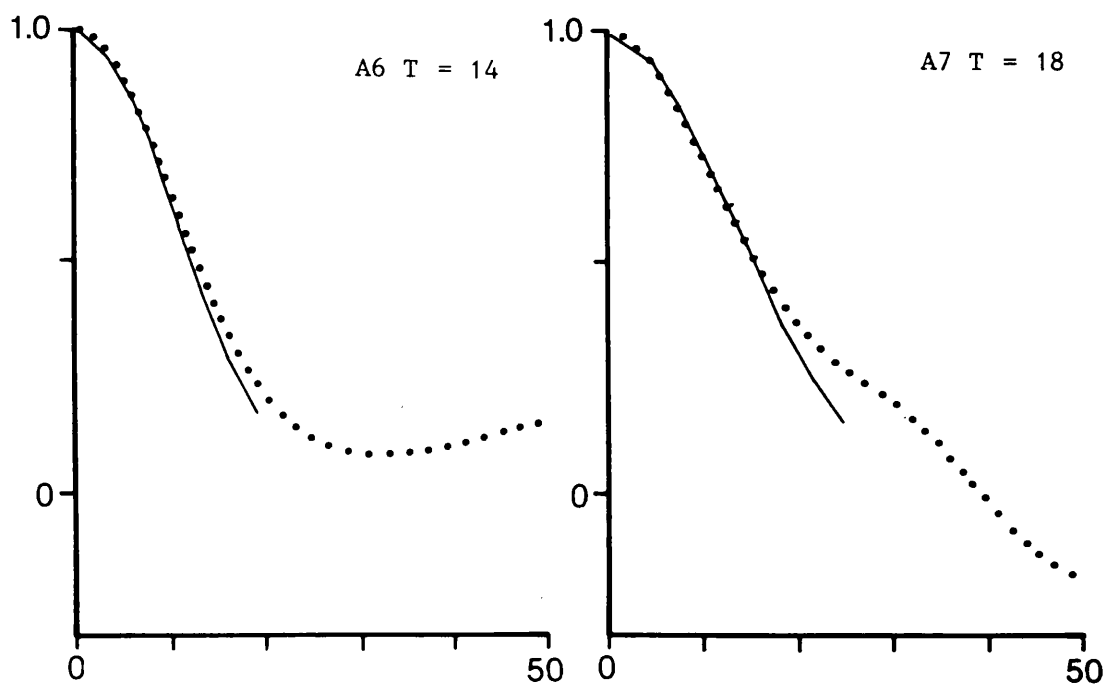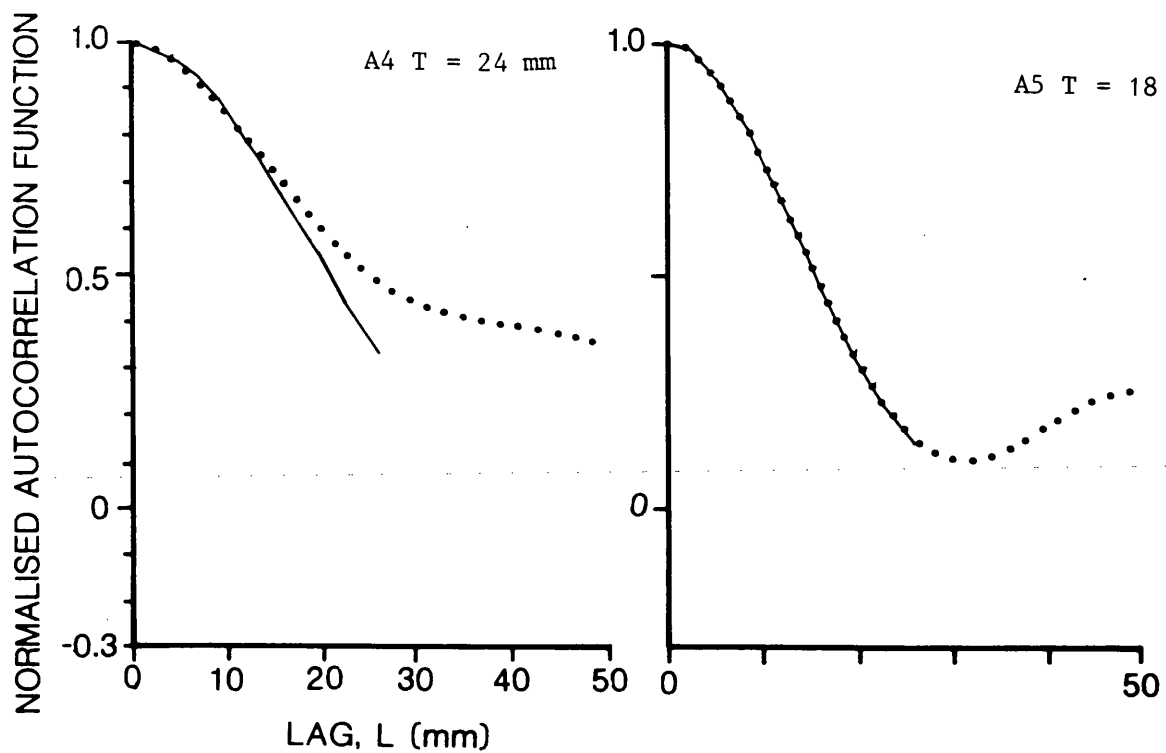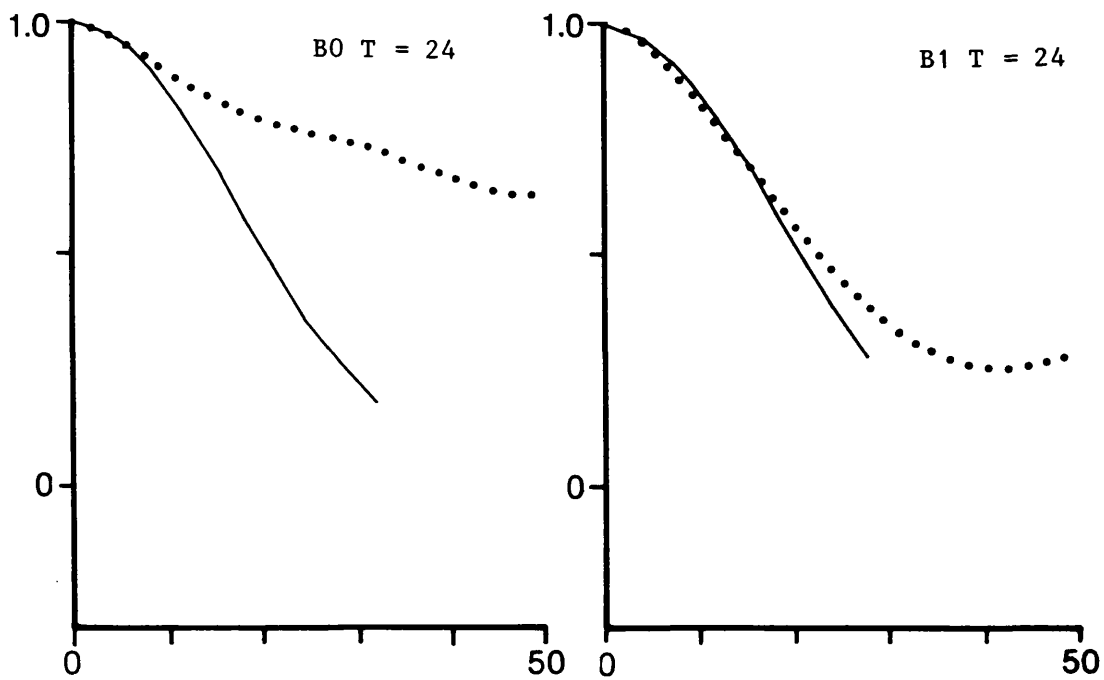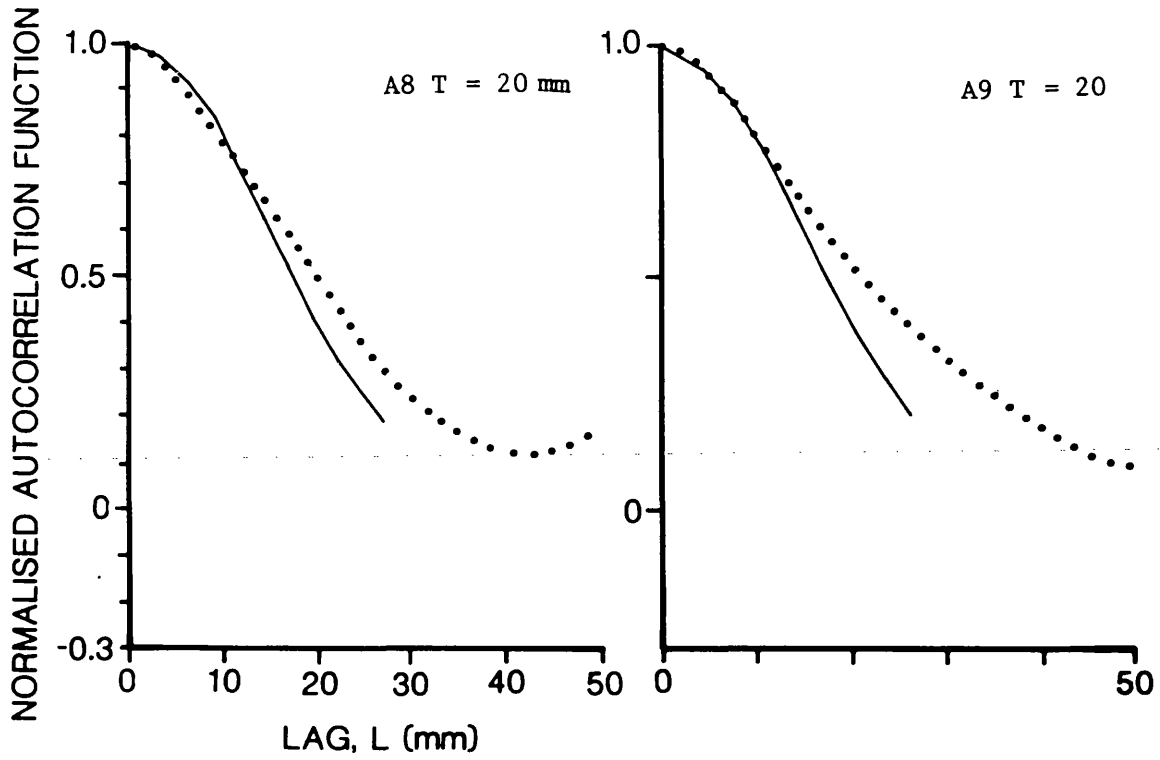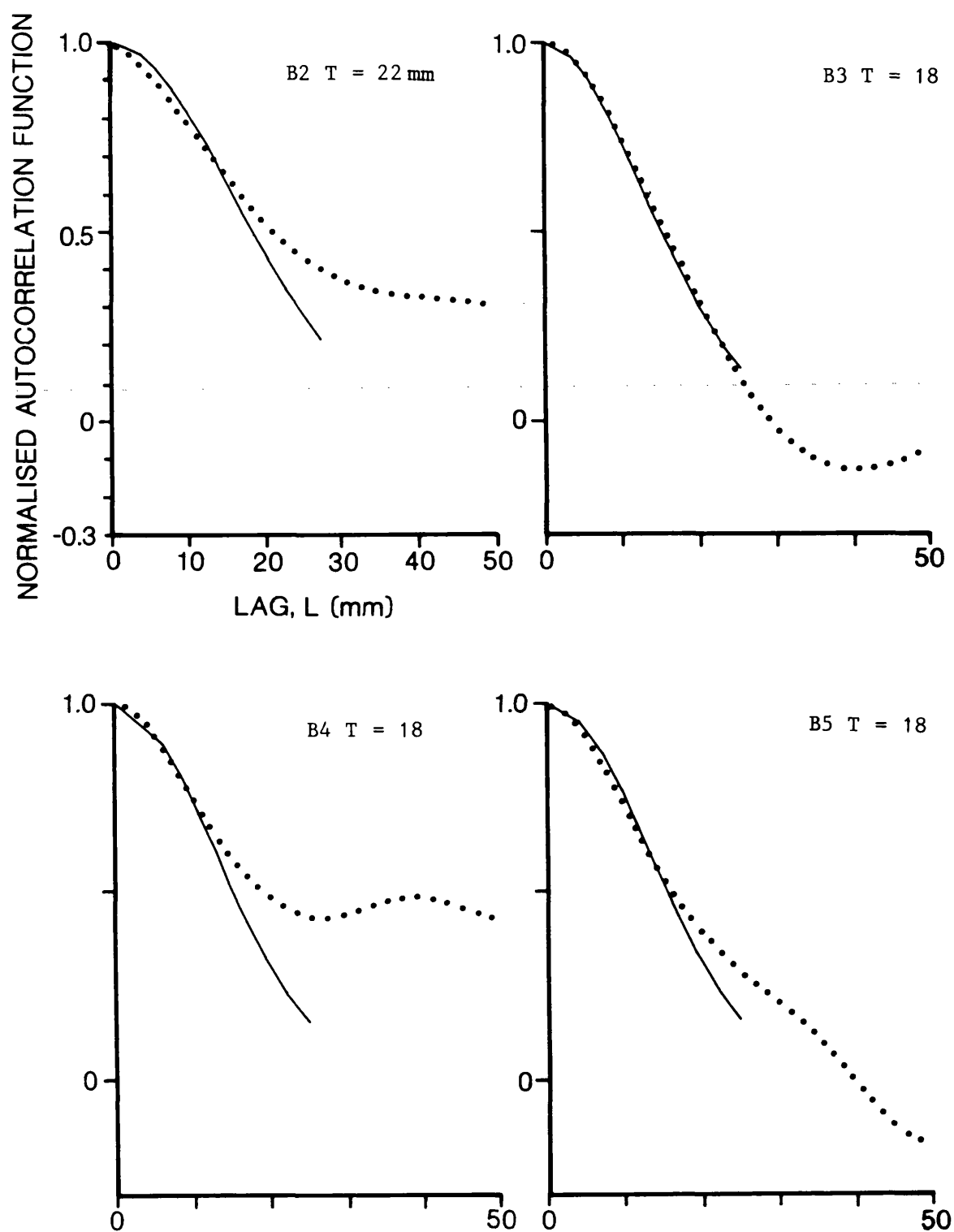where T is the autocorrelation length.   • Measured and,
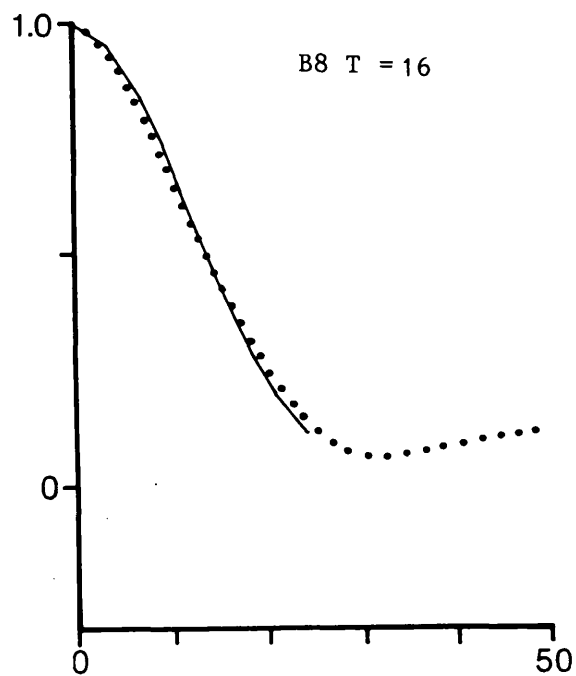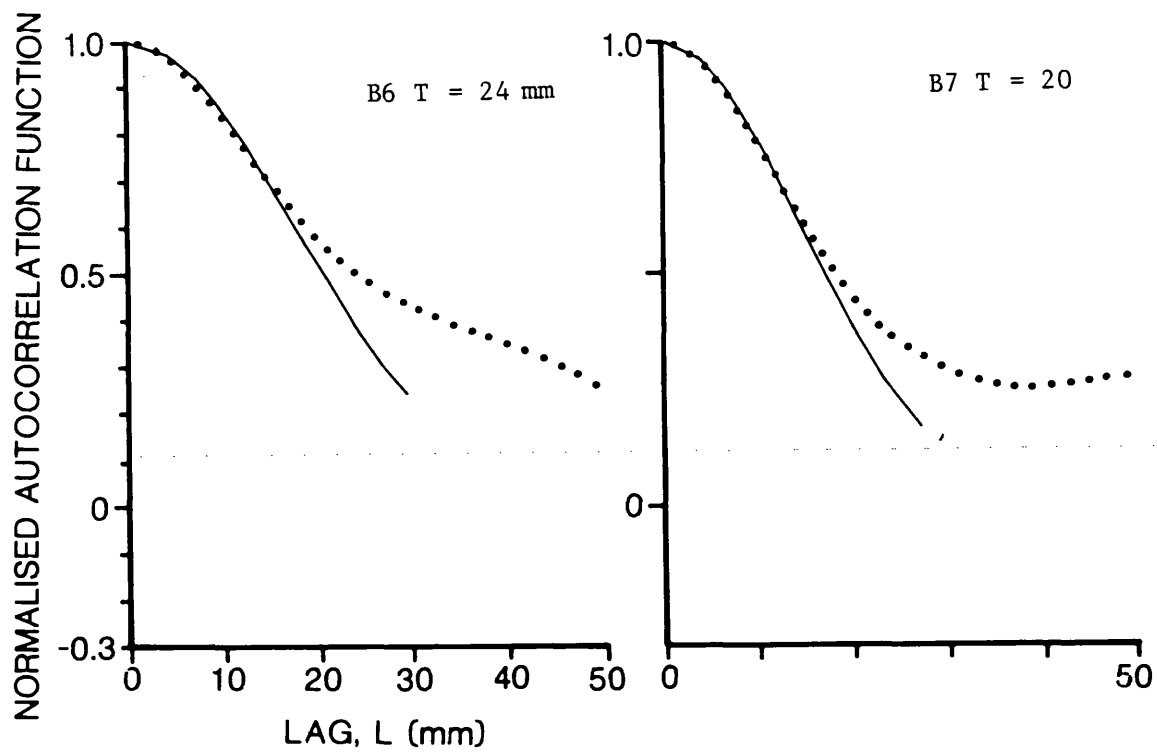
- Gaussian.

Fig 16   Measured autocorrelation functions compared with Gaussian

autocorrelation functions given by $C(r) = \exp(-r^2/T^2)$

where T is the autocorrelation length.   • Measured and,

— Gaussian.

Appendix 3   Details Of The Electronics Constructed

A brief operational description of the electronics built was presented in chapter 4, in this appendix further details of their design is considered.

A3.1   Modulating And Gating Unit

Circuit diagrams of the modulating and gating unit are given in figures 1 and 2. The gating unit of figure 1 was designed to give a pulsed modulating frequency of variable length, starting and terminating at zero cross over points on the waveform, with a wide range of pulse repetition frequencies.

From the input modulating sinewave a square wave was derived using a comparator (A) with a zero reference voltage. The output from the comparator was used to clock a dual edge triggered flip flop (E) of which one output was fed back through a nand gate (B) which allowed two monostable multivibrators (C, D) with 90% duty cycles to act together to effectively give a 100% duty cycle. This yielded a pulse repetition frequency with edges phase locked to the zero crossover points on the modulating signal. The negative edge of the pulse repetition frequency triggered a further monostable (F) the output of which was delivered into the second preset of flip flop (E). The output from the flip flop was used to switch a C-MOS switch (G), into which the modulating signal was fed. The output from the C-MOS switch was the pulsed modulating frequency, the length of which was governed by monostable (F) with a pulse repetition frequency under the control of monostable (C) and (D).
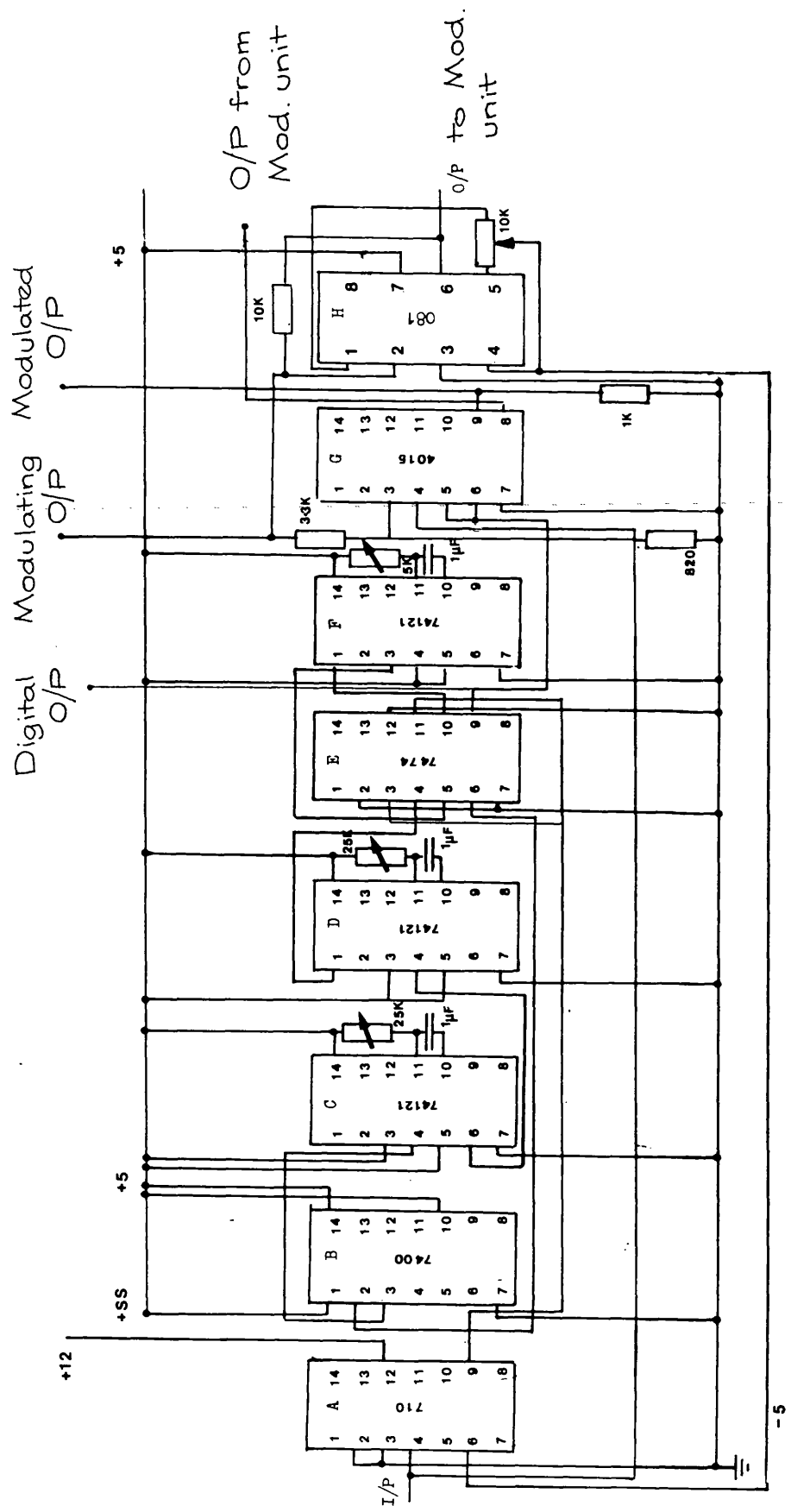
Fig 1 The gating unit.
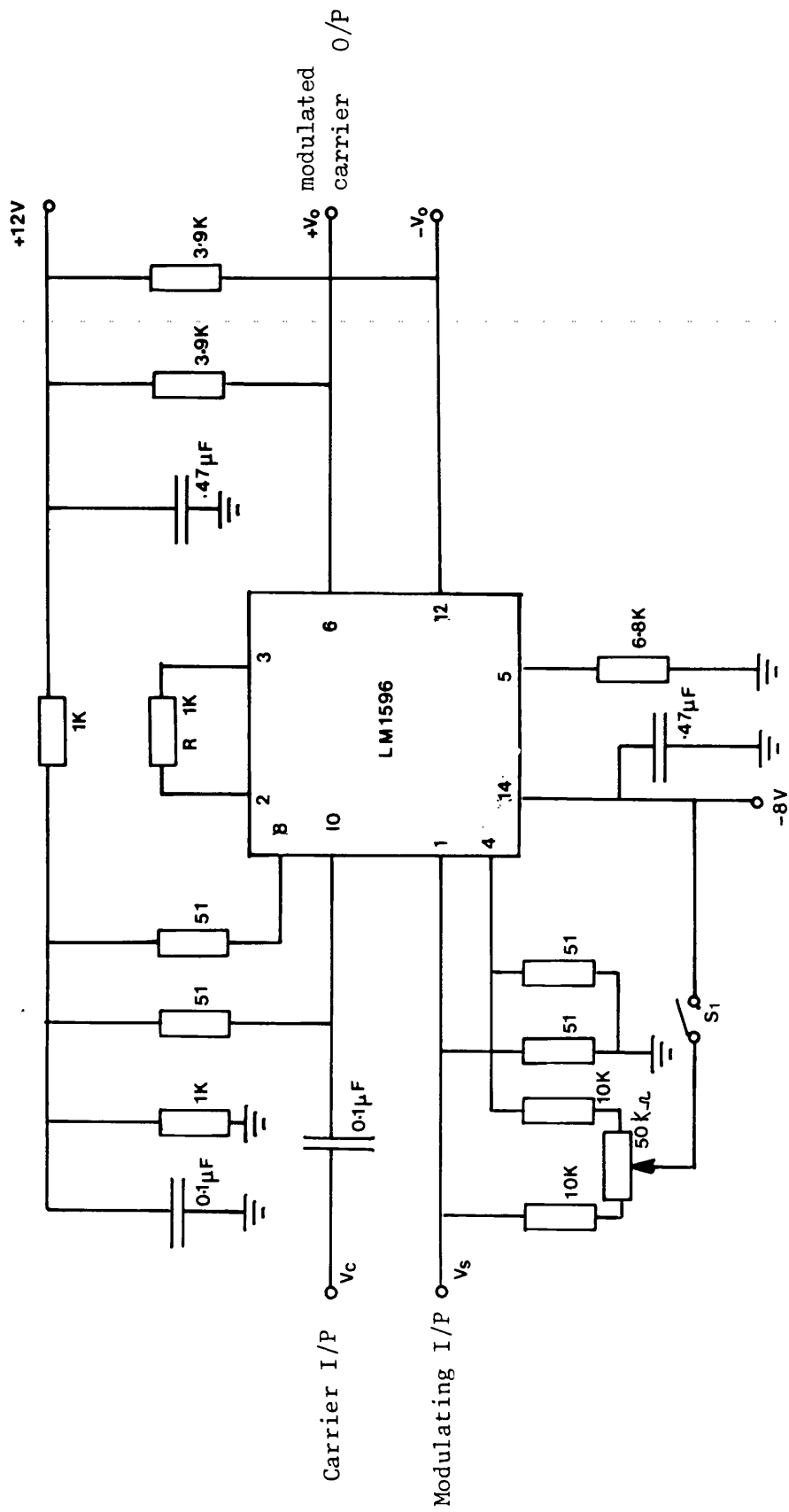
Fig 2 The Modulating circuit.

The pulsed modulating signal was passed through a buffer operational amplifier (H), and with a high frequency carrier, into a balanced modulator-demodulator integrated circuit (I) shown in figure 2. The integrated circuit was operated in suppressed carrier modulator mode which yielded the upper and lower sidebands with an estimated carrier suppression of between 50 db and 65 db.

A3.2 Pre-amplifier

The pre-amplifier shown in figure 3 utilises a compound series feedback circuit which provides a high input impedence amplifier with broadband gain characteristics. The first two stages yielded the voltage amplification and this was passed into the power amplifier through a unity gain operational amplifier. The frequency response of the circuit is given in figure 4 of chapter 4. Adequate gain was available over the frequency range of operation so that maximum output could be obtained from the power amplifier.

A3.3 Passive Filter

The passive filter was constructed to highly attenuate the primary frequencies before the received signal reached any active components which could have produced primary intermodulation frequencies. The attenuation characteristics of the filter are given in figure 10 of chapter 4 and these show that the filter was effective in reducing the primary levels by approximately -80 db. This value of attenuation was sufficient to prevent significant levels of difference frequency being generated by the receiving electronics.
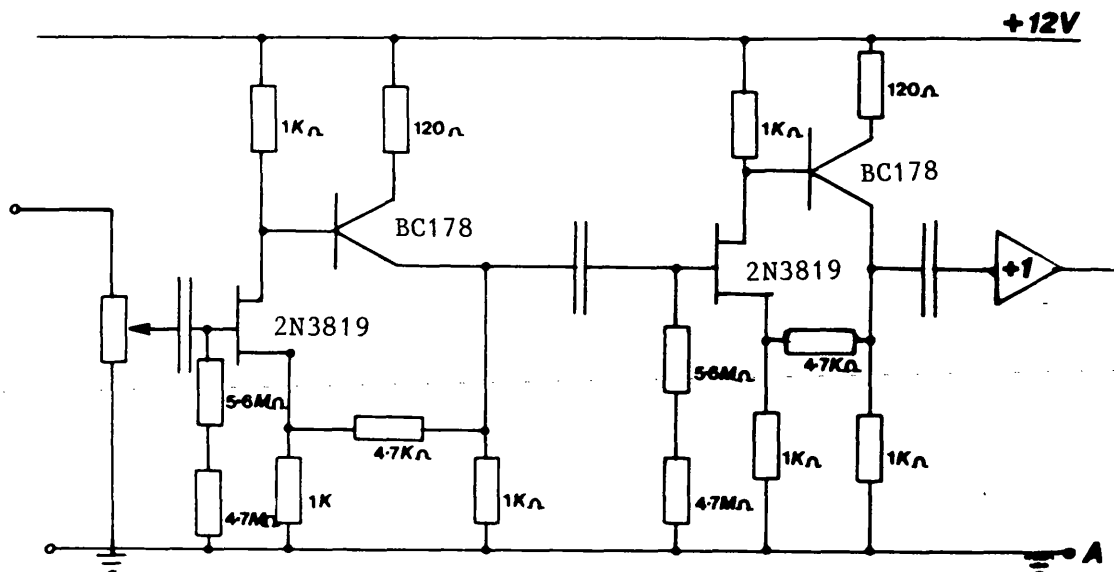
Fig 3 Pre-amplifier design.
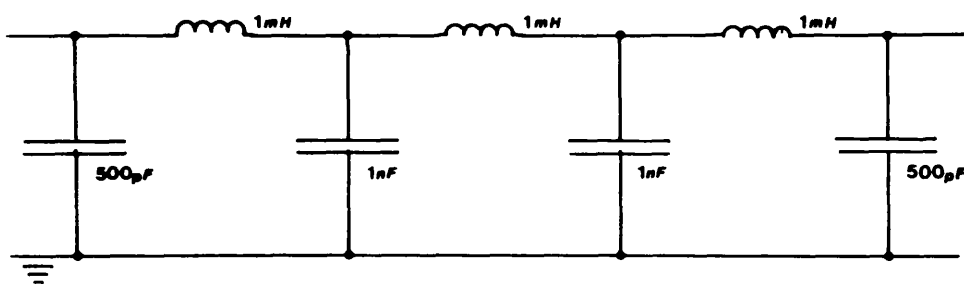
Fig 4 Passive filter.

The circuit design is given in figure 4. The inductors used were recommended for use in the frequency range 3.5-700 kHz and had ferrite cores with a fine core adjustment. They were constructed to have values of 1 mH. 500 pF and 1000 pF high stability silvered mica capacitors were used.

A3.4 Active Low and High Pass Filters

The design of both the low and high pass active filters used a procedure given by Bronzite (52). For a particular pass-band ripple and reject-band attenuation Bronzite tabulates values of low pass and high pass coefficients from which circuit parameters are simply derived.

The form of the circuits are given in figures 3 and 4. Their frequency responses are given in figures 11 and 12 of chapter 4. The low pass filter is of order seven and built around a wideband unity gain amplifier. This filter further reduced the primary frequency levels and high frequency noise present in the system. The high pass filter was used to reduce mains interference.

For all the measurements taken the output voltage from the Brookdeal receiving amplifier was kept below 1 Vp-p to ensure linearity throughout the active section of the receiving system.
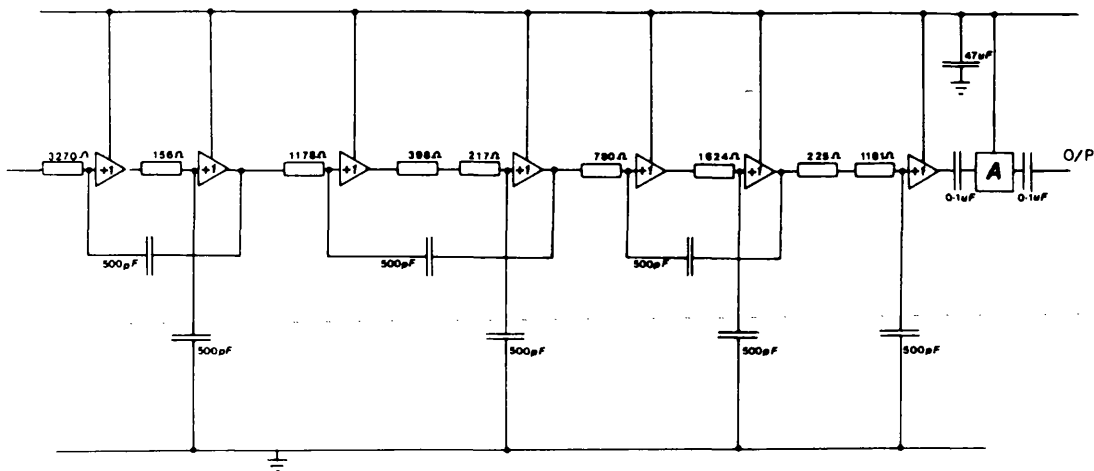
Fig 5   Active low pass filter.
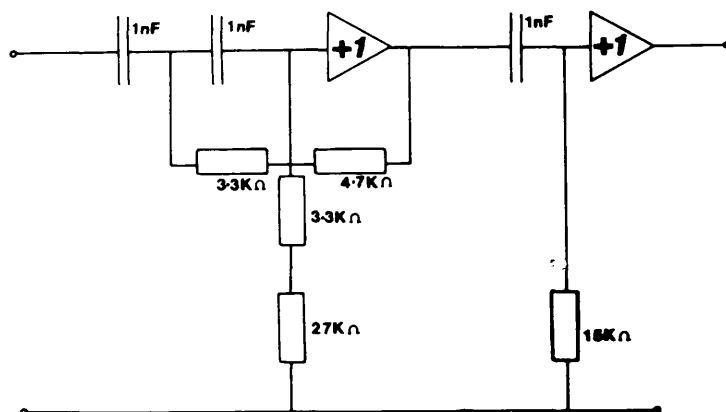
Fig 6   Active high pass filter.

APPENDIX 4   Non-Linear Acoustics And The Parametric Array

A4.1   The Acoustic End-Fire Array

An alternative to the construction of a relatively complicated conventional system to obtain the desired transmitter characteristics was to use the phenomenon of non-linear interaction between two acoustic waves propagating simultaneously through a common region in the water. Within the interaction volume of the primary field, secondary sources are generated due to the inherent non-linearity of the medium. Waves radiate out from these secondary sources which act as an acoustic volumetric end-fire array whose associated field is obtained by integrating over the sources. A particularly important feature of these sources is that they can be utilised to generate highly directional low frequency beams over a broad frequency spectrum by launching directional high frequency waves into the water from a single small transducer resonant at the primary frequencies.

Westervelt (37) analysed this non-linear interaction, and obtained a general source density function for the difference frequency wave generated by the non-linear interaction of two finite amplitude primary waves of different frequencies. The source density function, q, is given by

$$q = \frac{\beta}{\rho_0^2 c_0^4} \frac{\partial}{\partial t}(P_i^2) \qquad\qquad \text{A4-1}$$

Where β is a parameter of non-linearity for the fluid, and ρ_0

and c_0 are the ambient density and sound propagation in the fluid,

and p_i is the primary wave field. Integrating over the source

volume for the particular case of collinated plane primary waves

Westervelt reduced the problem to a line integral over the source

density function, and obtained a farfield solution for the difference

frequency pressure levels. An important aspect of the solution was

the difference frequency directivity function which is given by

$$D = 1/\sqrt{(1 + (2k_-/\alpha_T)^2 Sin^4(\theta/2))} \qquad\qquad A4\text{-}2$$

Where $k_- = k_1 - k_2$ is the difference in the primary wave numbers, and

$\alpha_T = \alpha_1 + \alpha_2 - \alpha$ where α_1 , α_2, and α are the absorption coefficients

of the primary and secondary frequencies respectively. This function

is monotonically decreasing, exhibiting no side-lobe structure. The

half power beamwidth is given by

$$2\theta = 4 Sin^{-1}\sqrt{(\alpha_T/2k_-)} \qquad\qquad A4\text{-}3$$

By appropriate choice of primaries a wide range of narrow low

frequency beams can be obtained in any portion of the low frequency

spectrum.

Early experimental evidence for the ability of this secondary

source volume, commonly called the acoustic end-fire or parametric

array, to generate narrow low difference frequency beams from small

transducers radiating directly at the primary frequencies was produced by Bellin and Beyer (53),Berktay and Smith(54), Hobaek (55) and Muir and Blue(56).

Although it is possible to restrict the secondary source volume to the nearfield of the transducer for high primary frequencies, at lower primary frequencies when attenuation is much weaker this becomes impracticable, and secondary generation predominantes in the farfield of the primary transducer. This region of predominant interaction has been considered for the farfield of the difference frequency by many authors including Fenlon(57), Berktay and Leahy(58) and Moffett and Mellen(59). These studies show that for narrow primary beams the difference frequency can still be highly directional, even though it is principally generated beyond the primary collimated region.

Another valuable property of the difference frequency is the low Q achievable at these frequencies due to the translation of the bandwidth at the primaries down to the difference frequencies. Muir and Blue (60) estimated that the Q_- of a difference frequency is approximately given by

$$Q_- = (f_-/f_0)Q_0 \qquad\qquad A4-4$$

where f_0 is the mean primary frequency, and Q_0 the quality factor for the primaries.

A disadvantage of the parametric array is that since the non-linear interaction is a second order effect, the production of the difference frequency is an inefficient process. For example, in reference (56) the secondary source level was estimated as -36db below the mean primary source level. However, for the present investigation the acoustic system was not unduly limited by the inefficiency of the conversion process, and full advantage was taken of the parametric array's unique properties of wide bandwidth and narrow beamwidths.

In this study the Rayleigh distance of the primary centre frequency was 30 cm and α_{12}, the combined primary wave attenuation coefficient was approximately 0.1 Neper m^{-1}. Therefore a significant proportion of the difference frequency was generated in the farfield spherically spreading primary interaction zone. However, since the difference frequency measurements were taken within two metres of the primary transducer this was still in the primary interaction volume, or difference frequency nearfield. Rolleigh (61) presented a model for the difference frequency pressure levels within the primary interaction region for spherically spreading primaries having negligible attenuation. It was shown that as ℓk_- increases, where ℓ is the distance from the primary transducer to the point of observation, the beamwidth decreases and approaches the product primary directivity pattern as $\ell k_- \to \infty$. Fenlon and McKendree (62) also obtained nearfield half power beamwidths within the nearfield difference frequency. Huckabay (63) experimentally investigated the directivity of the difference frequency and showed an increase in beamwidth occurring within the nearfield as compared with farfield values.

A4.2 Primary And Difference Frequency Measurements

Since the primary and difference frequency measurements were made within two metres of the transducer, both the collimated and spherically spreading region of the primary interaction zone were contributing to the difference frequency near field measurements. Simple analytical solutions for the directivity function of the parametric array are not available in these circumstances, and therefore an experimental investigation of the parametric array was pursued to obtain the information required to carry out the scattering measurements.

The instrumentation used to obtain the primary and difference frequency measurements is shown in figure 1. A 1 MHz centre frequency f_0, and a modulating frequency fm, were fed into a modulator circuit to generate the two primaries at $f_1 = f_0 + fm$ and $f_2 = f_0 - fm$. The primaries were gated, amplified and transmitted by a 1 MHz resonance transducer. After the signal was received the primaries were removed by filtering and the difference frequency, $f_- = 2fm$, was displayed. For measurements at the primary frequencies, a frequency near f_0 was gated and transmitted, and the filtering on reception bypassed. Before measurements were taken, system tests were carried out to ensure that the only place where significant non-linear interaction of the primaries occurred was in the water. These tests are described in chapter 4.

Five primary beamplots were measured at 0.9, 0.95, 1.0, 1.05 and 1.1 MHz at 150 cm from the transducer. Cartesian rather than polar co-ordinates were used, since the former gives the pressure distribution perpendicular to the acoustic axis, and this was of
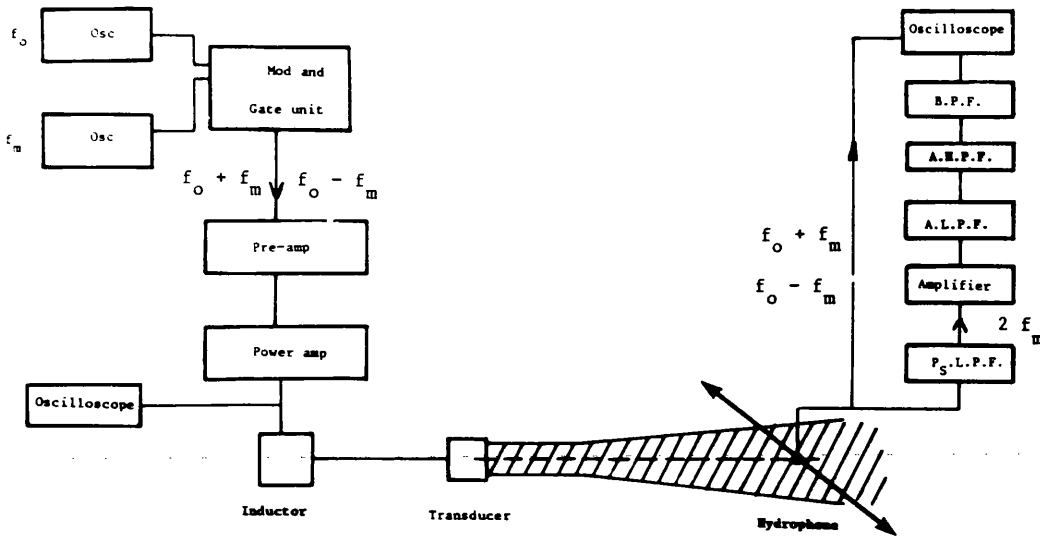
Fig 1   Block diagram of the equipment used. //////

Interaction zone.   Diagram nomenclature, A-Active, L-Low, H-High, B-Band, P-Pass, F-Filter, P_s-Passive
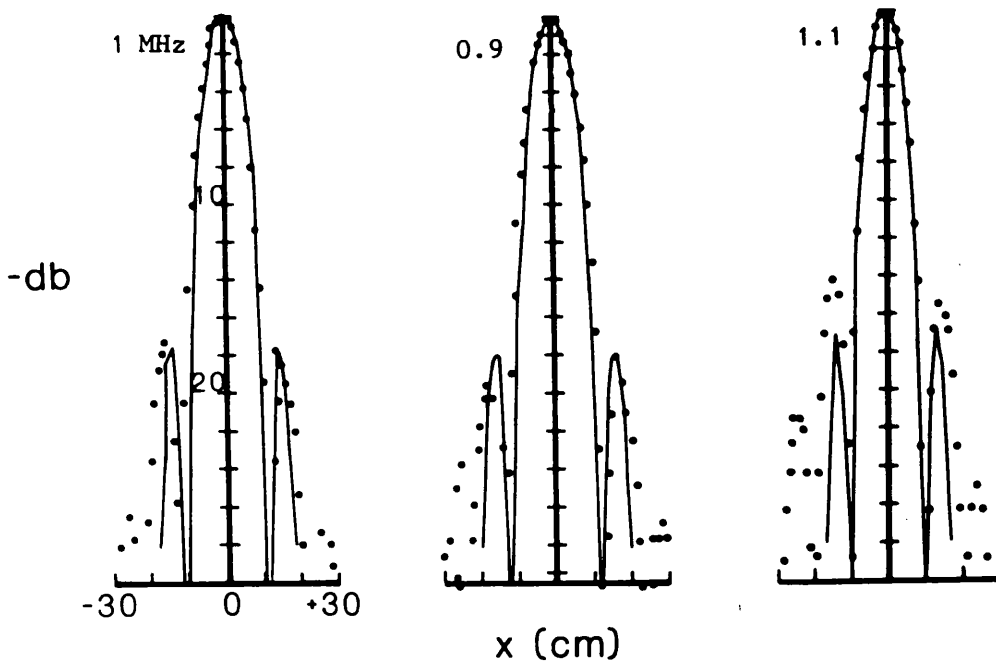

Fig 2   Primary beam profiles at 1, 0.9 and 1.1 MHz in cartesian co-ordinates at 150 cm from the transducer. •Experimental Values – $2J_1(z)/z$ profile where $z = ka\ell/x$.

more interest in relationship to the primary pressure levels over

the rough surface. Three of the five directivity profiles are

shown in figure 2. Comparisons are made with the piston directivity

function

$$D = \frac{2J_1(ka_x/\ell)}{(ka_x/\ell)} \qquad\qquad A4\text{--}5$$

where k is the wave number, a is the piston radius, ℓ is the distance

along the acoustic axis from the transducer, and x is the displace-

ment perpendicular to the acoustic axis. The experimental and

theoretical values are in satisfactory agreement with one another.

Difference frequency beamplots were also measured in Cartesian

co-ordinates. Figure 3a illustrates the geometry for difference

frequency measurements taken at one metre (L_0 = 100 cm) for frequencies

between 10-300 kHz at approximately 30 kHz intervals. A selection of

these beam profiles are shown in figure 4. There is a general decrease

in beamwidth as ℓk_- increases. They show highly directional monotoni-

cally decreasing directivity patterns over a broad frequency range

suitable for carrying out the scattering experiments. Figure 5 compares

these difference frequency nearfield half power beamwidths with those

predicted in reference (62) for $\alpha_T L^* < 0.1$ where $L^* = r_0 f_0 / f_-$ and r_0 is

the Rayleigh distance for the mean primary frequency f_0. For the

measured values $\alpha_T L^*$ varies between 0.1 at 300 kHz to 3 at 10 kHz.

The inequality is not adhered to at the lower difference frequencies,

however the agreement is still reasonable although the beamwidth is

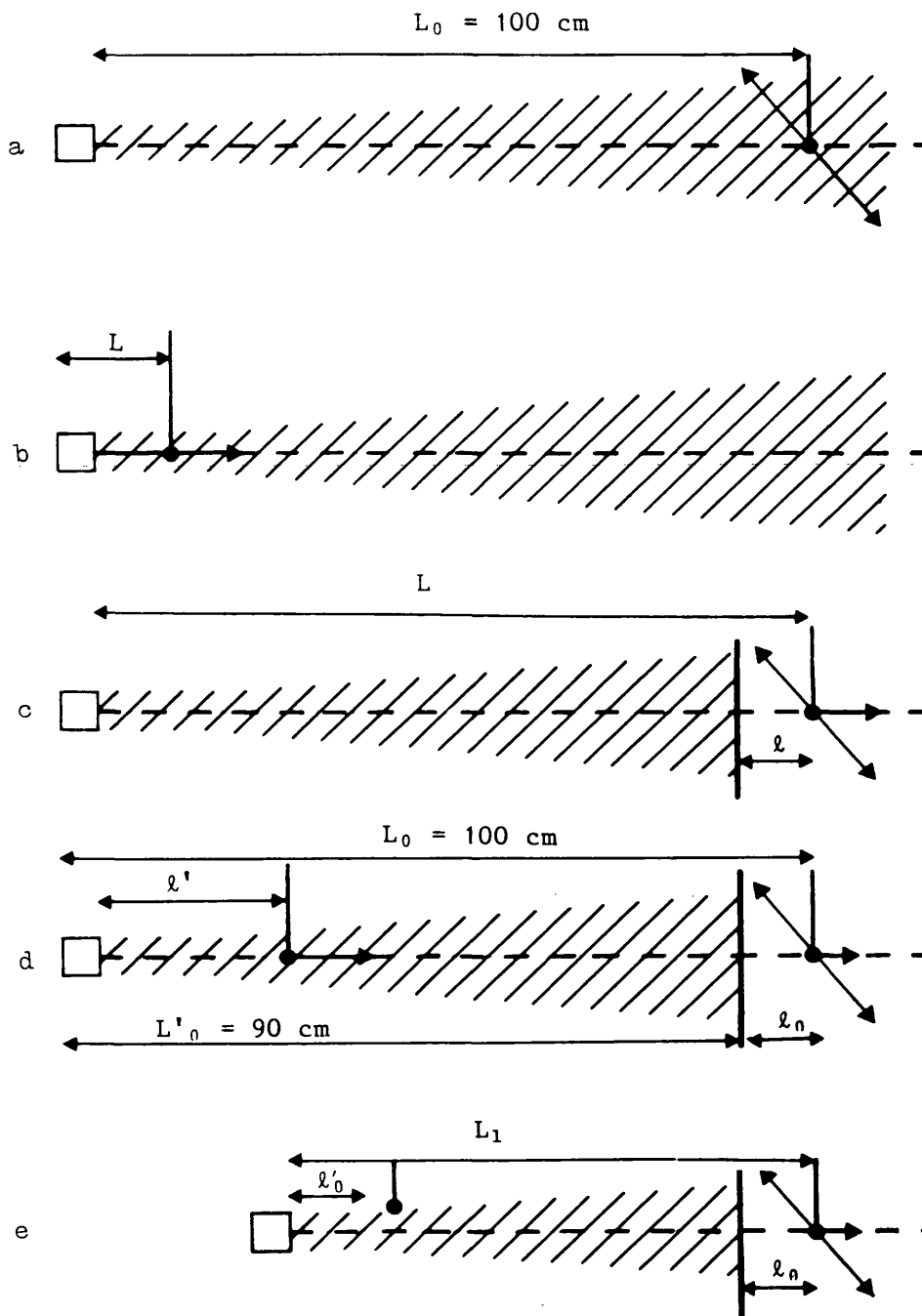over-estimated over the frequency range.

Fig 3 Experimental geometries for many of the measurements.
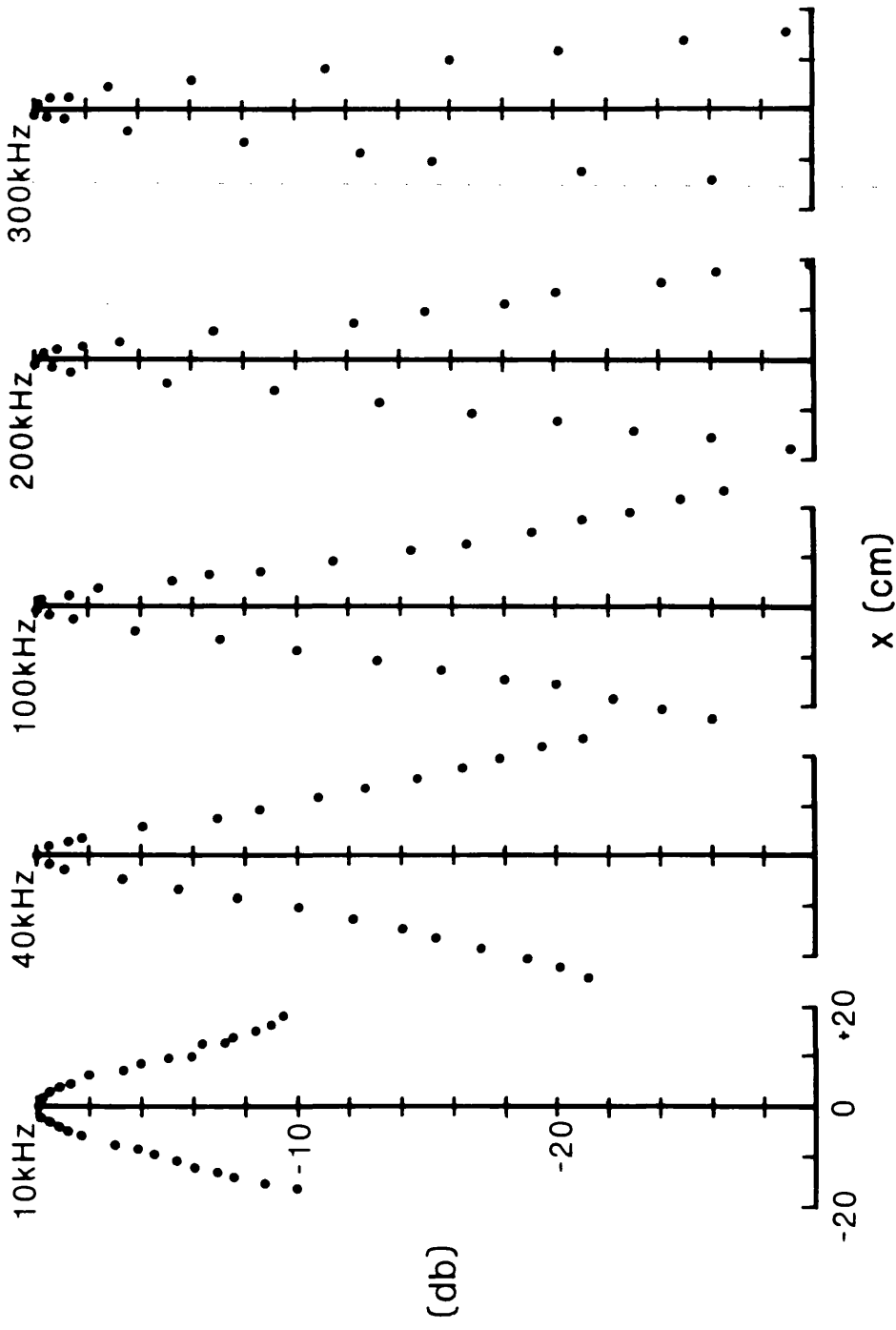
Fig 4 Difference frequency beam profiles measured at 100 cm in cartesian co-ordinates.

Difference frequency axial pressure measurements as illustrated
in figure 3b were taken at a selection of difference frequencies
between 20-280 kHz. Three axial measurements are shown in figure 6.
Axial pressure levels were calculated using

$$p(L, 0) = K1Q1 \qquad\qquad\qquad A4\text{-}6$$

where $|Q|$, derived from two normalised functions, is given by Berktay,
Smith, Braithwaite and Whitehouse (64), and K is a constant which was
empirically chosen to fit the experimental data, for each frequency,
at the furthest distance from the transducer. The predicted form of
the axial pressure is in agreement with the measured values.

A4.3   Introduction Of The Acoustic Filter

There was the possibility in the rough surface scattering experi-
ments that the difference frequency generated by the primary waves
scattered from the rough surface could by interference, affect the
intensity of the difference frequency scattered from the rough surface.
To remove the uncertainty involved in this process, the primary field
was prematurely truncated before the rough surface, using an acoustic
filter of dimensions 30 x 30 x 0.7 cm. Details of the attenuation of
the low pass filter are given in Chapter 4. The effect of the
truncation on the beam profile and the axial pressure levels was
investigated, using the geometry of figure 3c, and some measurements
for each are shown in figures 7a and 7b. The general effect beyond
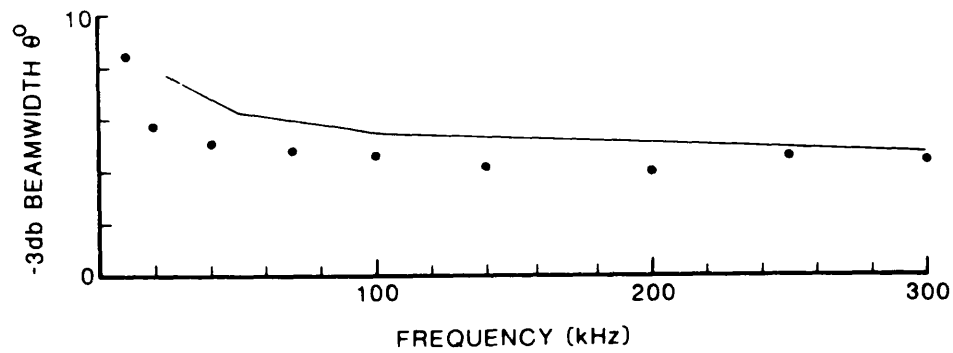
Fig 5 Difference frequency beamwidths at 100 cm from the transducer. •Measured – calculated from reference (62).

AXIAL DISTANCE (cm)
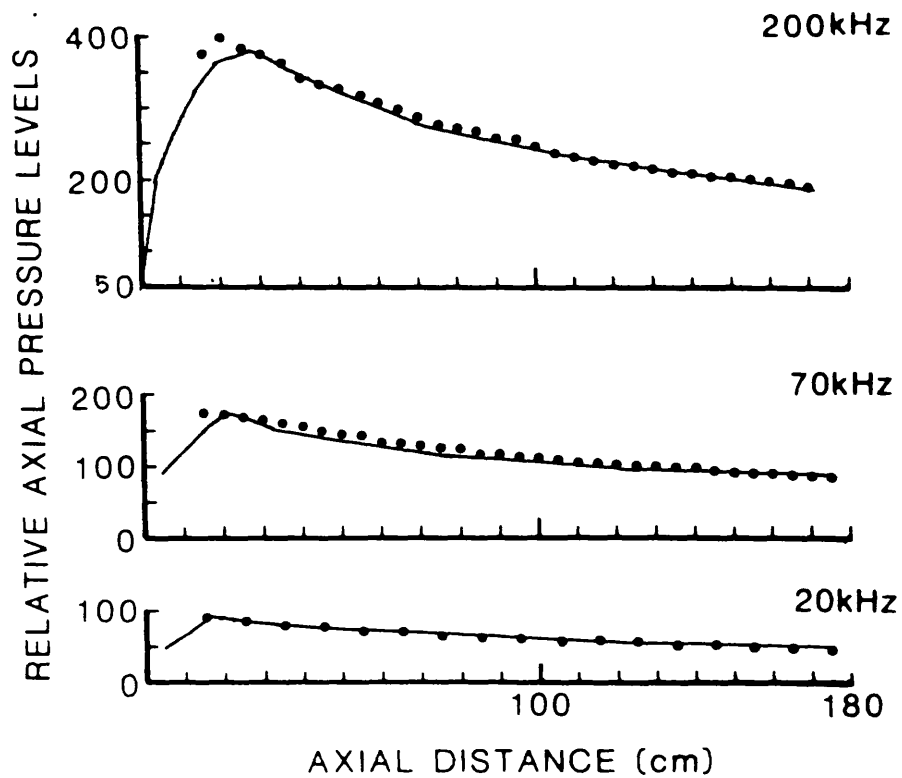
Fig 6 Difference frequency axial pressure measurements.
• Measured.   – Calculated using equation A4-6.
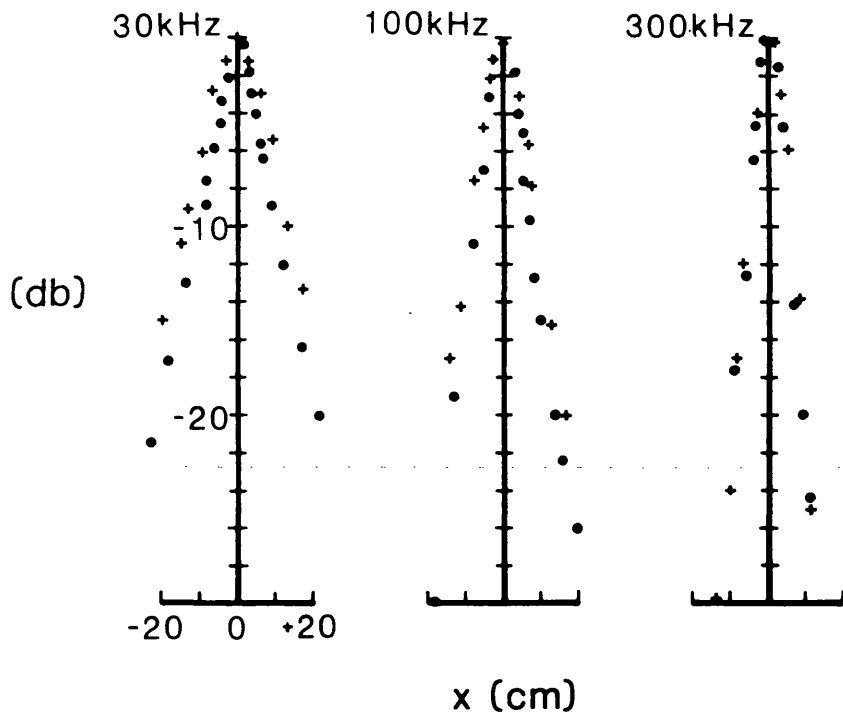
Fig 7a   Cartesian beam profile measurements.   ● Data taken at
86 cm from the transducer with no acoustic filter.   + Same
geometry but with acoustic filter at 76 cm from transducer.
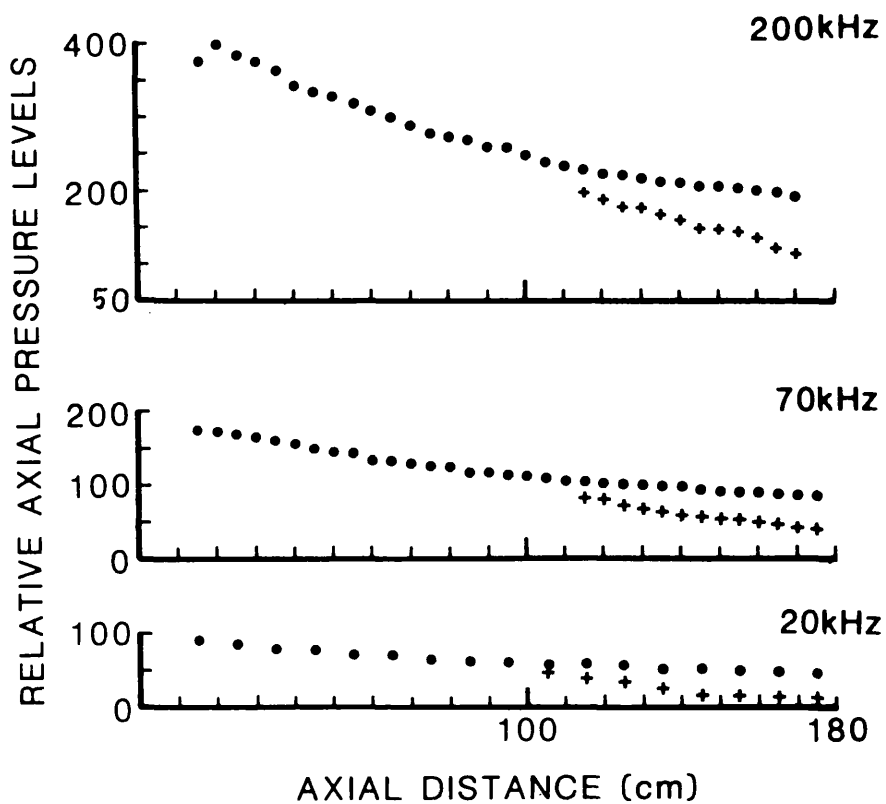
Fig 7b   Axial measurements with the acoustic filter placed at
100 cm from the transducer.   ● Measurements taken with no acoustic
filter.   + Measurements with filter in place.

truncation was to broaden the beamwidth and increase the rate of axial pressure decrease. For the scattering experiments these effects produced no problems, and for some measurements the beam broadening was beneficial.

A4.4 Beam Profile Measurements With Identical Geometries To Those In The Rough Surface Experiments

A4.4.1 Primary frequency measurements

To obtain information of the intensity distribution over the insonified area on the rough surface, beam profiles were taken with identical geometries to those used in the scattering experiments. To ascertain the validity of using a Gaussian beam profile in the theoretical development in chapter 2, comparisons were made with the measured profiles. The exp(-1) distance on the directivity patterns was also required to estimate the predicted scattered intensity.

For the first set of normal incidence acoustic backscattering experiments the receiving hydrophone was placed on the acoustic axis. However, before investigating the effect the on-axis hydrophone had on the difference frequency beam profiles, measurements were made on the primary frequency profiles.

Both the on-axis hydrophone in front of the transducer, and the hydrophone used to measure the primary frequency beam patterns were Bruel and Kjaer 8103's details of which are given in chapter 4. Both were attached to the end of a 1 cm diameter stainless steel tube.

For the primary frequency measurements one hydrophone was placed on the acoustic axis at positions ranging from 9-40 cm from the transducer, and the second hydrophone measured the beam pattern at 150 cm from the transducer. Experiments were carried out at 0.9 and 1.1 MHz. The influence of the on-axis hydrophone was very similar at both frequencies and figure 8 illustrates the principal effects. Compared with figure 2 they show that the presence of the on-axis hydrophone introduced a side-lobe structure into the main beam, and the usual sidelobe structure became more complicated. This effect was due to the transmitted primary signal from the transducer reflecting off the hydrophone and its mounting and interfering with the out-going signal. To measure the influence the primary beam pattern modification had on the difference frequency beam profile a series of measurements were conducted.

A4.4.2 Difference frequency beam patterns (I)

For the first set of measurements on the rough surface, the transducer was kept at a fixed distance of 100 cm from the surface. Insonification was at normal incidence. The normal incidence back-scattered intensity was measured by placing a hydrophone on the acoustic axis. Measurements of the intensity were taken at distances from the rough surface of the 70, 50, 30 and 20 cm. For the difference frequency beam pattern measurements, one hydrophone was placed on the acoustic axis at each of these four positions in turn, and the other was at 100 cm from the transducer in the vertical plane which the rough surface occupied in the scattering experiments. The acoustic filter was placed on the acoustic axis at 90 cm from the transducer, which was the position it occupied in the first set of scattering

1.1MHz   0.9MHz
37cm   10cm

(db)

-10

-20

0   30

x (cm)
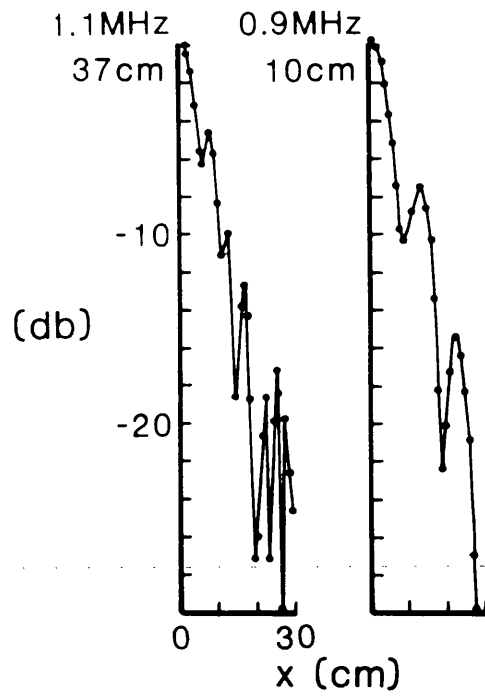
Fig 8   Beam profiles measured at 150 cm with a second hydrophone
on the acoustic axis at 37 and 10 cm from the transducer.

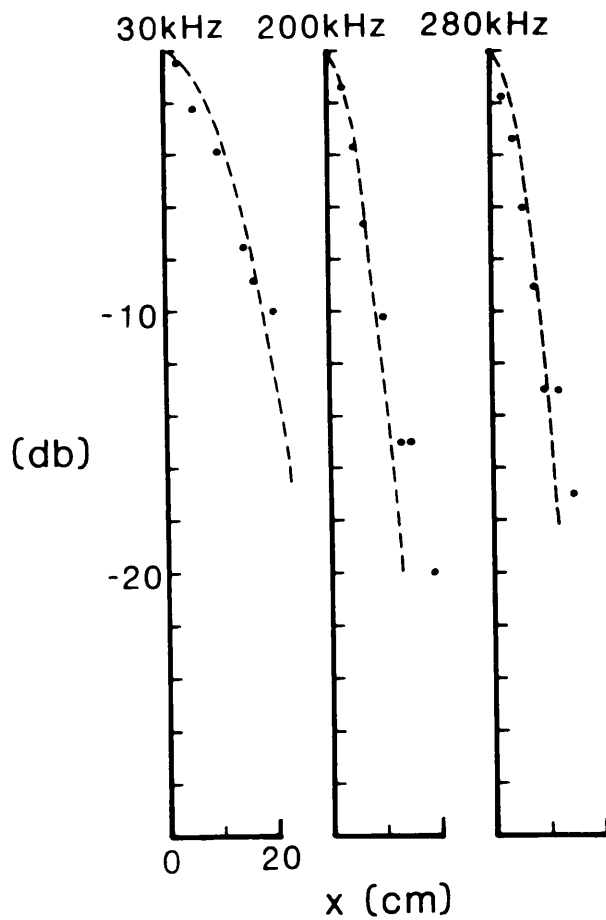30kHz   200kHz   280kHz

(db)

-10

-20

0   20

x (cm)

Fig 9   Difference frequency beam profiles at 100 cm from the transducer.
A second hydrophone had been placed on the acoustic axis at 70 cm from
the rough surface position which was 30 cm in front of the transducer.
● Measured values.   ――― Gaussian profiles.

experiments. Figures 9 and 10 show the effect the on-axis hydro-
phone,placed at 30 and 80 cm from the primary transducer had on
the difference frequency beam pattern. The geometry used is shown
in figure 3d where L_0 = 100 cm, L_0' = 90 cm and ℓ' takes on values
of 30, 50, 70 and 80 cm.

A Gaussian directivity function was compared with the measured
values. The Gaussian profiles were in reasonable agreement with the
observed beam patterns, until at the higher difference frequencies
a sidelobe structure became prevalent in the usual monotonically
decreasing difference frequency beam pattern. Since in all cases
the low frequency profiles did not exhibit the sidelobe structure,
it was probable that the change in pattern was not primarily due
to the hydrophone's effect on the primaries, but to the afore-
mentioned interference effect noted at the primaries, acting upon
the higher difference frequencies. Such an effect would therefore
be unavoidable even with a conventional system when trying to
measure the normal incidence backscattered intensity with a large
separation between the source and receiver, when the receiver is
close to the rough surface.

The change in beam pattern became particularly dominant in the
case where the on-axis hydrophone was at 80 cm from the transducer
and the frequency was higher than 200 kHz. Treating the difference
frequency intensity distribution over the rough surface as Gaussian
became a less accurate representation. However, for the majority of
higher difference frequency beam profiles measured, the patterns
were no worse than the usual diffraction pattern of a conventional
system, which has generally been used by other researchers in previous
scattering experiments. Also the profiles were still well behaved in

30kHz   120kHz   200kHz   280kHz

(db)

-10

-20

0   20

x (cm)

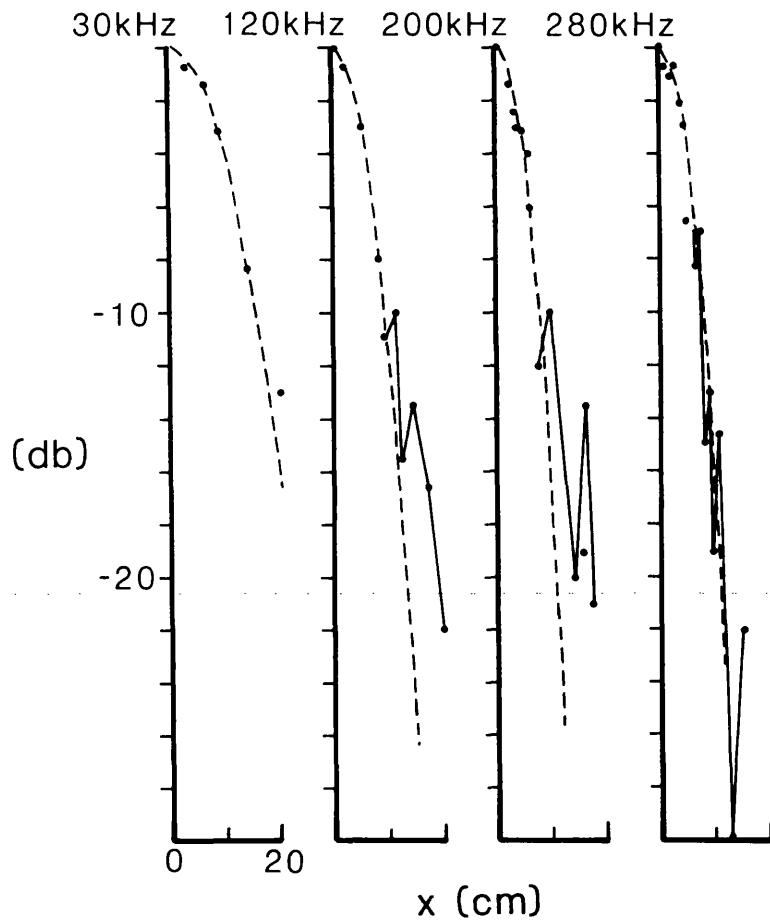Fig 10   Difference frequency beam profiles at 100 cm from the
transducer with a second hydrophone 20 cm from the rough surface
position. ● Measured values.   --- Gaussian profile.
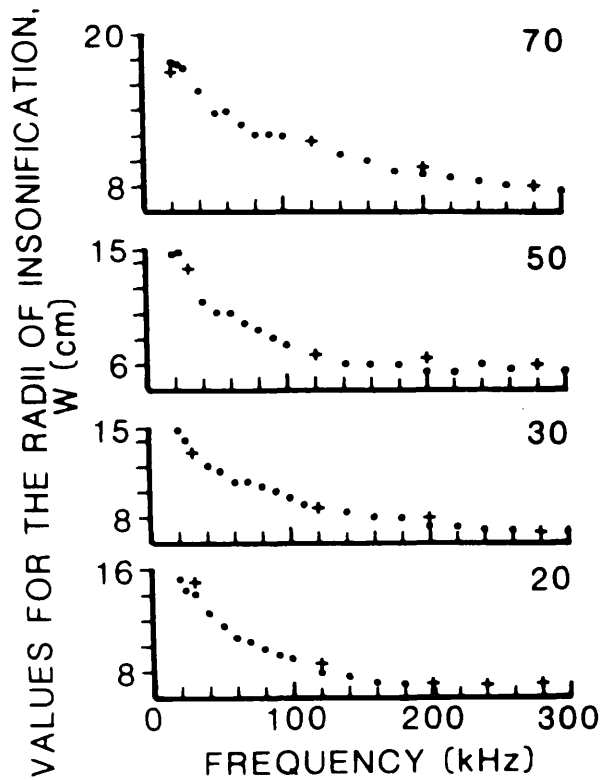
VALUES FOR THE RADII OF INSONIFICATION, W (cm)

20
8
70

15
6
50

15
8
30

16
8
20

0   100   200   300
FREQUENCY (kHz)

Fig 11 The e^{-1} point on the beam profiles. ● Measured from the acoustic
axis. + Taken from full beam profiles.

the region of maximum incident pressure levels about the acoustic
axis, and this region of insonification would have had the major
influence on the scattered intensity.

Figure 11 gives the 1/e distances on the directivity patterns
for the four on-axis hydrophone positions. These distances give
the values for 'W' used in chapter 2, and they are needed to cal-
culate the theoretical scattered intensity. Because the Gaussian
curve was not a perfect fit to the measured profiles, as can be
seen in figures 10 and 11 and due to the sidelobe structure, an
inaccuracy of about 5% was placed on 'W'.

A4.4.3 Difference frequency beam patterns (II)

For the second set of normal incidence backscattered intensity
measurements the transducer and hydrophone remained a fixed distance
apart, and both were simultaneously moved towards the rough surface.
In this series of experiments the hydrophone was always 16 cm in
front of the transducer, this was within the Rayleigh distance of
the primaries, and it was displaced by 2.5 cm off the acoustic axis
where it did not significantly interfere with the primary or
secondary field. The transducer was again insonifying the surface
at normal incidence. Displacing the hydrophone slightly off axis
was possible in these experiments because of the small separation
between the transducer and the hydrophone. The hydrophone measured
the backscattered intensity at receiver distances of 70, 50, 30 and
20 cm from the rough surface, and the distance from the transducer
to the rough surface was 86, 66, 46 and 36 cm respectively. Again
the acoustic filter was centred on the acoustic axis, 10 cm in front
of the rough surface.

With the transducer and hydrophone occupying identical positions
to those used in carrying out the second set of scattering measurements,
another Bruel and Kjaer 8103 hydrophone measured the beam pattern at
the position the surface occupied in the scattering experiments. This
geometry is shown in figure 3e, where $\ell_0' = 16$ cm, $\ell_0 = 10$ cm and
$L_1 = 86$, 66, 46 and 36 cm. For each of these positions, beam profiles
were measured at four frequencies, 30, 100, 200 and 300 kHz. The 30
and 300 kHz plots are shown in figure 12. Comparisons were made with
Gaussian directivity functions, and good agreement was observed. The
$1/e$ points on the beam pattern are given in figure 13.

A4.5 Axial Pressure Measurements With Identical Geometries To The Rough Surface Experiments

In chapter 2 the incident radiation was assumed to have a $1/R$
decrease in pressure with range, but figures 6 and 7b show that this
is not the case for the difference frequency axial pressure levels.
However, for the scattering experiments, only the relationship
between the pressure levels at the surface and at the receiving
position were needed. This allowed the truncated parametric array
to be treated as a conventional source, beyond the point of truncation
as far as the axial levels were concerned.

The location of this apparent source was arranged so that from
the position of truncation, the pressure level fell off as $1/R$
with reference to the source. The distance from the position the
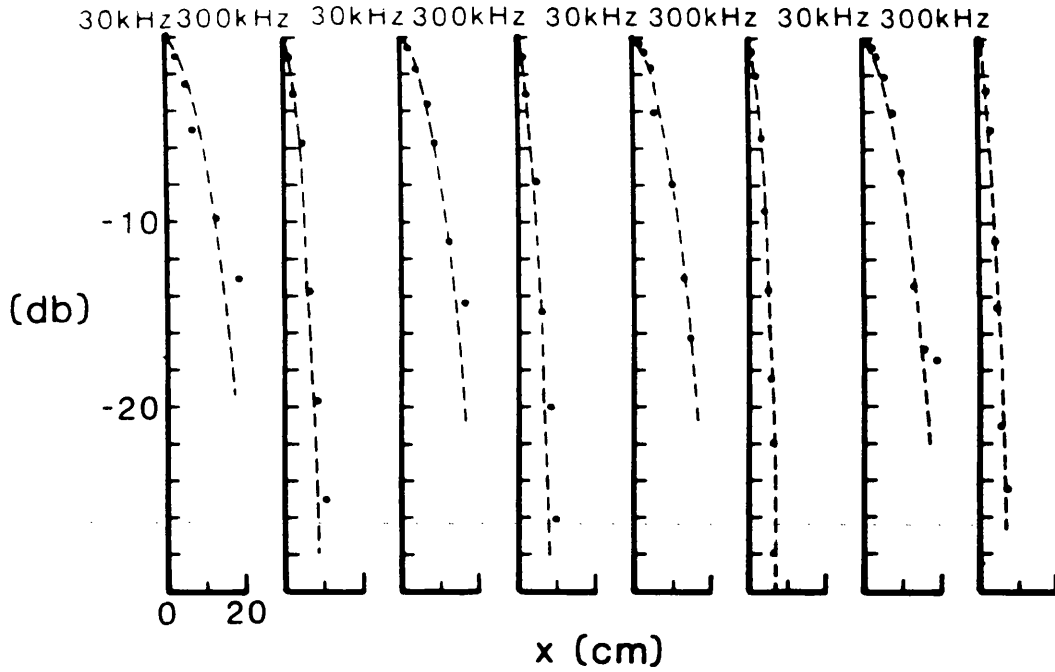rough surface occupied in the scattering experiments to the

Fig 12 Difference frequency beam profiles at 86, 66, 46 and
36 cm from the transducer with a second hydrophone 16 cm in
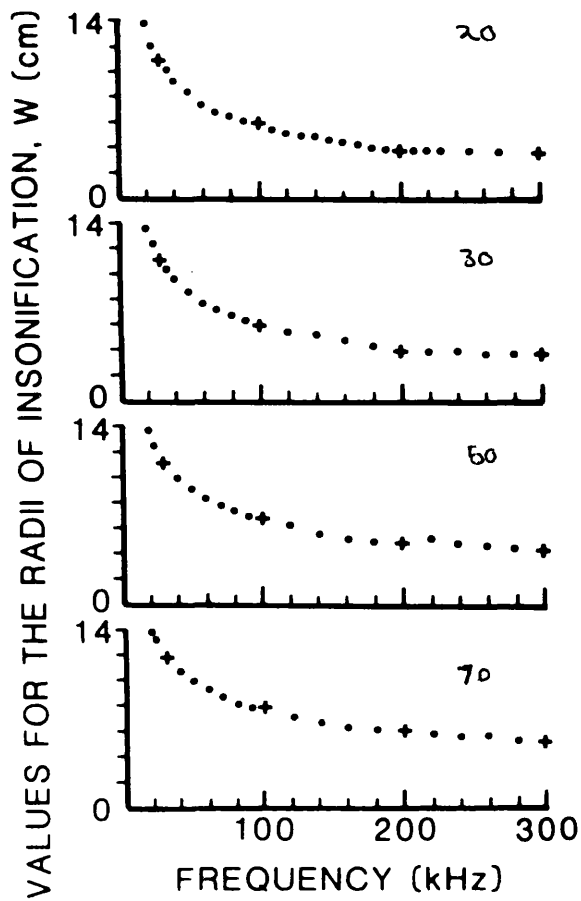front of the transducer. ● Measured values. ― ― Gaussian profile.

Fig 13 The e⁻¹ point on the beam profiles. ● Measured from the
acoustic axis. + Taken from full beam profiles.

receiving position was given by R_1, and this was the actual measured

distance. The distance from the apparent source to the surface, R_0,

was given by

$$R_0 = \frac{R_1}{[(p_0/p) - 1]} \qquad\qquad \text{A4-7}$$

where p_0 was the pressure at the rough surface, and p was the pressure

at R_1. R_0 was not the distance from the primary transducer to the

surface, it was a distance which allowed the axial pressure levels

after truncation to be given by

$$p = \frac{p_0 R_0}{(R_0 + R_1)} \qquad\qquad \text{A4-8}$$

Treating the parametric array in this way prevented particularisation

in the development of the scattering theory of chapter 2 for a para-

metric source.

To illustrate the point, axial pressure amplitude measurements

were taken from the point of truncation. Graphs of R_1 against

$[(p_0/p) - 1]$ were plotted. In these measurements p_0 was the pressure

at the point of truncation, and p was the pressure at a distance R_1

from the point of truncation. A least square fit was carried out on

this data, the gradient of which gave R_0, and the constant usually had

a magnitude less than unit and was ignored. The calculated values

for R_0 gave the distance from the apparent conventional source to

the truncation point. Figure 14 show five sets of measurements
at a selection of frequencies which show the axial pressure level
after truncation conforming to a 1/R reduction in pressure level
with distance, where R = (R_0 + R_1), for the distances considered.

As previously mentioned, for the scattering measurements, only
the pressure levels at the surface and receiver positions needed
to be compared. Using experimental arrangements identical to those
described in the previous section for the two sets of scattering
experiments, the on-axis pressure was measured at the rough surface
distance, and at a distance equal to that from the transducer to
the surface and back to the receiving hydrophone. The pressure
levels were measured at a number of frequencies and R_0 the distance
from the apparent conventional source to the receiver, was
obtained by using equation A4-7 at each of the selected frequencies
for the four experimental arrangements in each of the two sets.
For each of the arrangements the measured value of R_0 was related
empirically to the frequency f using

$$R_0 = Af^B \qquad\qquad\qquad A4-9$$

Where A and B were obtained by linear regression on the logarithms
of R_0 and f. The predicted values for p/p_0 using equation A4-8,
where R_0 is obtained from equation A4-9 are compared with the
measured values in figures 15 and 16. The calculated values are in
very good agreement with the measured values. The calculated values
for R_0 used in these figures are the values used in the estimation
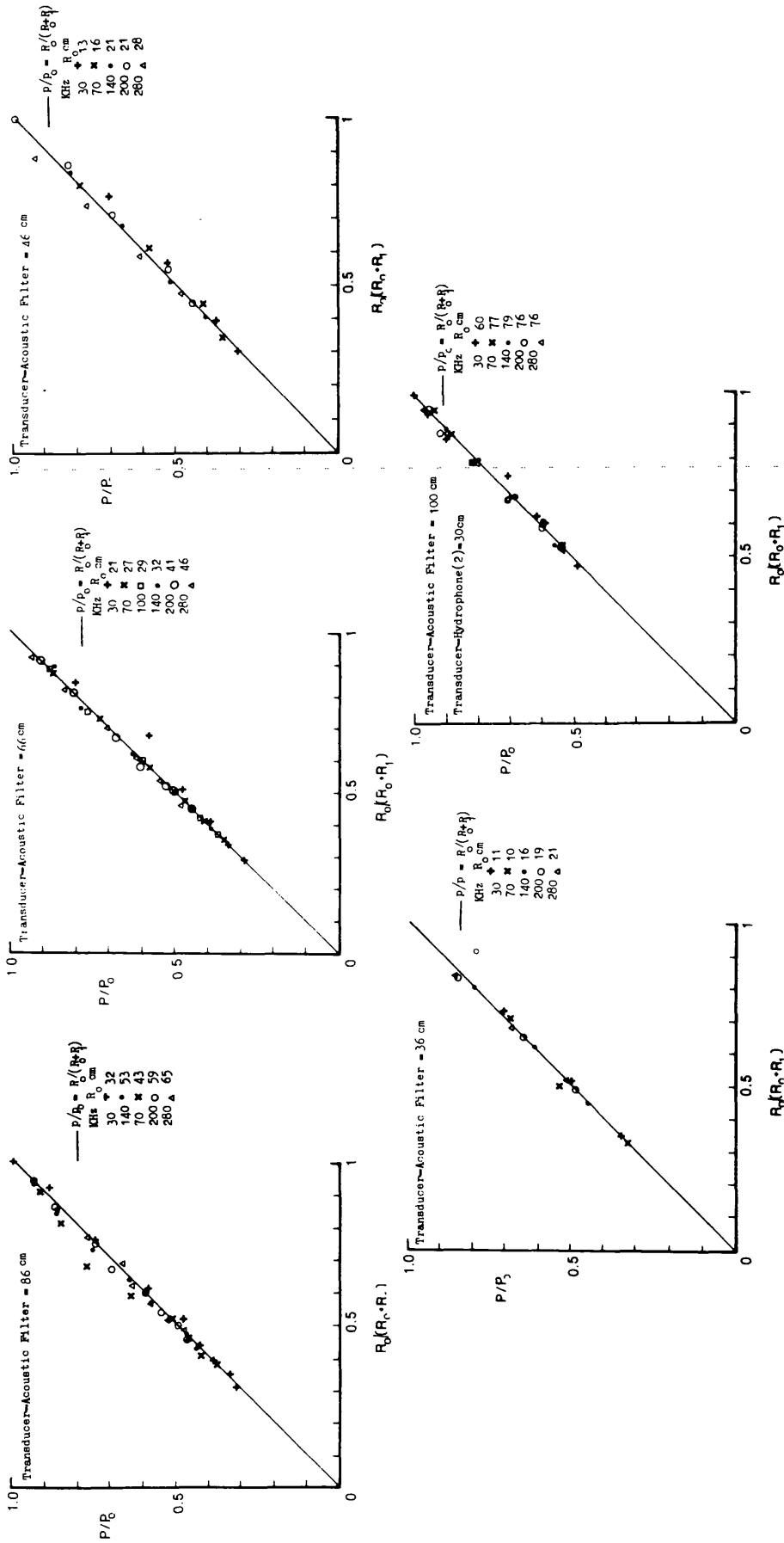
195

Fig 14 Truncated axial pressure measurements, p, at distances of R_1 from the truncation position. The pressure is normalised by P_0 the axial pressure at $R_1 = 0$. The truncation lengths are 100, 86, 66, 46 and 36 cm from the transducer. The pressure appears to originate from a spherical source located at R_0, whose value varies with frequency and truncation length.

RELATIVE PRESSURE, P/P_O

70 70

50 50

30 30

20 20

100 200 300   100 200 300

Fig 15   FREQUENCY (kHz)   Fig 16

Fig 15   Pressure at the rough surface position, p_o , to the receiver
position, p, at distances of 70, 50, 30 and 20 cm from the surface.
The transducer-surface separation was 100 cm.   ● Measured values.
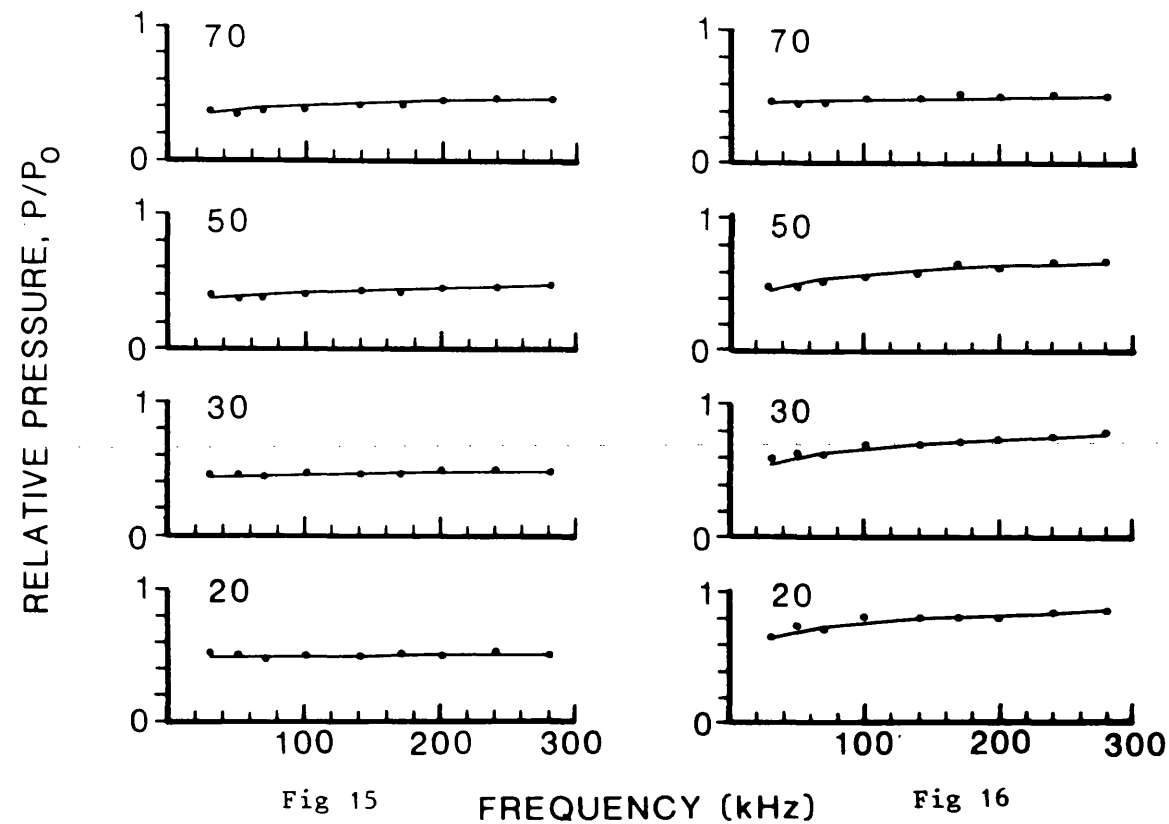- Calculated using equations A4-8 and A4-9.

Fig 16   Pressure at the rough surface position, p_o , to the
receiver position, p, for distances of 70, 50, 30 and 20 cm
from the surface.   The transducer-surface separation was
86, 66, 46 and 36 cm respectively.   ● Measured values.
- Calculated using equations A4-8 and A4-9.

of the scattered intensity predicted from equation 49 in chapter 2.
The values for R_1 used in the predicted scattered intensity cal-
culations are the distances used here.

A4.6   Phase

The theoretical development of chapter 2 assumed the phase to
have the form associated with a spherically spreading wave emanating
from the source whose location was obtained in the manner described
in the previous section.   Since the pressure levels are following
a 1/R form along the acoustic axis from the truncation point, and
attenuation is negligible, then the wavefront near the axis will have
a spherical form.

Measurements upon the phase variation of the truncated para-
metric array have been conducted by Humphrey (43) and these are
shown in figures 17, 18 and 19.   A phase centre can be located
within the array about which the phase varies near the acoustic axis
with the form of a spherically spreading wave.   At f_- = 50 kHz the
separation between the transducer and filter was 56 cm, and the
receiving position was 10 cm beyond the truncation point, this gave
a value for the apparent source centre as 35 cm from the hydrophone.
Using the same geometry but with the system used in this investigation
axial pressure measurements indicated an apparent source centre
34 cm from the hydrophone.

Berktay and Shooter (65) investigated the endfire line array from
which can be derived the phase variation near the acoustic axis.
Providing $k\rho^2/2Z \ll 1$ and $k\rho^2/2(Z-L) \ll 1$, where k is the radiation
wave number, L is the length of the endfire array, and $\sqrt{(Z^2 + \rho^2)}$

is the distance from the beginning of the endfire array to the

observation point then the velocity potential can be written

as

$$\phi = \frac{Q_0}{4\pi} \ln \left(Z/(Z-L) \right) \exp \left[-jk \left(Z + \rho^2 \psi/2Z \right) \right] \qquad A4\text{-}10$$

where

$$\psi = \left[(L/Z)/(1-(L/Z)) \right]/\left[-\ln(1-(L/Z)) \right]$$

For a fixed value of Z along the acoustic axis, the phase change

moving perpendicular to the acoustic axis in the direction of ρ,

is given by $\rho^2\psi/2Z$. Near the axis this is the same change as

would be observed for a spherically spreading source located at

$Z' = Z/\psi$.

Moving away from the acoustic axis the approximation that the

wavefront is spherical appears to become poorer from figures 17, 18

and 19. However, for the case of scattering from the rough surface

the phase coherency is being reduced by the rough surface undulations,

which with the directivity of the transmitter reduced the influence

of the departure of the wave front from a spherical form.

Whether the phase and amplitude centres exactly coincide is

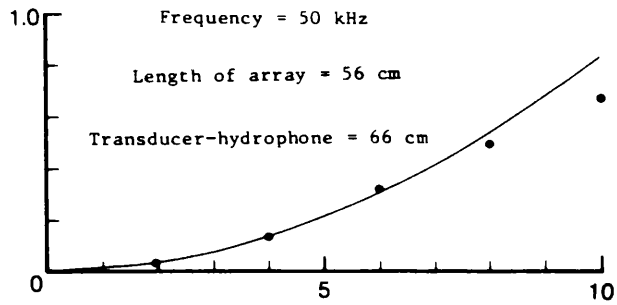difficult to establish exactly, although the comments made in the

Fig 17 Phase variation of the truncated parametric array. -
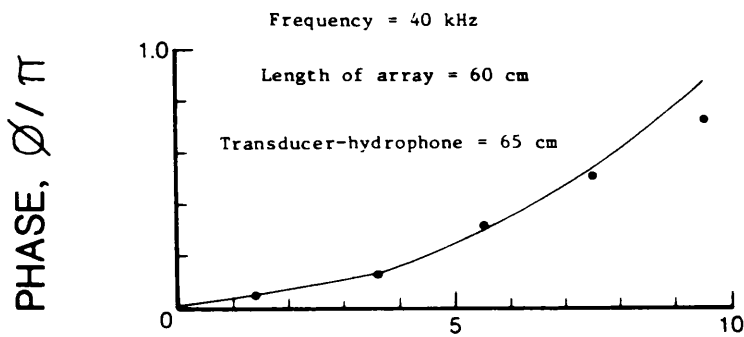Phase centre at 35 cm from the hydrophone.

Fig 18 Phase variation of the truncated parametric array. -
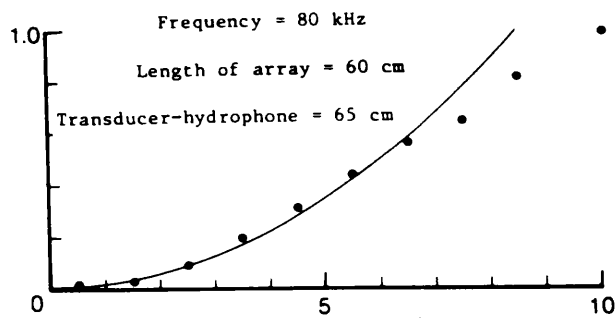Phase centre at 32 cm from the hydrophone.

Fig 19 Phase variation of the truncated parametric array. -
Phase centre at 38 cm from the hydrophone.

DISTANCE OFF ACOUSTIC AXIS, ρ (cm)

second paragraph of this section indicate that they are similar in value. However, for the calculation of the coherent intensity each secondary source within the interaction volume can be treated as creating Huygen wavelets, whose amplitude and phase are coincident. Each of these, generates its own image source and by superposition the parametric array is reflected with the intensity reduced by the factor $R^2 \exp(-g)$. For the calculation of the incoherent intensity, the value of R_0 in the phase term is only retained as a second order quantity through $\cdot$ s and small variations in R_0 do not have a significant effect on the calculation of the scattered intensity.

A4.7 Summary

The potential of the parametric array to generate the requisite highly directional beamwidths over a broad frequency range was found to be realisable and suitable for carrying out scattering experiments on a model rough surface in a laboratory tank. The range of frequencies available, and the area of surface insonified conformed closely to the original specifications for the source.

The parametric array required premature truncation before the surface, to prevent problems arising due to the scattered primaries, and this was achieved by the use of a low-pass acoustic filter. The truncated beam profiles, not withstanding the effect of the on-axis hydrophone were all well represented by the Gaussian directivity function.

Appendix 5   Comparison Of The Theoretical Developments

With Published Experimental Data

An experimental investigation into the backscattered, forward

scattered, and specularly scattered intensity from four pressure

release surfaces has been reported in reference (22). The surfaces

have root-mean-square heights of 0.231, 0.462, 0.925 cm, and auto-

correlation length of 4 cm for the first three and 8 cm for the

fourth surface. The Gaussian probability density function fits the

measured height distribution reasonably well. The Gaussian auto-

correlation function is a relatively poor fit to the measured

autocorrelation function, however, it was also used when analysing

these surfaces in reference (20) and found to be successful.

Figures 1, 2 and 3 give details of the surfaces.

The data reported on the specularly scattered intensity is

considered in this appendix. The intensity was measured from near

normal incidence down to an incidence angle of 80° from the normal.

The frequencies used for the measurements were 100, 220 and 500 kHz.

This gave a range in values for the roughness parameter g of

between 0.116 when the incident radiation on the smoothest surface

was at 80° and 100 kHz, through to 1540 at normal incidence on the

roughest surface for a frequency of 500 kHz.

Two curves are compared with the experimental values, these

are shown in figures 4, 5 and 6. The normalised measured intensities

are represented by the dotted line. The broken line was calculated

using equation 2-47 of Chapter 2 and the solid line was obtained with

the same expression but using the approximation s = 0. Better
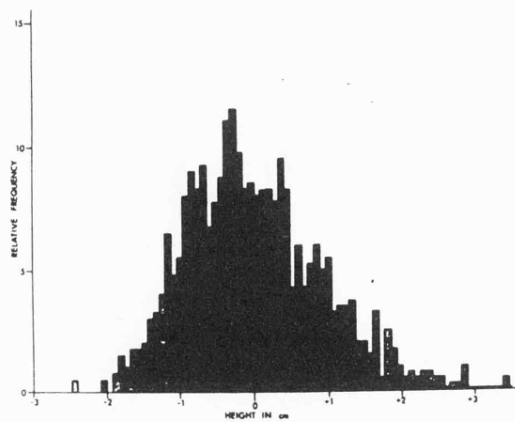
FIGURE 6
HISTOGRAM OF HEIGHTS MEASURED AT 1089 SAMPLE
POINTS FROM THE CENTER QUARTER OF THE MODEL

Fig 1   Surface height distribution (taken from reference 22).
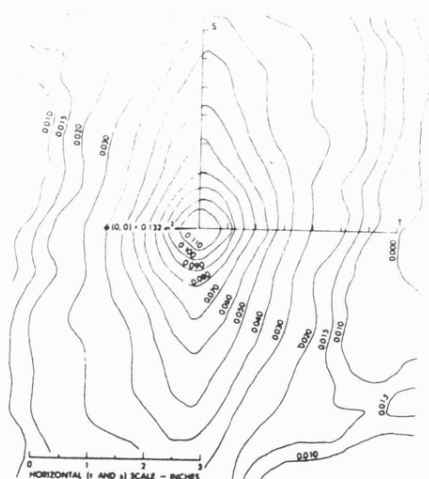
FIGURE 7
CONTOUR MAP OF THE AUTOCORRELATION FUNCTION
OF THE CENTER QUARTER OF THE MODEL
THE DIMENSION OF THE CONTOURS IS in²
VALUES WERE COMPUTED AT ½-in. LAGS.

Fig 2   Surface autocorrelation function (taken from reference 22).
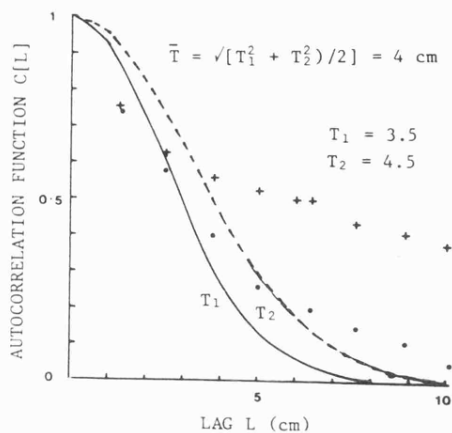
Fig 3   Surface autocorrelation function in "X" and "Y" directions

compared with Gaussian autocorrelation functions with

autocorrelation lengths of 3.5 and 4.5 cm.

SPECULAR SCATTERING COEFFICIENT, $<I>/I_0$
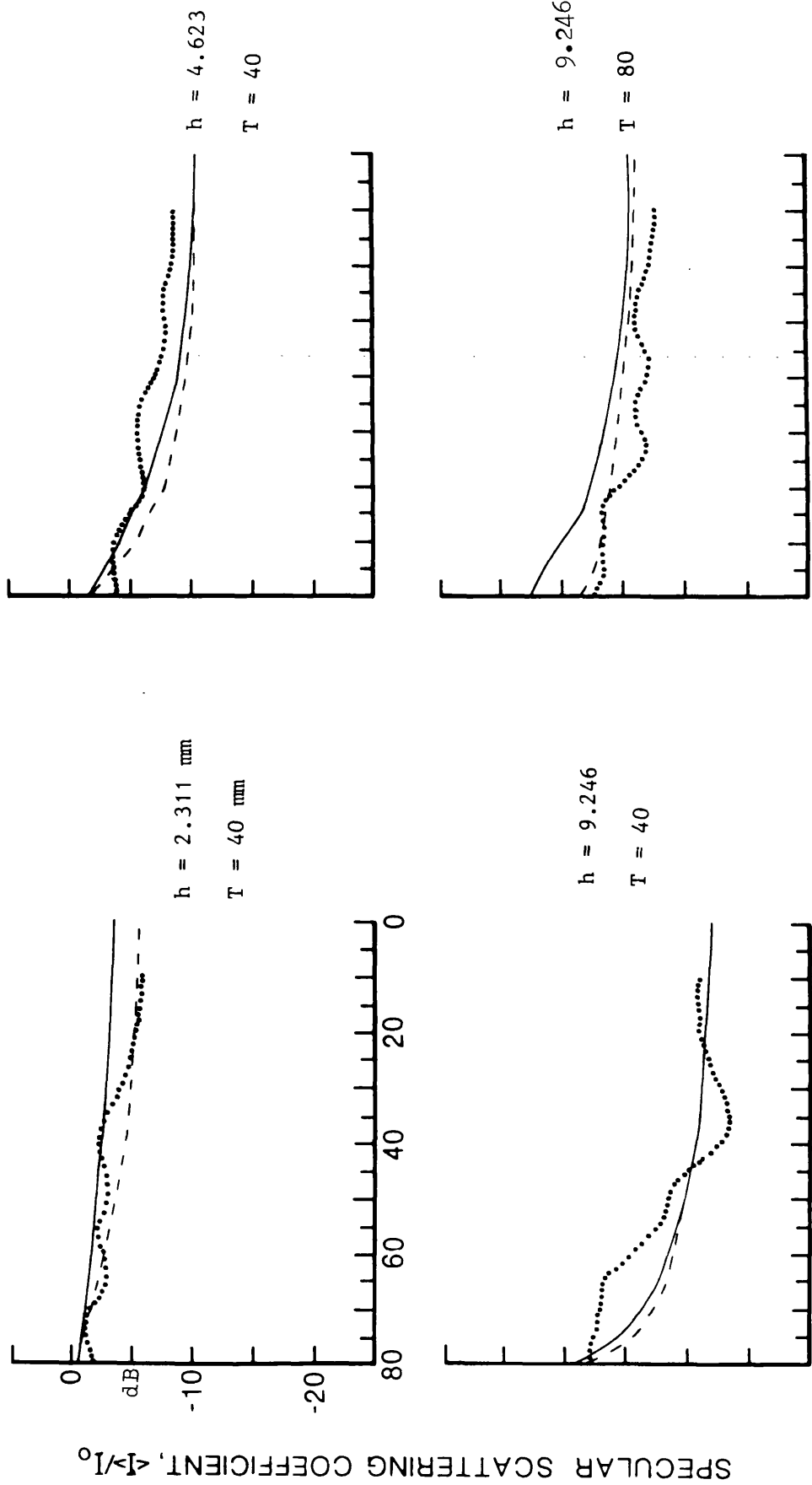
ANGLE OF INCIDENCE θ°

Fig 4 Predicted curves taken from equation 2-47 compared with measured values from reference (22). ● Measured, — equation 2-47 with s = 0, and ---- equation 2-47 with values for s used. Insonifying frequency 100 kHz.
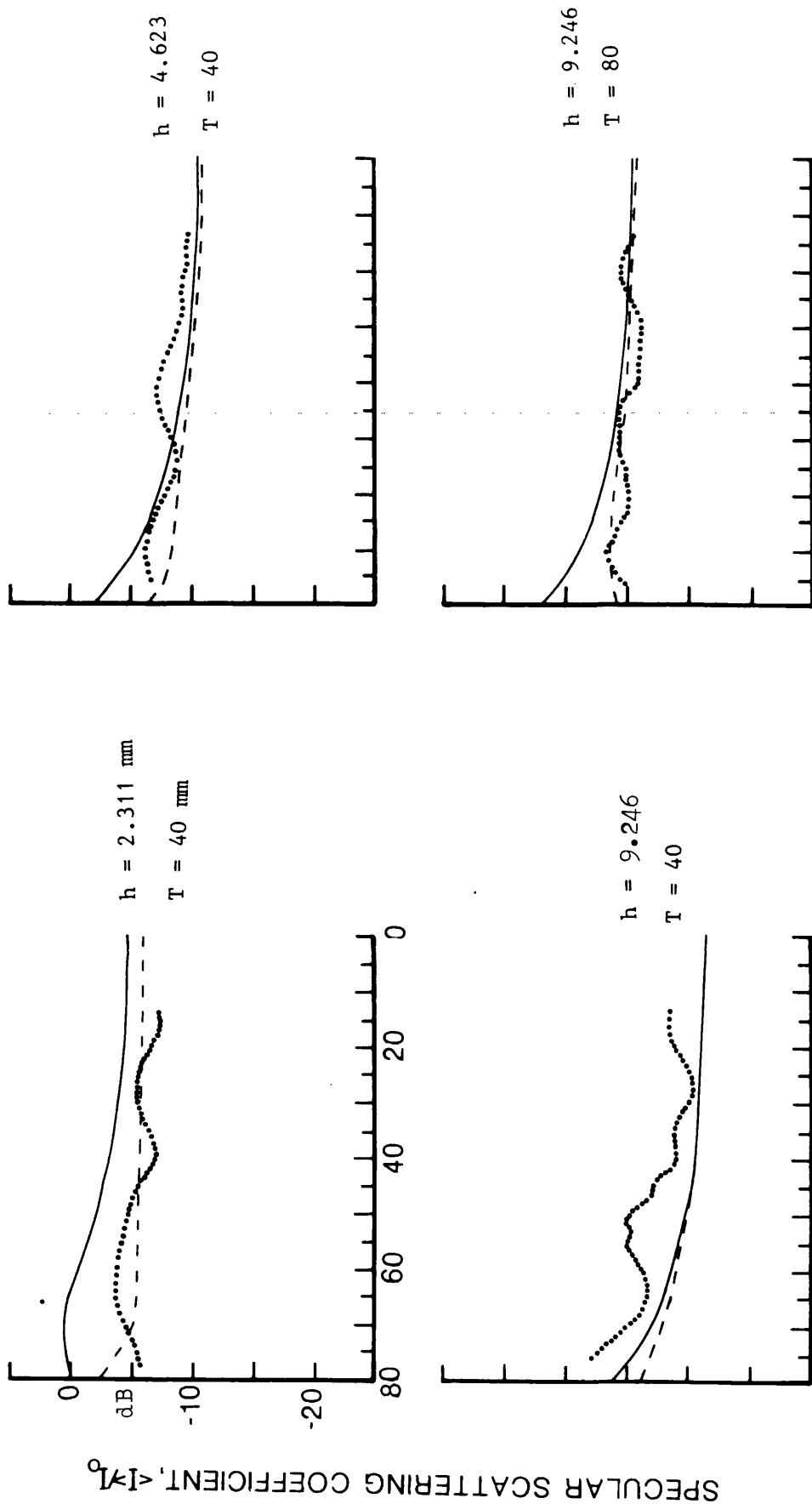
Fig 5 Predicted curves taken from equation 2-47 compared with measured values from reference (22). ●Measured,
— equation 2-47 with s = 0, and —--- equation 2-47 with values for s used. Insonifying frequency 220 kHz.
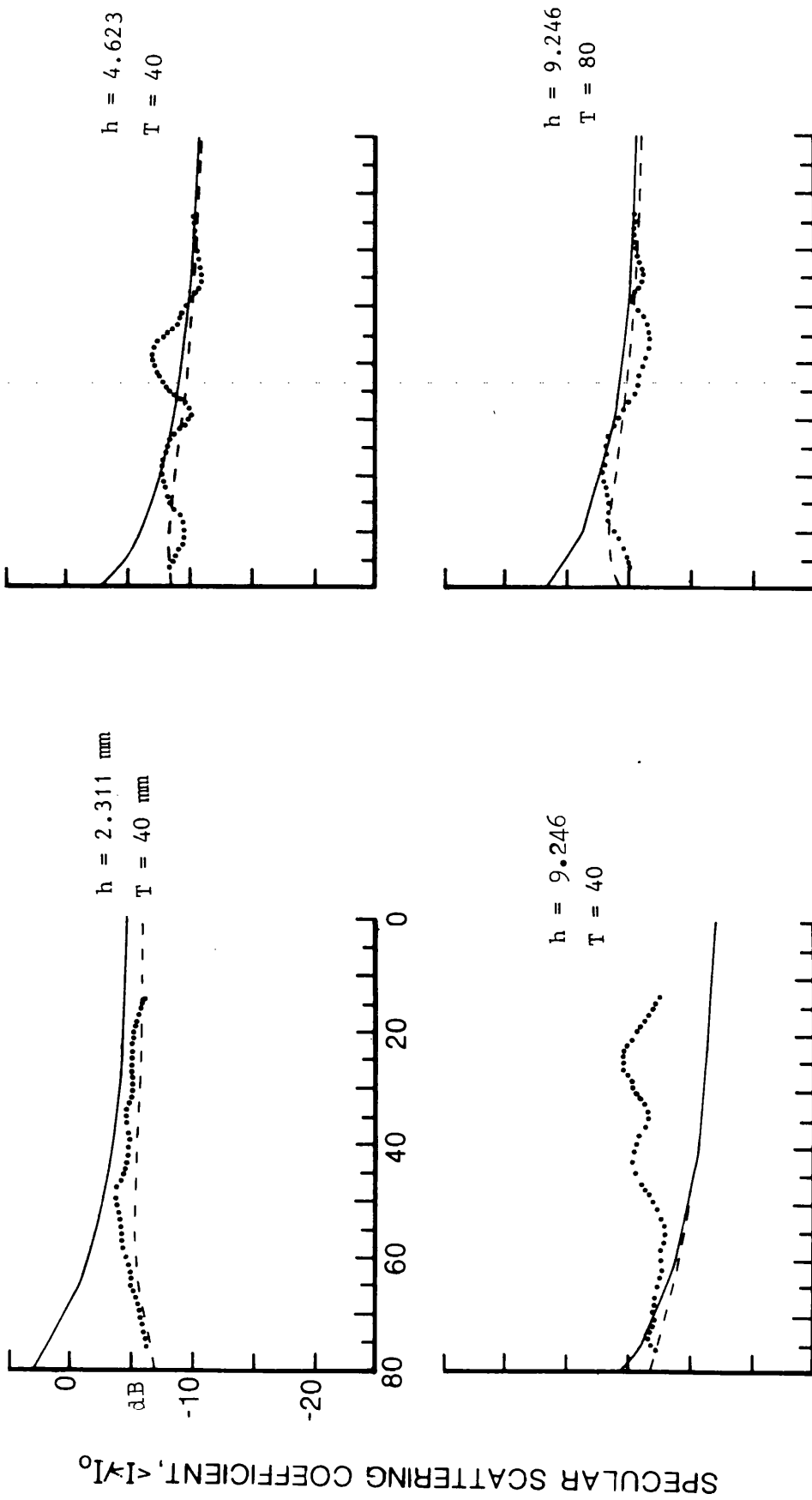
Fig 6 Predicted curves taken from equation 2-47 compared with measured values from reference (22). ● Measured, — equation 2-47 with s = 0, and ---- equation 2-47 with values for s used. Insonifying frequency 500 kHz.

agreement between the calculated and measured intensities is normally obtained when the approximation s = 0 is not used, in this case the predicted intensities compare well with the measured data.

The poorest agreement is obtained for the surface with a root-mean-square height of 0.925 cm and an autocorrelation length of 4 cm. The predicted intensities underestimate the measured scattered intensities. This surface has the steepest root-mean-square slope and therefore shadowing and or multiple scattering could be occurring, and introducing the observed discrepancy between the measured and predicted intensities.

References

1. Ouchi, K, Uscinski, B J, Robertson, Y C and Thomas, T J.   Recent progress and development in the field of of microwave interactions with the sea and land surfaces.   Oxford Computer Services Ltd.   Study Reference E486/1975, ZF/263/08.   March 1980.

2. Berry, M V.   The statistical properties of echoes diffracted from rough surfaces.   Phil Trans Roy Soc Serv A273, 611-654, 1973.

3. Horton, C W.   A review of reverberation, scattering and echo structure.   J Acoust Soc Amer 51, 1049-1061, 1972.

4. Fortuin, L.   Survey of literature on reflection and scattering of sound waves at the sea surface.   J Acoust Soc Amer 47, 1209-1228, 1970.

5. Strutt Lord Rayleigh, J W.   Theory of sound.   Dover, New York, 1945.

6. LaCasce, E O and Tamarkin, P.   Underwater sound reflection from a corrugated surface.   J Appl Phys 27, 138-148, 1956.

7. Marsh, H W.   Exact solution of wave scattering by irregular surfaces.   J Acoust Soc Amer 33, 330-333, 1961.

8. Uretsky, J L.   The scattering of plane waves from periodic surfaces.   Annals Phys 33, 400-427, 1965.

9. Barnard, G R, Horton, C W, Miller, M K and Spitznogle, F R.   Underwater-sound reflection from a pressure sinusoidal surface.   J Acoust Soc Amer 39, 1162-1169, 1966.

10. Eckart, C.   The scattering of sound from the sea surface.   J Acoust Soc Amer 25, 566-570, 1953.

11. Clay, C S and Medwin, H.   Acoustical.   Oceanography, Wiley 1977.

12. Horton C W and Muir T G. Theoretical studies on the scattering of acoustic waves from a rough surface. J Acoust Soc Amer 41, 627-634, 1967.

13. Horton C W, Mitchell S K and Barnard G R. Model studies on the scattering of acoustic waves from a rough surface. J Acoust Soc Amer 41, 635-645, 1967.

14. Proud, Beyer and Tamarkin. Reflection of sound from randomly rough surfaces. J Appl Phys 31, 543-552. 1960

15. Beckmann P and Spizzichino A. The scattering of electomagnetic waves from rough surfaces. Pergamon, 1963.

16. Clay C S and Medwin H. High-frequency acoustic reverberation from a rough-sea surface. J Acoust Soc Amer 36, 2131-2134, 1964.

17. Hayre H S and Kaufman D E. Plane-wave scattering from a rough surface with correlated large- and small-scale orders of roughness. J Acoust Soc Amer 38, P599-603, 1965.

18. Medwin H. Specular scattering of underwater sound from a wind-driven surface. J Acoust Soc Amer 41, 1485-1490. 1967

19. Melton D R and Horton C M. Importance of the Fresnel correction in scattering from a rough surface. II Scattering coefficient. J Acoust Soc Amer 47, Pt2, 290-303. 1970

20. Boyd M L and Deavenport R L. Forward and specular scattering from a rough surface theory and experiment. J Acoust Soc Amer 53, 791-801, 1973.

21. Clay C S and Medwin H. Dependence of spatial and temporal correlation of forward-scattered underwater sound on the surface statistics. I Theory. J Acoust Soc Amer 47, 1412-1418, 1969.

22. Welton P J, Frey H G and Moore P. Experimental measurements of the scattering of acoustic waves by rough surfaces. J Acoust Soc Amer 52, P1553-1563, 1972.

23. Clay C S, Medwin H and Wright W M. Specularly scattered

    sound and the probability density function of a rough surface.

    J Acoust Soc Amer 53, 1677-1682.

24. Bruno D R, Novarini J C and Vara C D. Effect of the

    surface correlation on the average scattered pressure in

    Eckart's Formulation.

25. Mintzer D. Discussion of the Paper by C Eckart on Sea Surface

    Scattering. J Acoust Soc Amer 25, 1015(L), 1953.

26. Meecham W C. On the use of the Kirchhoff approximation for the

    solution of reflection problems. J Rotational Mech Anal 5,

    323-333, 1956.

27. Bourne D E and Kendall P C. Vector Analaysis. Oldbourne,1967.

28. Tolstoy I and Clay C S. Ocean Acoustics. McGraw-Hill, 1966.

29. Born M and Wolf E. Principles of Optics. Pergamon Press, 1965.

30. Mikeska E E and McKinney C M. Range dependence of underwater

    echoes from randomly rough surfaces. J Acoust Soc Amer 63,

    1375-1380, 1978.

31. Fung A K and Leovaris A. Experimental verification of the proper

    Kirchhoff Theory of wave scattering from known randomly rough

    surfaces. J Acoust Soc Amer 46, 1057-1061, 1969.

32. Numrich S K and Callen E. Scattering of acoustic waves from

    rough surfaces. Final Report. Work Unit No NR RR032-05-01, 1979.

33. Markson J L and Stern R. Use of FM pulses to measure acoustic

    backscatter from rough plane surfaces. J Acoust Soc Amer 49,

    1464-1474, 1971.

34. Bendat J S and Piersol A G. Random Data. Analysis and measure-

    ment procedures. Wiley, 1971.

35. Kennedy J B and Neville A M. Basic statistical Methods for

    Engineers and Scientists. 1964.

36. Schwartz M and Shaw L. Signal Processing Discrete Spectral Analysis

    Detection and Estimations. 1975. McGraw-Hill.

37. Westervelt P J. Parametric Acoustic Array. J Acoust Soc Amer

    35, 535-537, 1963.

38. Kossoff G. The effects of backing and matching on the performance

    of Piezoelectric Ceramic Transducers. IEEE Trans Sonics and

    Ultrasonics, SU-13, 20-30, 1966.

39. Tucker D G and Gazey B K. Applied Underwater Acoustics.

    Pergamon Press, 1966.

40. Koyman, H, Smith B V and Gazey, B K. Equivalent circuits for

    high-frequency sonar transducers. Electron Lett 15, 600-601, 1979.

41. Humphrey V F and Hsu C H. Non-linearity of cylindrical

    hydrophones used for the measurement of parametric arrays. Proc

    Inst of Acoust Conf. Transducers for sonar application 5.1, 1980.

42. Wood A B. A textbook of sound. Bell and Son, 1964.

43. Humphrey V F. Private communication.

44. Kendall M G and Stuart A. The Advanced Theory of Statistics. Vol I

    Griffin. 1958

45. Cochrane N A and Dunsiger A D. Sediment roughness characteristics

    measured by Broadband Spectral Analysis Echoes. Proc Inst

    Canadian Conf on Marine Geotechnical Eng Calgary, 140-150, 1979.

46. Bass F G and Fuks I M. Wave scattering from statistically

    rough surfaces. Pergamon Press, 1979.

47. Pace N G. Acoustic classification of the sea bed. Handbook of

    Marine Science, Geophysical Exploration at Sea. CRC Press.

    Ed R A Geyer, in press.

48. Pace N G . Sediment Identification Using Acoustic Techniques. Unpublished report 1974.

49. Pace N G . Underwater Acoustic Backscattering of Wide Band Signals From Sedimentary Materials Unpublished report 1978.

50. Williams J P. Quantitative sediment identification using remote acoustic techniques. PhD thesis University of Wales, 1978.

51. Gurcan M K, Creasey D J and Gazey B K. Wideband high-frequency sonar transmissions for sediment identification. Proc IERE Conf Electronics for Ocean Technology, 273-282, 1981.

52. Bronzite M. Simple Active Filters. Wireless World. 117-119, March 1970.

53. Bellin J L S and Beyer R T. Experimental investigation of an end-fire array. J Acoust Soc Amer 34, 1051-1054, 1962.

54. Berktay H O and Smith B V. End-fire array of virtual sound sources arising from the interacting of sound waves.Electron Lett, March 1965.

55. Hobaek H. Experimental investigation of an acoustical end-fire array. J Sound Vib 6, 460-463, 1967.

56. Muir T G and Blue J E. Experiments on the acoustic modulation of large-amplitude waves. J Acoust Soc Amer 46, 227-232, 1969.

57. Fenlon F H. On the performance of a dual frequency parametric source via matched asymptotic solutions of Burgers equation. J Acoust Soc Amer 55, 35-46, 1974.

58. Berktay H O and Leahy D J. Farfield performance of parametric transmitters. J Acoust Soc Amer 55, 539-546. 1974

59. Moffett M B and Mellen R H. Model for parametric acoustic sources. J Acoust Soc Amer 61, 325-337, 1977.

60. Muir T G and Blue J E. Transient Response of the Parametric Acoustic Array. Proc of Conf Non-linear Acoustics. 1969.

61. Rolleigh R L. Difference frequency pressure within the inter-action region of a parametric array. J Acoust Soc Amer 58, 964-971, 1975.

62. Fenlon F H and McKendree F S. Axisymmetric parametric radiation -A weak interaction model. J Acoust Soc Amer 66, 534-547, 1979.

63. Hunkabay J M. An experimental study of parametric acoustic arrays with intermediate directivity in water. J Acoust Soc Amer 67, 1480-1485, 1980.

64. Berktay, H O, Smith B V, Braithwaite H B and Whitehouse M. Sub-bottom profiles using parametric sources. Proc Inst of Acoust Conf. Underwater application of non-linear acoustics 1.2, 1979.

65. Berktay H O and Shooter J A. Nearfield effects in end-fire line arrays. J Acoust Soc Amer 53, 550-556, 1973.